OPTICAL TRANSITIONS IN ALKALINE EARTH SULFIDE ELECTROLUMINESCENT PHOSPHORS

By

PHILIP DEREK RACK

A DISSERTATION PRESENTED TO THE GRADUATE SCHOOL
OF THE UNIVERSITY OF FLORIDA IN PARTIAL FULFILLMENT
OF THE REQUIREMENTS FOR THE DEGREE OF
DOCTOR OF PHILOSOPHY

UNIVERSITY OF FLORIDA

1997

to my wife karen and daughter kathryn

ACKNOWLEDGMENTS

I would first like to thank Dr. Paul H. Holloway who has been my advisor, mentor, and friend over the past four years. He has been a source of guidance and encouragement during my graduate career and his example has challenged me to strive for excellence. Secondly, I would like to thank Dr. Sey-Shing Sun for many insightful discussions and for providing me with many samples to investigate various electroluminescence phenomena. Thirdly, I would like to thank Ted O'Brien and Dr. Mike Zerner for the collaboration on the molecular orbital cluster calculations. The many hours of discussion and countless computer calculations were instrumental in theoretically modeling and quantifying the experimental observations. Many others have contributed technically to this dissertation and deserve recognition. I would like to thank Eric Lambers for helping with XPS analysis, Dr. Balu Pathangey and Dr. Mark Davidson for sputter depositing the SrBaS:Ce thin films, and Mike Stora and Won Park for PL measurements.

Next I would like to thank many of my friends who have supported and encouraged Karen and me during our stay in Gainesville. I am indebted to Dean Paxton, Jim Fitzgerald, and Thad Adams who were always there when I needed a break during the hectic days at the office. They were always there when I needed a quick pick-me-up. I am also thankful to Greg Olexa whose friendship I appreciate and character I admire. Finally, I would like to thank my life-long friends: Matthew Jung, Bryan Kessler, Jason Huff, Chad Hambrick, Kirk Kishbach, and last, but not least, Carlos Gonzalez. They really are the best friends a guy could ever have.

Thirdly, I would like to thank my family who have always been there for me and have supported me in all my endeavors. I want to thank Mom and Dad Fountain, and all my newest family members for all their love and encouragement. Next I want to thank my Aunt Marilyn, and my Grandmother; they have been a special part of my life and I love them more than they will ever know. I also want to thank my brother Jeff who I have always looked up to. He has given me a lot of good advice during my graduate career, whether it was solicited or not. I would like to especially thank my mom and dad who have always loved me and supported me. I have always aspired to be like my dad and am thankful for him always being there for me. My mom has also always been there for me and has probably sacrificed more for me than anyone else. I want to thank her for investing her life in me.

The last person I want to thank is my wife Karen. She is the most important person in my life and I am privileged to be her husband. She encourages me when I am down, rejoices with me when I am up, and loves me all the time. I love her very much and treasure our relationship.

Finally, I want to give all glory, honor, and praise to my Lord and Savior Jesus Christ. I want to acknowledge Him as the source and inspiration for every idea and result that was accomplished in this dissertation. He is my joy and my peace, and His ultimate sacrifice on the cross is the reason I live. I am grateful for the eternity I will get to spend with Him.

TABLE OF CONTENTS

page
ACKNOWLEDGEMENTS........ ii

ABSTRACT........ vii

CHAPTERS

1 INTRODUCTION........ 1

2 LITERATURE REVIEW........ 7

History of Electroluminescence........ 7
Device Structure........ 9
Electrical and Optical Properties of ACTFEL Devices........ 12
Device Physics........ 16
Material Properties........ 28
Fundamentals of Atomic Transitions........ 37
ACTFEL Phosphor Materials........ 41

3 THE EFFECTS OF OXYGEN DOPING $Ca_{0.55}Sr_{0.45}Ga_2S_4$:Ce THIN FILMS........ 79

Introduction........ 79
Background........ 79
Experimental Procedure........ 82
Results........ 83
Discussion........ 85
Summary........ 97

4 EMISSION SPECTRA CHANGES IN Ce DOPED ALKALINE EARTH (Mg, Ca, Sr, AND Ba) SULFIDE PHOSPHORS........ 115

Introduction........ 115
Background........ 115
Experimental Procedure........ 117
Results........ 118
Discussion........ 120
Summary........ 132

5 SrS:Te Bound Excitons.......... 156

Introduction.......... 156
Background.......... 156
Experimental Procedure.......... 159
Results.......... 160
Discussion.......... 163
Summary.......... 174

6 CONCLUSIONS.......... 194

Oxygen Doped $Ca_{0.55}Sr_{0.45}Ga_2S_4$:Ce ACTFEL Devices.......... 194
Ce Doped Alkaline Earth Sulfide Phosphors.......... 195
SrS:Te Bound Excitons.......... 197

7 FUTURE WORK.......... 200

Oxygen Doped $Ca_{0.55}Sr_{0.45}Ga_2S_4$:Ce ACTFEL Devices.......... 200
Ce Doped Alkaline Earth Sulfide Phosphors.......... 201
SrS:Te Bound Excitons.......... 202

REFERENCES.......... 203

BIOGRAPHICAL SKETCH.......... 210

Abstract of Dissertation Presented to the Graduate School
of the University of Florida in Partial Fulfillment of the
Requirements for the Degree of Doctor of Philosophy

OPTICAL TRANSITIONS IN ALKALINE EARTH SULFIDE ELECTROLUMINESCENT PHOSPHORS

By

Philip Derek Rack

May, 1997

Chairman: Dr. Paul Holloway
Major Department: Materials Science and Engineering

The optical transitions in three alkaline earth (AE) sulfide material systems were investigated. In undoped and oxygen doped $Ca_{0.55}Sr_{0.45}Ga_2S_4$:Ce the optical transitions occur between Ce energy levels, which are sensitive to the local bonding of the Ce. The oxygen doped films were found to be brighter, more efficient, and emitted higher energy photons than the undoped materials. Analytical data showed that while Ce was bonded to eight sulfur ions in the undoped films, in the oxygen doped films the Ce was bonded to 5 sulfur and three oxygen ions. To model the effects that oxygen has on the Ce energy levels, semiempirical cluster calculations were performed. The calculated Ce energy levels for the undoped and oxygen doped thin films were in good agreement with the experimentally determined energy levels.

The optical transitions of different Ce doped AE sulfide phosphors (MgS:Ce, CaS:Ce, SrS:Ce and BaS:Ce) were also studied. Semiempirical cluster calculations were performed to model the Ce energy levels in MgS, CaS, and SrS and a good agreement with the experimental values was obtained. The crystal field model was also used to calculate the energy levels in these phosphors, and while it accurately described the

CaS:Ce and SrS:Ce, it had to be modified for the MgS:Ce. The crystal field model also predicted that the BaS:Ce transition energy would be higher than SrS:Ce. $Sr_xBa_{1-x}S$:Ce thin films were grown, and analytical data revealed that films with higher BaS concentrations had lower transition energies than pure SrS:Ce. The discrepancy between the model calculations and the experimentally determined transition energies was explained by a local change in the Ce symmetry.

The properties of SrS:Te powders and thin films were also studied and excitons bound to Te sites were determined to luminesce efficiently. Two emission peaks (360 and 400 nm) were identified, and their intensities were found to be dependent on the Te concentration. From temperature dependent photoluminescent data several important bound exciton properties were determined, including: 1) the binding energy, 2) the thermal quenching activation energy, and 3) the vibrational energy.

CHAPTER 1

INTRODUCTION

Though the display market is currently dominated by the standard cathode ray tube (CRT), the flat panel display (FPD) market share has steadily grown. The Electronic Display Industry reported that in 1992 the FPD market share was 27%, and projected a 44% increase for 1995. The FPD applications range from televisions and laptop computers to aircraft cockpits and helmet mounted displays. According to Stanford Resources, the 1994 FPD market breakdown (by applications) is demonstrated in figure 1-1. The current flat panel display technologies include liquid crystal displays (LCD), plasma displays (PD), field emission displays (FED), and electroluminescent displays (ELD). Presently, LCDs, PDs, and ELDs are commercially available, while FEDs are still in the developmental stage. The 1992 FPD market was dominated by LCDs (91%), while PDs (7%) and ELD's (2%) competed only in niche markets. Though LCD's (85%) are still projected to dominate the overall market in 1997, ELDs are expected to grow to 8% while PDs should remain at 7% (figure 1-2) [HOL 96].

The focus of this dissertation will be electroluminescent flat panel displays. More specifically, ac-driven thin film electroluminescent (ACTFEL) displays will discussed. While each FPD technology has its own strengths and weaknesses, ACTFEL displays have several qualities that make them particularly attractive for small to midsize flat panel displays. Fundamental to an EL device is its solid state construction which can be fully integrated onto the substrate of the drive electronics. This has the advantage that a fully integrated optoelectronic flat panel display can be produced on a single substrate. Additionally, since EL displays are emissive, the viewing angle is greater than 160 degrees which has been an inherent problem with the LCD displays. EL panels offer a temperature range of -25°C to 60°C which is limited by the drive electronics, and the solid state construction makes them inherently more shock and vibration resistant. The ruggedness and temperature range of flat panels are very critical for certain military and industrial applications. Currently, thin film EL displays are the longest lasting, most reliable flat panel display technology on the market. Display panels have demonstrated device lifetimes of over 50,000 hours with less than 10% luminance change [RAC 96, KIN 96b].

To understand the fundamentals of an ACTFEL device, one must consider the device structure, the electrical and optical properties, the device physics, and the unique materials requirements. In addition, the radiative recombination events in these devices are most often atomic transitions which are fundamentally different than traditional semiconductor radiative transitions (i.e., band edge, donor-acceptor, etc.,). These topics are each discussed in chapter two where the literature on electroluminescence is reviewed. Particular attention will be given to the properties of the phosphor material, and the current status of the red, green and white EL phosphors will by presented. The current status of the blue EL phosphors will be briefly reviewed in the background sections of chapters three and four.

While the advantages of ACTFEL displays make them very attractive for many applications, the main drawback in this technology is the lack of sunlight readable full color displays. Filtered ZnS:Mn and ZnS:Tb yield bright red and green devices, respectively, but currently the brightness of a blue phosphor is too low. Subsequently, most of the ongoing research for ACTFEL devices has focused on the evaluation and development of blue phosphor materials. Currently, two materials (SrS:Ce and $Ca_xSr_{1-x}Ga_2S_4$:Ce) are the most promising blue EL phosphor materials, and they dominate much of the current ACTFEL research. SrS:Ce has adequate brightness: however, the emission spectra has a peak wavelength of 490 nm which results in a blue-green chromaticity. Conversely, $Ca_xSr_{1-x}Ga_2S_4$:Ce emits a deep blue color (peak wavelength ~ 450nm) but it suffers from low brightness. The goal of this research was to investigate the radiative transitions of these two materials and modify them to develop a brighter blue EL phosphor.

In chapter three, the effects of oxygen doping on $Ca_{0.55}Sr_{0.45}Ga_2S_4$:Ce is discussed. XPS analysis suggested that oxygen was ligating to the Ce luminescent center, and the observed blue shift in the emission spectra was accurately described by molecular orbital cluster calculations. In chapter four, the reported transition energy of Ce doped alkaline earth (Mg, Ca, Sr) sulfides were modeled with molecular orbital cluster calculations and crystal field calculations. The crystal field calculations were then extended to BaS:Ce and they predicted a blue shift in the transition energy. $Sr_xBa_{1-x}S$:Ce thin films were grown, and the emission spectra were found to contradict the theoretical calculations. The reasons are discussed. To explore new blue EL phosphor materials, SrS:Te powders were synthesized as reported in chapter five. The radiative and non-radiative recombination processes in these SrS:Te powders are discussed. This material was found to emit high energy photons under photoluminescent excitation and a configuration coordinate model was used to describe the temperature dependent photoluminescence data. To conclude this study, SrS:Te thin film devices were fabricated and tested under EL excitation. The conclusions of this study are summarized in chapter six, and future research efforts are suggested in chapter seven.

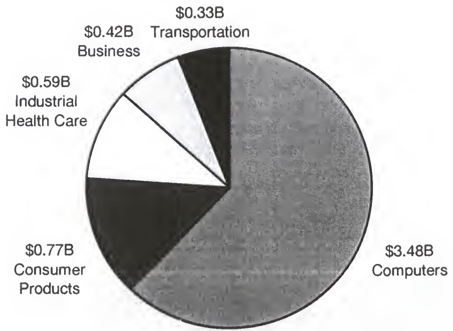

Figure 1-1. 1994 flat panel display market breakdown (by applications).

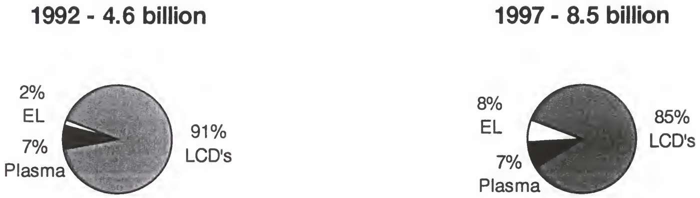

Figure 1-2. A comparison of the 1992 and the projected 1997 flat panel display market share (by technology).

CHAPTER 2

LITERATURE REVIEW

History of Electroluminescence

Electroluminescence (EL) is the phenomenon in which electrical energy is converted to luminous energy without thermal energy generation. The first observations of the electroluminescence phenomenon were reported in 1929 [GUD 29]. Important, but often overlooked experiments by Gudden and Pohl first demonstrated the effect that an electric field has on the photoluminescent decay of a ZnS:Cu phosphor. In 1936 Georges Destriau [DES 36] observed light emission from a suspension consisting of ZnS:Cu and oil; this work is often cited as the first published report on the phenomenon of electroluminescence. Very few people published work on electroluminescence after Destriau's discovery, until the early 1950's when GTE Sylvania received a patent for an EL powder lamp [TAN 85]. Subsequent to this patent, research efforts concentrated on powder EL phosphors in order to achieve a brighter, long lifetime light source with minimal power requirements. This effort however, soon ended when it was determined that the phosphors being investigated were unable to provide adequate sustained brightness over the minimum commercially acceptable lifetimes (500 hours).

In the 1960's there was a resurgence in EL research which was focused on display technologies. One of the first AC thin film dot matrix displays was unveiled in 1965 by

Sigmatron Corp., which was followed by the demonstration of a sunlight readable numeric display in 1968 [CAS 92 p.8]. No commercial products were ever produced from this effort and eventually this company folded. Later in 1968, Vecht [VEC 68] demonstrated the first DC driven EL panel, but again a commercial product was not generated. In the 1960s great strides were made in thin film technology, which helped Soxman and Ketchpel [SOX 72] fabricate thin film devices. These devices had acceptable lifetimes and multiplexing capabilities, but failed to achieve acceptable reliability. A breakthrough in EL technology was made by Inoguchi et al. (Sharp Corporation) [INO 74] which introduced a new AC thin film approach in 1974. The key to this approach was the concept put forward by Russ and Kennedy (1967) [RUS 67] which described a three-layer sandwich design. The team of researchers at Sharp fabricated a device modeled after a capacitor structure which consisted of a manganese activated zinc sulfide (ZnS:Mn) central phosphor layer and two yttrium oxide (Y_2O_3) insulators that sandwiched the phosphor layer. This was the first high brightness, long lifetime device. This paper is credited with transforming the research and development of electroluminescence into a viable display technology. While both ac and dc driven devices have been explored for display applications, the interest in ac-driven thin film electroluminescent devices has dominated. Sharp succeeded in developing this technology and introduced a monochrome television display in 1978 [CAS 92 p.9]. In order to compete with other display technologies, multicolored displays were introduced by Coovert et al., (Planar Systems) [COO 82] and by 1994 Planar Systems had introduced a prototype full color ACTFEL display [BAR 93].

While ACTFEL research has dominated much of the EL research and development efforts, parallel work has been done in powder EL technology. In the early 1990's, AC powder EL light sources began to reestablish themselves based on improved control of moisture which was necessary to ensure adequate lifetimes. Using a glass microencapsulation technique to avoid moisture-induced degradation of ZnS powders, Durel Corp. demonstrated a flexible thin EL lamp which was incorporated as a back light into LCD flat panel displays (i.e. in wrist watches). Thus, today both thin film and powder EL displays are active in the market place.

Device Structure

A typical ACTFEL device structure is illustrated in figure 2-1. The MISIM (metal-insulator-semiconductor-insulator-metal) structure is usually deposited on a transparent glass substrate which varies in composition depending on the phosphor processing temperature. Typically, Corning 7059 glass is used as a substrate because of its low cost and high availability. In addition, it does not contain alkali metals which have been found to diffuse into the semiconducting phosphor layer and cause the devices to degrade over time [ONO 95 p.61]. Some EL phosphors however, require a high temperature annealing step which is above the 598°C softening temperature of the Corning 7059 glass. When processing temperatures exceed 598°C high temperature glass ceramics are used. These glass ceramics typically cost 10 times that of the standard 7059 glass.

Another structure that has been developed is the so-called "inverted" structure which is shown in figure 2-2. This structure has been used in active matrix electroluminescent (AMEL) [KHO 94] displays as well as thick film hybrid electroluminescent displays [BAI 95]. These structures use opaque substrates which requires that the transparent electrode be deposited on the top of the ACTFEL structure. AMEL displays typically use silicon substrates which allow the drive electronics and the EL device to be manufactured on the same substrate. High performance displays with a resolution 2000 lines/inch (LPI) have been manufactured with this technology [KIN 96a]. The primary market that the AMEL technology is targeting is the so-called helmet mounted or heads up display applications, which include commercial virtual reality games and military flight simulators.

The thick film hybrid EL technology uses an opaque alumina substrate on which they screen print an opaque high dielectric constant ferroelectric thick film as one of the insulating layers. There are several advantages of the thick film hybrid EL approach, namely: 1) the alumina substrate is stable at high temperatures, 2) higher dielectric constant insulators can be used, and 3) thick film processing is inherently cheaper than thin film processing. Most ACTFEL phosphors become brighter and more efficient as the annealing temperature increases. Because alumina is stable at temperatures much greater than 598C, these devices can be annealed at higher temperatures versus standard device structures which are deposited on glass substrates. The advantages of higher dielectric constant insulators will be demonstrated later when the insulating materials and properties are discussed in detail. One disadvantage of this aproach is that the pixel resolution is limited to about 100 microns because of the surface roughness of the alumina substrate. The as-recieved alumina substrates are rough, and require several polishing steps to achieve this resolution. While the first prototype full color thick film hybrid EL display was introduced in 1995 by Westaim Inc., [BAI 95] they have recently developed a monochrome display that will be sold commercially [WU 96].

Though the inverted structure is used in a variety of display applications, this review will focus on the standard device structure. Unless noted, all references to the ACTFEL structure will pertain to the standard (non-inverted) structure.

Regardless of whether the standard or inverted structure is used, the basic function of each layer is the same. Before discussing the ACTFEL equivalent circuit diagram it is appropriate to first summarize the basic function of each layer. First of all, the middle semiconducting layer (commonly called the phosphor layer) is the light emitting material. This material consist of two constituents: 1) the host material which dominates the electrical properties of the phosphor layer, and 2) the luminescent center which dominates the optical properties of the phosphor layer. While specific details will be discussed later, the solid state processes are summarized below. When a large electric field is induced across the phosphor layer, electrons are injected from the phosphor/insulator interface and accelerate through the phosphor layer. These electrons then excite the luminescent centers which subsequently generate light. The phosphor layer is sandwiched between two insulators which limit the current transported across the device. These insulating layers have been found to effectively prolong the lifetime of the ACTFEL device. Finally, the top and bottom electrodes simply complete the device structure and make electrical contact to the drive electronics.

Electrical and Optical Properties of ACTFEL Devices

The basic ACTFEL device structure can be modeled as a simple circuit where the insulators are represented by perfect capacitors and the phosphor layer is represented by a capacitor below threshold and a pair of back-to-back diodes above threshold [ALT 84]. The threshold is the voltage or electric field at which the phosphor layer experiences a Zener breakdown. This mechanism will be explained in more detail in device physics section. Schematically, the equivalent circuit is shown in figure 2-3 . Below threshold the ACTFEL device is simply a 3 series capacitor circuit where the voltage drop across each layer is proportional to the dielectric constant and the layer thickness. At threshold, the phosphor layer experiences a Zener breakdown as electrons are injected by tunneling into the phosphor layer. This produces a real current which is transported across the phosphor layer and is represented by the back-to back Zener diodes in the diagram. ACTFEL devices are driven at high voltages (200-250V) which induce large electric fields (1-2 MeV/cm) across the insulators and the phosphor layer.

One very useful measurement that illustrates the electrical characteristics in an ACTFEL device is the Charge-Voltage (Q-V) diagram which is illustrated in figure 2-4 [KIN 96b]. Initially, in a virgin device, there is no stored polarization charge so at 0 voltage there is a corresponding 0 charge. As the voltage is ramped below threshold, the slope of the Q-V curve $\left(\frac{dQ}{dV}\right)$ is equal to the total capacitance of the insulators and the phosphor layer. When threshold (V_{th}) is reached, the phosphor layer breaks down and charge is transported which causes the slope of the Q-V diagram to increase sharply. The new slope is equal to the series capacitance of the two insulators only. The charge that is transported across the phosphor layer accumulates at the anodic phosphor/insulator interface and creates an opposing polarization field. When the voltage is reduced below threshold, the slope decreases and the capacitance again becomes equal to the combined capacitance of the insulators and the phosphor. Because of the trapped charge at the interface, at 0 V the charge is now non-zero and only when the external field equals the internal polarization field does the charge reduce to zero. When the voltage is cycled through an entire ac pulse, a hysteresis loop is formed whose area is proportional to the power dissipated in the device. The power density (P) is given by:

$$(2\text{-}1)\quad P = 2fC_iV_{mod}V_{dth},$$

where f is the frequency (60 Hz), C_i is the insulator capacitance (18 nF/cm^2), V_{mod} (40 V) is the modulation voltage, and V_{dth} (90 V) is the internal diode threshold voltage. According to equation 2-1 and the values given, a typical ACTFEL device only consumes about 8 mW/cm^2 during typical device operation. C_i and V_{dth} are both a function of the dielectric properties of the phosphor and insulator layers and it will be shown that minimizing the phosphor dielectric constant and maximizing the insulator dielectric constant is critical to lowering the power consumed in ACTFEL displays.

While it is important to understand the electrical properties of ACTFEL devices, it is the optical response to the electrical stimulus that is critical to the display performance. Probably the most important measurement used to evaluate an EL device is the luminance vs. voltage (L-V) plot (Figure 2-5). To make these measurements, all one needs is a variable ac voltage supply to ramp the external voltage (typically 0-300V) and a spectrometer/calorimeter to measure the brightness as a function of the applied voltage. From this simple measurement, several important ACTFEL parameters can be extracted, namely: 1) the threshold voltage (V_{th}), 2) the luminance at V_{th} + 40V (L_{40}), 3) the CIE color coordinates, and 4) the luminous efficiency.

The threshold voltage is typically defined to be the voltage where a brightness of 1cd/m^2 is achieved [ONO 95 p.9]. At this external voltage, the field inside the phosphor is high enough to cause electrons to excite the luminescent centers and generate light. V_{th} is a function of the dielectric properties of the insulator and phosohor layers, and can be controlled by varying phosphor layer thickness (increasing phosphor thickness increases V_{th} and vice versa). This is important because for full color and multi color display applications, it is critical to match the threshold voltages for each phosphor to simplify the drive electronics. For many display applications, a threshold voltage of 180V is used.

As the voltage increases above threshold the phosphor electric field increases proportionally as does the electron energy distribution. Consequently, the brightness usually increases linearly with voltage until the phosphor brightness saturates or until the phosphor layer experiences dielectric breakdown. Another important ACTFEL parameter is the L_{40} value which is defined as the brightness (cd/m^2) at 40V above the threshold voltage. This parameter is important because most ACTFEL displays are driven at 40V above threshold, which is the modulation voltage referred to in equation 2-1 [KIN 96b]. When comparing L_{40} values, it is important to consider both the threshold voltage and the frequency at which the device was driven. L_{40} increases almost linearly with both phosphor thickness (i.e., V_{th}) and frequency: as thickness increases, there are more luminescent centers that electrons can excite, and when frequency increases, the number of passes that electrons make across the phosphor layer increases.

The third set of parameters that are usually extracted from the B-V measurement are the CIE (Commission Internationale de l'Eclairage) coordinates [KEL 96]. The CIE coordinates (x, y, and z) are a measure of the color of the light that the device is generating. Usually only x and y values are reported because the z coordinate is redundant, as $x + y + z = 1$. Figure 2-6 shows the CIE diagram (1936). To obtain the CIE coordinates for a specific emission spectra (intensity vs. wavelength), one must apply what are called the "tri-stimulus functions" to the emission spectra. The tri-stimulus functions are three mathmatical functions that span the visible region of the electromagnetic spectrum, and the extent to which an emission spectra overlaps each of these functions determines what the CIE coordinates will be. The three tristimulus curves are shown in figure 2-7. Obviously, the range of colors that a display can generate is very important. By plotting the CIE coordinates of the different phosphor materials in a display, the range of colors that can be achieved can easily be determined.

The last important parameter that is used as a standard measure for ACTFEL device performance is the luminous efficiency (lum/W). This parameter can be calculated by simply dividing the luminance (cd/m^2) by the power density (W/m^2). Typically, the drive frequency and voltage is specified when the luminous efficiency is reported, and 60Hz at Vth+40V is commonly used because these are common device driving conditions. A simple way to determine the luminous efficiency is to determine the L_{40} (cd/m^2) from the B-V curve, and then measure the power at Vth+40V from a Q-V plot [ONO 95 p.39].

Device Physics

The intent of this section is to review some of the basic physics of ACTFEL devices. Understanding the basic physics of the ACTFEL device helps justify some of the current research that is being explored, and also gives insight into other possible areas of research that could be useful in this technology. The device physics of an EL device can be divided into four main topics, namely: 1) tunnel emission of electrons from interface states, 2) acceleration of electrons to high energies, 3) impact excitation or impact ionization of the luminescent center, and 4) de-excitation of the excited electron by radiative (photon generation) or non-radiative recombination [RAC 96]. These four processes are illustrated in figure 2-8 (omitting non-radiative recombination).

Tunnel Emission

The mechanism of electron injection in ACTFEL devices is critical to understanding the device operation. There are basically two mechanisms responsible for carrier injection, namely: 1) thermionic emission, and 2) field emission or tunneling (Figure 2-9). In ACTFEL devices, one must also consider the source of these carriers, which either come from the bulk or from the phosphor/insulator interface. The accepted theory for carrier injection in most EL phosphors is tunneling from interface states. While the pure tunneling mechanism will be shown to be temperature independent, there is a slight temperature dependence on the device current. Consequently, this tunneling mechanism is suggested to be thermally assisted [KOB 92].

There are several experimental observations that support the idea that the electrons trapped at the interface are the carrier source, and that the thermally assisted tunneling mechanism is responsible for their injection. First of all, it has been shown that the threshold voltage (field) varies when different top and bottom insulators are used, which suggests that the interface is the source of carriers. Specifically, devices with different top and bottom insulators have demonstrated asymmetric device currents and threshold fields as a function of the polarity of the applied voltage. Second, the observation that the device current is such a strong function of the phosphor field suggests that the tunneling mechanism dominates. Finally, the fact that the electrical properties are only a weak function of temperature rules out a strict thermionic emission process and suggests that tunneling dominates [MIY 93].

Typically, commercial ACTFEL displays are driven at 60Hz with a trapezoidal waveform given by figure 2-10 that has an 8 μs rise and fall time (τ_r, and τ_f, respectively) and a 40 μs pulse width (τ) [ONO 95 p.38]. As the voltage pulse rises, the energy bands begin to bend under the influence of the induced electric field. Eventually, a threshold voltage (or field) is reached when the energy bands are bent enough so that electrons tunnel into the phosphor conduction band from interface states. The tunneling emission current (J) for Shottky barriers is given by [SZE 81 p.403]:

$$\text{(2-2)}\ J \sim E^2 \exp\left[\frac{-8\pi\sqrt{2m^*}\left(q\phi_B\right)^{3/2}}{3qhE}\right]$$

where E is the electric field, m^* is the electron effective mass, q is the charge of an electron, ϕ_B is the barrier height, and h is Planck's constant. For interface trap (or interface state) emission, the expression is virtually the same except that the barrier height term is replaced with a term that represents the interface trap depth. The optimum electron trap depth is a rather delicate balance between two competing processes. Obviously, if the electrons are too deep, the electron injection will not occur until extremely high fields are reached. Conversely, if they are too shallow, electrons will inject at low fields and will not be accelerated to high enough energies to promote luminescence. Empirically, electron state depths of 1.0 - 1.3 eV have resulted in good device performance [KOB 92].

While the phosphor electric field simply depends on the dielectric constant and the thickness of the phosphor and insulator layers, the interface state properties are more difficult to predict and control. Of particular interest is the density of occupied interface states, which limits the current injected in to the ACTFEL device. Extensive studies on metal-semiconductor contacts by Bardeen [BAR 47] and later by Kurtin et al. [KUR 69], revealed that surface and interface state properties are dependent on the covalency/ionicity of the semiconductors bonds [26 #8proposal]. They measured the barrier heights (Φ_B) for many different semiconductors as a function of the metal electronegativity (X_M). They plotted Φ_B versus X_M and found that for most semiconductors the barrier height of the metal-semiconductor contact increased linearly with the metal electronegativity. They defined the "index of interface behavior (S)" to be:

$$(2\text{-}3)\ S \equiv \frac{d\phi_B}{dX_M}$$

which is simply the slope of the Φ_B-X_M plot. Larger S values implied that the barrier height is strongly dependent on the metal electronegativity, and small S values implied that the semiconductor is only weakly dependent to the metal electronegativity.

After compiling S values for many elemental, III-V, and II-VI semiconductors, they plotted the S values versus the corresponding electronegativity difference (ΔEN) of the semiconductor anion and cation. From this plot, they noticed that semiconductors with small ΔEN (more covalent) corresponded to low S values, and as the semiconductor ΔEN increased (became more ionic), the S value increased. To understand the physical significance of these empirical observations, they compared their results to the following expression that correlates the metal-semiconductor barrier height to the density of states (D_s) at the metal-semiconductor interface:

$$\text{(2-4)}\quad \phi_B \simeq c_2\left(\phi_M - \chi\right) + (1 - c_2)\left(\frac{E_g}{q} - \phi_o\right) - \Delta\phi$$

where Φ_M is the metal work function, χ is the semiconductor electron affinity, E_g is the semiconductor bandgap, q is the charge of an electron, Φ_o is the interface fermi level, $\Delta\Phi$ is the image force lowering of the barrier, and

$$\text{(2-5)}\quad c_2 \equiv \frac{\varepsilon_i}{\varepsilon_i + q^2 \delta D_s}$$

where ε_i is the interface permittivity, and δ is the interface thickness.

From equation 2-4 and 2-5, there are basically two limiting cases for D_s which lead to the following results:

1) If $D_s \rightarrow$, then $c_2 \rightarrow 0$ and

$$\text{(2-6)}\quad q\phi_B \simeq (E_g - q\phi_o) - q\Delta\phi$$

2) If $D_s \rightarrow 0$, then $c_2 \rightarrow 1$ and

$$\text{(2-7)}\quad q\phi_B \simeq q\left(\phi_M - \chi\right) - q\Delta\phi$$

To correlate the empirical results to these two limiting cases, one must first understand that the metal work function, Φ_M, is directly proportional to the metal electronegativity, X_M . With this in mind, the two limiting cases for the density of interface states (D_s) can easily be correlated to the semiconductor's bonding properties. When D_s approaches infinity, the barrier height term (equation 2-6) is not a function of the metal work function (or X_M), which corresponds to a low S value. Empirically low S values were characteristic of more covalent semiconductors, so this implies that as the semiconductor becomes more covalent, the density of interface states increases. Conversely, when D_s approaches zero, the barrier height term (equation 2-7) is a function of the metal work function, which corresponds to a large S value. Empirically large S values were characteristic of more ionic semiconductors, so this implies that as the semiconductor becomes more ionic, the density of interface states decreases.

While this is useful in predicting the interface properties of many semiconductors, many of the more covalent semiconductors are not suitable for EL host materials because they tend to have smaller band gaps. Because tunneling from interface states seems to be the dominant mechanism for injecting electrons into the EL phosphor, several groups have explored modifying the phosphor/insulator interface to increase the density of occupied states. In particular, several groups that have introduced thin interfacial layers between the phosphor and insulating layers as a means of increasing the charge injected into the phosphor layer. Kobayashi et al. [KOB 82] and Ohwaki et al. [OHW 90] have investigated the use of insulating SiO_2 and semiconducting germanium, respectively, to increase the charge injection in ZnS:Mn. Britton et al. [BRI 92] investigated thin layers of aluminum (1-5 nm) to modify the phosphor/insulator interface and promote charge injection into the ZnS:Mn system. In each of these studies, it was suggested that the modification of the phosphor/insulator interface introduced trapped electron states that lead to increased electron injection under ac bias. Britton and Ohwaki demonstrated an increase in the brightness for their modified devices, while Kobayashi reported an increase in the conduction charge, but a decrease in the brightness. Kobayashi postulated that the reduced brightness resulted from a reduction in the local electric field at the Ge/ZnS interface.

Electron Acceleration

Once the electrons are tunnel injected into the phosphor layer conduction band, they are accelerated under the influence of the electric field. The electric field in the phosphor layer can be calculated by rearranging Maxwell's equations for series capacitors. The resultant equation for the phosphor electric field (E_p) is [KIN 88]:

$$(2\text{-}8)\quad E_p = \left(\frac{\varepsilon_i}{\varepsilon_i d_p + \varepsilon_p (2) d_i}\right) V_{tot}$$

where ε is the dielectric constant, d is the layer thickness, and the subscripts i and p represent the insulator and the phosphor, respectively (assuming the top and bottom insulators are the same). When substituting typical values for ε_i (20), d_i (300nm [x2]), ε_p (13), d_p (500nm), and V_{tot}(180-220V), the phosphor field ranges between 2.0 and 2.5 MV/cm. At these extremely high electric fields, the injected electrons accelerate to high energies extremely fast. If one assumes loss-free electron transport, the simple expression:

$$(2\text{-}9)\quad En_e(x) = E_p\, x$$

describes the electron energy (En_e) as a function of distance (x) under an electric field E_p. Under these conditions, an electron would gain sufficient energy to impact excite a blue (450nm) EL center in less than 11nm. Because electrons scatter and lose energy by several mechanisms, the electron energy distribution does not obey this simple relationship. The electron energy distribution is a complicated function of high field scattering mechanisms such as intervalley scattering, polar optical phonon scattering, acoustic phonon scattering, ionized impurity scattering, band-to-band impact ionization, and impact excitation [BHA 93]. These scattering mechanisms depend on the energy band properties of the host phosphor.

Numerical Monte Carlo computer simulations of electron high field transport in ACTFEL devices have been investigated by several groups (32,33,34 MachGoodnickBrennan). For these Monte Carlo techniques, there are basically two components that must be considered, namely: 1) the carrier dynamics, and 2) the carrier kinetics. The carrier dynamics are governed by the E(k) dispersion, and the carrier kinetics are controlled by the scattering rates of the different scattering mechanisms listed above. By describing the carrier dynamics and kinetics as a function of electric field, these simulations can be used to calculate the electron energy distribution in ACTFEL devices. Furthermore, if one estimates the impact excitation cross section as a function of energy, the quantum yields of these devices can be approximated.

Initially, Brennan [BRE 88] used a full band ZnS structure to calculate the electron energy distribution for electric fields up to 1 MV/cm. For this electric field region, he concluded that very few electrons obtained sufficient energy to excite Mn luminescent centers. Later, a simple parabolic band model [MAC 90] was used to simulate the high field transport properties in ZnS in which the conduction band was described by a single parabolic band. In addition, this parabolic band model assumed that the electron scattering was dominated by polar optical phonon scattering. These calculations suggested that the electrons in ZnS experienced nearly loss free transport, which is referred to as electron runaway, and resulted in a very energetic electron energy distribution. Later, a non-parabolic conduction band was implemented by Bhattacharyya et al. [BHA 93], where they included scattering due to polar optical phonons, acoustic phonons, intervalley scattering, and ionized and neutral impurities. Figure 2-11 shows the electron distribution [n(E)] generated from these simulations as a function of electron energy (eV). Finally, another simulation using a full band structure was performed in which impact ionization and impact excitation were also included as scattering mechanisms. Figure 2-12 again shows the electron energy distribution generated from these simulations as a function of electric field with a calculated impact excitation cross section for Mn ions. The overlap between the electron energy distribution and the impact excitation is related to the quantum efficiency of the devices.

Another model, the so-called "lucky drift" model, is a more simplistic analytical model which uses the electron mean free path to describe the high field transport properties [BRI 91]. Both the numerical Monte Carlo models and the analytical lucky drift model have made significant contributions to understanding the high field electron transport phenomenon in ACTFEL devices.

Impact Excitation/Ionization

After the electrons accelerate to high enough energies, they can interact with a luminescent center and promote one of the luminescent center's ground state electrons. The electron can either be promoted into a higher atomic state of the luminescent center, or into the conduction band of the host material which is called impact excitation [BRI 91] or impact ionization [BRI 90], respectively (figure 2-13). The electron - luminescent center interaction probability is related to the luminescent center radiative cross section which will be discussed in the phosphor material properties section. When the electron is excited into a higher atomic state (impact excitation), it can relax back into its ground state either radiatively or non-radiatively.

When an electron is promoted into the conduction band of the solid (impact ionization), the excited electron is immediately accelerated toward the anode by the electric field. This type of impact causes electron multiplication and is referred to as avalanche breakdown [SZE 81 p.149]. Subsequent light emission from the ionized luminescent center requires that an electron be recaptured from the conduction band. The recapture rate is extremely low for hot electrons, however, and subsequently this electron recapture event occurs predominantly in low field regions. This type of electroluminescence is a two-step process which changes the relaxation kinetics as compared to impact excited centers [BRI 94]. While the details of the two step recombination process will not be elaborated, the kinetics of the non-radiative and radiative recombination processes will discussed in the following section.

De-excitation

As mentioned previously, de-excitation can occur either radiatively (which produces a photon), or non-radiatively. Typically, non-radiative relaxation occurs by phonon generation which produces heat from lattice vibrations. Figure 2-14 schematically demonstrates these two de-excitation pathways. Local lattice imperfections such as point defects (interstitials, vacancies...), line defects (dislocations), and volume defects (grain boundaries) also act as non-radiative recombination centers which is deleterious to the radiative efficiency. The radiative efficiency as a function of temperature $\eta(T)$ is usually written as [CHO 79]:

$$(2\text{-}10)\ \eta(T) = \frac{I}{I(0)} = \frac{W_R}{W_R + W_{NR}}$$

where W_R and W_{NR} are the radiative and non-radiative recombination rates, respectively. Furthermore, W_{NR} is given by the temperature dependent expression:

$$(2\text{-}11)\ \ W_{NR}(T) = W(0)\exp\left(\frac{-E}{kT}\right)$$

where W(0) is on the order of the lattice vibrational frequency, E is an activation energy, k is Boltzman's constant and T is temperature. From these expressions, it is seen that the non-radiative recombination rate increases with temperature while the radiative recombination rate is temperature insensitive. Subsequently, the radiative efficiency decreases as the temperature increases due to an increase in the non-radiative recombination rate.

For ACTFEL devices, temperature dependent luminescence data is complicated by the electrical properties of the device. For instance, the brightness of a SrS:Ce device was shown to gradually increase with temperature under EL excitation, while it was shown to gradually decrease under PL excitation [TRO 95]. Examination of the device current as a function of temperature showed that the current increased with temperature, which is consistent with the thermally assisted tunneling mechanism. Therefore, while the radiative efficiency of the Ce luminescent center decreased with temperature as equation 2-10 suggests, the simultaneous increase in the device current caused the overall brightness to increase with temperature. While the overall device performance is a function of both the electrical and optical properties, it is useful to understand the optical de-excitation mechanisms independent of the electrical properties.

The radiative decay lifetime of a luminescent center is one measure of the radiative recombination rate and it is governed by two selection rules. While the two selection rules (spin and momentum) will be discussed later, the radiative kinetics for atomic transitions will be elaborated here. In ACTFEL devices, electrons are promoted to an exited state by impact excitation or impact ionization as discussed in the previous section. The de-excitation of electrons in the exited state as a function of time (t) is given by [BLA 94 p.38]:

$$(2\text{-}12)\quad \frac{dN_e}{dt} = -N_e P_{se}$$

where N_e is the number of luminescent centers in the excited state, and P_{se} is the probability of spontaneous emission. Integration of eq. (2-12) yields:

$$(2\text{-}13)\quad N_e(t) = N_e(0)\exp(-P_{se}t)$$

which can be written as:

$$(2\text{-}14)\quad N_e(t) = N_e(0)\exp(-t/\tau_R)$$

where τ_R equals $(P_{se})^{-1}$ and is called the radiative decay lifetime of the transition. From equations 2-13 and 2-14, it is noted that the radiative decay time is simply the reciprical of the spontaneous emission probability. This means that transitions with shorter decay lifetimes have higher spontaneous transition probabilities.

While the radiative decay time of a luminescent center is an important property for ACTFEL phosphors, a fast decay time does not necessarily mean that it will be a good ACTFEL material. Similarly, a slow decay time does not mean that a luminescent center will be necessarily be a poor ACTFEL material. It is often difficult to know, a priori, whether a material will be efficient or not, because one must consider both the electrical and optical characteristics of the material.

Material Properties

Electrodes

Both the standard and inverted ACTFEL device structures require a top and bottom electrode, one of which must be transparent. For the standard device, the first layer that is deposited is the bottom transparent electrode which is typically 300-500 nm thick [RAC 96]. The most common transparent electrode used is indium tin oxide (ITO) which has a resistivity of approximately 5 ohms/square for thicknesses that range from 300-500 nm. Though optically transparent, ITO has a high conductivity because of a high concentration of shallow donors that lie only a few meV below the conduction band. At room temperature, these donors are thermally activated into the conduction band and lead to high conductivity. There are basically two sources believed to contribute to the shallow donor level in ITO, namely: 1) Sn^{+4} sitting substitutionally on an In^{+3} site, and 2) oxygen vacancies. While ITO is the predominant transparent electrode material, ZnO and ZnO:(Al, In, Ga) have also been used for ACTFEL displays. A similar conduction mechanism that is responsible for ITO conduction occurs in ZnO films as well. For un-doped ZnO, a high oxygen vacancy concentration is believed to induce a shallow donor level, and for the doped ZnO, Al, In, and Ga all have a +3 valence state which act as shallow donors when substituting for the Zn^{+2} site [CHO 83].

The top electrode is the last layer that is deposited for the standard thin film device and it typically has a thickness range of 300-500nm. Because there is no further processing steps after this metallization layer is deposited, there are no temperature restrictions for the top electrode. The main requirement for the top electrode is that it has to have a low resistivity. In addition, it must be resistant to electromigration under high electric fields [ONO 95 p.68]. Aluminum is frequently used as the top electrode in standard ACTFEL devices because of its good conductivity, its resistance to ion migration as well as processibility [RAC 96]. One drawback of aluminum, however, is its extremely high reflectivity. External light that penetrates into the ACTFEL device is reflected back by the aluminum which has negative effects on the contrast of the display. Filters are often used to suppress this light back reflection so only the light generated in the device is observed by the viewer. For inverted structures, the opaque electrode is the first layer that is deposited. Therefore, depending on the highest temperatures that are experienced during subsequent processing, alternative refractory metals such as molybdenum and tungsten are often used.

Insulators

ACTFEL devices impose rather stringent property requirements on the insulating layers, which has limited the number of insulating materials suitable for practical devices. The most important requirements for the insulating layers are 1) a high dielectric constant, 2) a high electric field strength 3) a uniform thickness, and 4) the layer must be pinhole free. Of these requirements, the dielectric constant and electric field strength are materials dependent, while the thickness uniformity and the pinhole density are process dependent.

The high dielectric constant requirement for insulators can be justified by applying Maxwell's equations to an EL device below the threshold voltage. As discussed earlier, the threshold is defined to be the maximum voltage or field that marks the onset of the Zener breakdown of the semiconducting phosphor. To optimize device performance, careful consideration must be given to maximize the electric field across the phosphor layer, and minimize the field across the insulators. As described previously, below the threshold voltage the device can be approximated as three series capacitors with the applied electric field drop across each layer is given by:

$$(2\text{-}15)\quad \varepsilon^{t}_{i}E^{t}_{i} = \varepsilon_{p}E_{p} = \varepsilon^{b}_{i}E^{b}_{i}$$

where E is the electric field, ε is the dielectric constant at the frequency of operation, subscript i and p represent the insulators (t = top, and b = bottom) and the phosphor layers, respectively. Furthermore, the voltage drop across each layer is simply the product of the electric field in each layer and the thickness (d) of each layer. The total applied voltage (V_{tot}) is divided between each layer according to the following equation:

$$(2\text{-}16)\quad V_{tot} = E^t_i d^t_i + E_p d_p + E^b_i d^b_i\ .$$

Equation 2-15 and 2-16 demonstrate that the threshold, or turn-on, characteristics of an ACTFEL device are a function of the dielectric constant and the thickness of each layer in this three series capacitor structure. To maximize the phosphor electric field, the insulators should have a high dielectric constant and a sufficient electric field strength to avoid breakdown. In addition, the insulators should be processed as thin as possible without compromising device reliability. Generally, as the insulator film thickness decreases, device reliability gets worse because pinholes in the films cause localized high field regions which results in premature dielectric breakdown.

A survey of the insulators that have been tested for ACTFEL devices reveals that, as the dielectric constant increases, the electric field strength decreases. Because these properties are usually inversely proportional to one another, Howard introduced a figure of merit for insulator materials [HOW 77]. The figure of merit is simply the product of the dielectric constant and the electric field strength of the insulator. Figure of merits for several insulators have been tabulated and a range of 2-25 C/cm has been reported [ONO 95 p.65]. Table 2-1 lists several insulating materials used in ACTFEL devices; included in the table is the dielectric constant, the electric field breakdown strength, the figure of merit, and the breakdown mode of the material. Unfortunately, the high dielectric constant insulators ($SrTiO_3$, $BaTiO_3$, and $PbTiO_3$) that have yielded the highest figure of merits (19-25 C/cm), exhibit "propagating breakdown." In these materials, when breakdown initiates it catastrophically spreads and destroys the device. Lower dielectric constant insulators (Al_2O_3, Si_3N_4, TiO_2, $BaTa_2O_6$...) that have lower figure of merits (3-7 C/cm) have proven to be more practical for EL devices. These materials have so-called "self-healing" breakdown which inherently isolates the localized breakdown and prevents catastrophic breakdown.

Phosphors

Many efficient cathodoluminescent (CL) phosphors that have been developed for CRT applications, have been investigated as EL phosphors. These investigations however, have shown that the most efficient red (Y_2O_2S:Eu), green (ZnS:Cu,Au,Al), and blue (ZnS:Ag,Cl) CL phosphors are poor EL phosphors. While the reason for the poor EL efficiency of the Y_2O_2S:Eu phosphor is beyond the scope of this review, the poor efficiency for the ZnS:Cu,Au,Al and ZnS:Ag,Cl phosphors can be easily understood by examining the fundamentals of their emission processes.

Under excitation from a highly energetic beam of electrons (1-30 keV), electrons in the ZnS valence band (VB) are exited into the conduction band (CB). Subsequently many electron-hole (e-h) pairs are created. These electrons and holes then drift through the phosphor material and are eventually trapped by donor levels (Al, and Cl) and acceptor levels (Cu, Au, and Ag) in the ZnS. These electrons and holes eventually recombine with the photon energy being equal to:

$$(2\text{-}17)\ h\nu = BG - BE(d) - BE(a)$$

where BG is the ZnS bandgap, BE(d) is the binding energy of the donor level, and BE(a) is the binding energy of the acceptor level (Figure 2-15). When electrons and holes are trapped in close proximity to one another this e-h recombination is favorable and very high efficiencies result.

Under EL excitation, a large electric field (>1 MeV/cm) is induced across the phosphor layer. Subsequently, when electrons are excited into the CB and holes are created in the VB, the presence of the electric field transports the electrons toward the positive polarity and holes toward the negative polarity as shown in figure 2-16. This spatially separates the electrons and holes which prevents radiative recombination from occurring. Even when an electron or hole is trapped by the donor or acceptor level, respectively, the depth of these levels are usually shallow enough that they tunnel back into the CB or VB under the high fields. This electric field dependent luminescence phenomenon is referred to as field quenching. Because the donor-acceptor recombination phosphors are inefficient under high electric fields, a different class of phosphors is necessary for ACTFEL devices. These phosphors consist of a semiconducting host material doped with a transition metal or rare earth lumimescent center. The radiative recombination event in these phosphors is an atomic transition which occurs locally at the luminescent center. While the two constituents (host material and luminescent center) of an EL phosphor make up a unique material system, each constituent has a distinct function in the electroluminescence phenomenon and will be discussed separately.

Host materials

One of the most important requirements that the host material must satisfy is the bandgap must be larger than the energy of the photons generated by the luminescent center. For display applications, this implies that the bandgap of the host must be greater than 1.7 - 3.1 eV, to ensure that absorption of visible light does not occur. Another important requirement that the host material must have is good high field transport properties. Though there has been some disagreement as to energy range of the high energy electron distribution that are achieved in these devices, it is recognized that the high field charge transport properties of the host material is critical. As discussed earlier, extensive parabolic [MAC 90], non-parabolic multivalley [BHA 93], and full band model calculations [BRE 88] have been used to better understand these high electron energy loss mechanisms in EL devices.

Another important property that is partially controlled by the EL host material is the turn-on characteristics. Because these devices are high field devices, the host material must also have a high dielectric strength, usually greater than 1MeV/cm. As discussed already, the phosphor/insulator interface state density and interface state depth is typically dominated by the host material. The density of interface states dictates the total current transported in the device, and the depth of these states dictates the thermally assisted electron tunneling process which is responsible for the device turn-on. Finally, the host material also interacts with the luminescent center which affects the energy and probability of the radiative relaxation process.

While several host materials have been explored, the most efficient EL host materials are metal sulfides, where the most common metals are Zn, Ca, Sr, or Ca-Sr-Ga. Of these host materials, ZnS is by far the most widely studied and also the most commonly used host material for commercial ACTFEL displays. ZnS has a bandgap of 3.8 eV which makes it transparent to visible light so optical absorption in the phosphor layer is minimal. The dielectric breakdown strength of ZnS is about 1 MeV/cm, which allows the electrons to reach high enough energies so efficient excitation of the luminescent centers is accomplished. While the interface states properties can also be insulator dependent, evidence suggests that ZnS promotes a high density of interface states. In addition, these states are sufficiently deep (1.0 - 1.3 eV) which results in its exceptional turn-on characteristics [BRI 94].

Luminescent centers

While the host material dominates the electrical properties of the phosphor layer, the luminescent center dominates the optical emission properties of the phosphor layer. When discussing the luminescent center constituent, three aspects must be considered: namely the radiative kinetics, the cross section for excitation, and the radiative transition energy. The cross section for excitation is related to the probability that a high energy electron will impact excite or ionize a luminescent center in the phosphor material. To a first order approximation, the cross section for excitation is proportional to the geometric cross section of the ionized luminescent center when substituted in the host matrix [MAC

91]. The power efficiency (η) of the device is directly proportional to the cross section of luminescent center and is expressed by the following equation [BLA 94 p.213]:

$$(2\text{-}18)\ \eta = \frac{h\nu\sigma N}{eE}$$

where hν is the photon energy, σ is the excitation cross section, N is the optimum luminescent center concentration, e is the charge of an electron, and E is the electric field. From equation 2-18 it is clear that a large cross section is desirable for efficient devices.

While the cross section of the luminescent center is important when describing the probability of the excitation, the radiative transition energy dictates the emitted photon energy and therefore its color. As described earlier, for some luminescent materials the radiative mechanism is an electron-hole pair recombination whose energy is a function of the properties of the solid. This event can either be a conduction band to valence band, conduction band to acceptor state, donor state to valence band, or donor state to acceptor state recombination (Figure 2-17). The photon energy is a measure of the energy separation of the initial and final states of the recombination event. These positions depend on the electronic properties of the solid which are described quantum mechanically by Schroedinger's equations. In most ACTFEL devices however, the radiative mechanism is an atomic transition. The atomic transition energy is not dominated by the properties of the solid, but rather the elemental or free ion quantum properties of the luminescent center. Though this radiative event occurs by intershell and intrashell transitions localized at the luminescent center, the photon energy can be affected host material [DUF 90 p.40].

Fundamentals of Atomic Transitions

Atomic transitions can be catagorized as either intershell transitions or intrashell transitions depending on the quantum numbers of the initial and final state. Electrons involved in intershell transitions undergo a change in the angular momentum quantum number (*l*), while intrashell transitions occur between states in the same quantum shell. The probability of an optical transition (absorption or emission) is a function of the initial state and final state wavefunction and is represented by a term called the oscillator strength. It can be shown mathematically that certain intershell transitions are allowed, and intrashell transitions are forbidden.

The oscillator strength (*f*) can be expressed as [DUF 90 p.36]:

$$(2\text{-}19)\, f = \frac{8\pi^2 mc}{3he^2} G\nu M^2$$

where m is the electron mass, c is the speed of light, h is planks constant, e is the charge of an electron, ν is the frequency, G is a parameter which relates to the degeneracy of the transition and M is the transition moment. The wavefunction dependency of *f* comes from the transition moment function which is given by:

$$(2\text{-}20)\quad M^2 = M_x^2 + M_y^2 + M_z^2$$

where

$$\text{(2-21)}\ M_x = \int \psi_m^* \Sigma e_i x_i \psi_n d\tau$$

where the integral $\int d\tau$ is over all space, ψ^*_m is the wavefunction of the final state, $\Sigma e_i x_i$ is the x component of the dipole, and ψ_n is the wavefunction of the initial state. The expressions for M_y and M_z are similar to equation 2-21. While the mathematical details will not be pursued here, the following qualitative examination of equation 2-21 demonstrates the origin of one of the optical transition selection rules [DUF 90 p.38].

This relatively simple proof is based on the premise that the transition moment is an intrinsic property of the atom or ion so its value should not change by the application of a symmetry operation. This implies that the transition moment function must be even because upon inversion, an odd function changes sign. This condition means if the function is odd, the transition moment, and subsequently the oscillator strength, is zero which results in a forbidden transition. From this argument, one can examine the three components that contribute to the transition moment function (i.e., ψ_n - the initial state wave function, ψ^*_m - the final state wavefunction, and $\Sigma e_i x_i$ - the dipole moment) and determine what conditions make the transition moment even (allowed) and which conditions make it odd (forbidden). Inspection of the dipole moment contribution, reveals that this function is odd. Therefore, to make the entire function even, this requires that the wavefunction of the initial state or the final state be even and the other wavefunction be odd. The result of this proof is the so-called Laporte selection rule which can be expressed by:

$$\text{(2-22)}\ \Delta l = \pm 1$$

where Δl is the change in the angular momentum quantum number. For an electronic dipole transition to be allowed, the angular momentum (or azimuthal) quantum number must change by factor of |1|. Applying the Laporte selection rule to the two types of atomic transitions demonstrates that intrashell transitions (d-d, f-f...) are forbidden and certain intershell transitions (s-p, p-d, d-f...) are allowed.

The second selection rule for optical transitions is called the spin selection rule. It is expressed by:

$$\text{(2-23)}\quad \Delta s = 0$$

where s is the spin quantum number (i.e., $\pm\frac{1}{2}$) of the electron. This rule simply implies that for an optical transition to occur, the spin state of the electron in the initial and final state must be the same. This selection rule comes from the fact that there is no spin associated with a photon.

While these selection rules are general and apply to all optical transitions, the oscillator strengths are often non-zero for Laporte and/or spin forbidden transitions. There are several mechanisms that relax these selection rules and cause otherwise forbidden transitions to emit or absorb rather efficiently. The Laporte selection rule can be relaxed by vibrations in the lattice which result in vibronic transitions that have a non-zero oscillator strength. In addition, Laporte forbidden transitions can be relaxed when the atom or ion is in placed in a site without a center of symmetry (i.e., tetrahedral). This mechanism is very important to ACTFEL technology because the brightest red and green ACTFEL phosphors are Laporte forbidden and are efficient because ZnS lattice sites are tetrahedral. Finally, a relaxation of the spin selection rule occurs because of spin-orbital coupling; in particular when the spin-orbital coupling becomes large, rather intense spin forbidden transitions are observed [SOB 79 p.27].

Term Symbols

For systems that only have one outer shell electron, the electron states can be conveniently represented by their quantum numbers. When multi-electron systems are considered however, it is more convenient to represent the electron states with term symbols [SOB 79 p.20]. This representation is important to understand, because atomic transitions for transition metals and rare earths are often represented in this manner. A term symbol has the general form ${}^{2S+1}L_J$, where 2S+1 is the multiplicity of the of a term, L is the total orbital angular momentum of a term, and J is the total angular momentum of a term. The multiplicity of a term (2S+1) is determined by adding up the total spin angular momentum (S) of an atom or ion. This is done by simply counting the total number of unpaired spin electrons and multiplying this number by $\frac{1}{2}$. The L term represents the total orbital angular momentum, and is denoted by capital letters as follows:

L = 0 (S), 1 (P), 2 (D), 3 (F), 4(G), 5 (H), 6 (I), 7 (K), 8 (L), 9 (M), 10 (N).

Finally J is just the sum of the spin and angular momentum ($J = L + S$). While this nomenclature is rather straightforward, electron orbital and spin interactions cause the number of terms to increase rapidly for multiple electron systems.

ACTFEL Phosphor Materials

Currently there are two approaches that are being pursued to develop a full color ACTFEL display, namely: 1) red-green-blue (RGB) displays, and 2) color-by-white. For RGB displays, the red, green, and blue phosphor layers are patterned so that each pixel is divided up into four regions that contain a red, green and two blue phosphor regions (Figure 2-18). In the color-by-white approach, each pixel has a phopshor layer (or layers) that produces white light that is subsequently filtered by a red, green, or blue filter (Figure 2-19). Bright red and green ACTFEL phosphors have been developed for the RGB approach, however, a brighter blue phosphor still needs to be developed. Similarly, several white ACTFEL phosphor systems have been explored, however, the blue contribution is stll too dim for many full color applications. In this section, the current status of red, green, and white ACTFEL phosphor systems will be summarized. Particular attention will be given to the blue phosphors in subsequent chapters as this is subject matter of this dissertation.

Table 2-2 [RAC 96] is a list of some the ACTFEL phosphor systems that have been investigated with their corresponding efficiency (lum/W), L_{40} (cd/m^2), CIE x and y, and peak wavelength (nm). Table 2-3 lists specific elemental/ionic properties of the anions and cations that make up the host matrix and finally, table 2-4 lists specific elemental/ionic properties of the most important transition metal and rare earth luminescent centers.

Red

ZnS:Mn

ZnS:Mn is the brightest most efficient ACTFEL phosphor that has been developed. It has a luminance of 300 cd/m^2 of lum and an efficiency of 5 lum/W. In this phosphor system, Mn^{+2} ions substitute directly on Zn^{+2} lattice sites (Mn$_{Zn}$). Figure 2-20 shows the emission spectra of ZnS:Mn which results from the Mn $^4T_1(3d)$-$^6A_1(3d)$ intrashell transition (group theory notation). Because the Mn^{+2} transition is an intrashell transition (3d-3d), there is no angular momentum difference between the ground state and the excited state ($\Delta l=0$). Consequently, this transition should be forbidden by the Laporte selection rule. This selection rule is relaxed however, because the Mn^{+2} ions substitute directly on Zn^{+2} lattice sites (Mn$_{Zn}$) which have tetrahedral symmetry. As discussed earlier, parity or Laporte forbidden transitions can be efficient if the lattice site they are sitting in does not have a center of symmetry. Figure 2-21 shows the tetrahedral arrangement of the Mn$_{Zn}$ ion.

By examining the electron configuration of the Mn^{+2} ion (Table 2-4), it is clear that the 3d orbitals are not shielded from the host lattice by any occupied orbials. Therefore, the host lattice can be modified to change energy difference between the excited state and the ground state. Recently a Zn$_{1-x}$Mg$_x$S:Mn EL phosphor was introduced, in which the Mn^{+2} peak emission was systematically shifted from 585nm for pure ZnS:Mn to 550nm for the Zn$_{0.68}$Mg$_{0.32}$S:Mn composition [MIK 96]. When a solid solution of Zn$_{1-x}$Mg$_x$S:Mn is formed, the lattice parameter (and subsequently the bond distance) decreases linearly according to Vegard's law:

$$(2\text{-}24)\quad a_{o(Zn_{1-x}Mg_xS:Mn)} = (1-x)\times a_{o(ZnS)} + (x)\times a_{o(MgS)}$$

where a_o is the lattice parameter. As x increases and the lattice parameter decreases, the 3d energy levels feel a stronger influence from the nearest neighbor sulfur ligands. This causes the 3d energy levels involved in the radiative transition to become farther apart which increases the transition energy.

From figure 2-20, it is observed that the ZnS:Mn emission spectra is a broad band. This broad band is due to longitudinal (LO and LA) and transverse optical and acoustic (TO and TA) phonons which are not resolvable at room temperature, but can be detected at low temperature. These phonon replicas arise because there is strong coupling between the Mn 3d orbitals and the ZnS host lattice. Though the excitation mechanism in PL differs from EL, the radiative de-excitation mechanism from the excited state to the ground state is the same. Therefore, low temperature PL spectroscopy can be a valuable tool in determining detailed information about radiative transitions in ACTFEL phosphors.

The ZnS:Mn broad band transition is actually yellow in color, and is used in most of the commercial monochrome ACTFEL display applications. It is often catagorized as a red phosphor however, because the high energy portion of the broad band can be filtered out to produce a red emission. Tuenge and Kane [TUE 91] developed a CdSSe filter for the ZnS:Mn phosphor that resulted in a CIE color coordinates that are very close to the CRT standard. Though the ZnS:Mn brightness and efficiency obviously decreases when filtered, the CdSSe filtered ZnS:Mn is currently the brightest (70 cd/m^2) and most efficient (0.8 lum/W) red ACTFEL phosphor.

CaS:Eu

The highest brightness and efficiency achieved thus far for CaS:Eu is 12 cd/m^2 and 0.05 lum/W [TAN 89]. In this phosphor system, Eu^{+2} ions substitute for Ca^{+2} lattice sites (Eu$_{Ca}$). Figure 2-22 shows the deep red emission spectra of CaS:Eu which results from the Eu^{+2} ^{7}F(5d)-^{8}S$_{7/2}$(4f) transition, and also the relative positions of the ground state and the excited state. The Eu^{+2} transition is an intershell transition (5d-4f), therefore there is an angular momentum difference between the ground state and the excited state ($\Delta l=1$). Consequently, this transition is allowed by the Laporte selection rule. Because Eu^{+2} is a lanthanide rare earth ion, the 5d orbitals are not shielded from the host lattice by any occupied orbitals. Therefore, the host lattice affects the excited 5d state, and subsequently the photon energy generated by the Eu^{+2} radiative transtion.

The CaS host lattice is has the NaCl structure, therefore when Eu substitutes for Ca it has octahedral symmetry. Figure 2-23 shows the octahedral arrangement of the Eu$_{Ca}$ site. Because the excited 5d orbitals are unshielded, modification of the CaS host lattice is expected to modify the radiative transition energy. Alloying the CaS:Eu phosphor with Se to form CaS$_x$Se$_{1-x}$:Eu has been shown to increase the luminance (25 cd/m^2) and efficiency (0.25 lum/W) by shifting the emission spectra toward slightly higher energy [YOS 89]. Though the color purity for the CaS:Eu and CaS$_x$Se$_{1-x}$:Eu are superior to other red EL phosphors, its low brightness has made them impractical for commercial displays.

Similar to ZnS:Mn, the CaS:Eu emission spectra is a broad band. This broad band is also due to phonon broadening. While the Eu 4f levels do not couple strongly with the CaS lattice, there is strong coupling between the Eu 5d orbitals and the CaS host lattice. Yamashita et al. [YAM 95] have performed low temperature PL studies on CaS:Eu powders and have resolved the phonon replicas in this material and have determined accurately the ground state and excited state energy positions of the Eu in CaS.

Green

ZnS:Tb

The brightest and most efficient non co-doped ZnS:Tb ACTFEL device has a brightness of 90 cd/m^2 and an efficiency of 0.6 lum/W. In the ZnS:Tb phosphor system, Tb^{+3} ions substitute for Zn^{+2} lattice sites (Tb$_{Zn}$). In this system, there is a valence mismatch and an ionic radius mismatch between the Tb^{+3} and Zn^{+2} therfore it is difficult to get large concentrations of Tb into the ZnS host matrix. Figure 2-24 shows the green emission spectra of ZnS:Tb which results from the Tb^{+3} $^5D_4$(4f)-$^7F_6$(4f), $^5D_4$(4f)-$^7F_5$(4f), $^5D_4$(4f)-$^7F_4$(4f), $^5D_4$(4f)-$^7F_3$(4f) transitions, as well as the relative energy level positions. The Tb^{+3} transitions are all intrashell transitions (4f-4f), therefore there is no angular momentum difference between the ground state and the excited state ($\Delta l=0$). Consequently, this transition is also forbidden by the Laporte selection rule, but its tetrahedral symmetry in the ZnS lattice helps relax this condition. Because Tb^{+3} is a lanthanide rare earth ion, the 4f orbitals are shielded from the host lattice by the 5s and 5p occupied orbitals. Therefore, the transition energy between the ground state and excited state of the Tb^{+3} luminescent center is not affected by the host lattice.

Again the ZnS host lattice is has the zincblende crystal structure, therefore when Tb substitutes for Zn it has tetrahedral symmetry. Figure 2-25 shows the tetrahedral arrangement of the Tb_{Zn} site. While the tetrahedral symmetry of the Tb ion in the ZnS lattice slightly relaxes the Laporte selection rule, because the 4f orbitals are shielded by the 5s and 5p electrons, there is not as much admixing of the 4f electron states compared with the 3d orbitals of the Mn orbitals. Consequently, ZnS:Tb is not as effecient as ZnS:Mn. To help increase the efficiency of the ZnS:Tb phosphor, so called lumocens (luminescent molecular centers) [GOD 94] have been introduced into this material system which has dramatically increased the brightness and efficiency. Lumocens are rare earth complex centers that have a higher efficiency than there rare earth ion counterparts.

In the case of ZnS:Tb, oxygen and fluorine have been introduced into this phoshor to improve the device performance. Sohn et al. [SOH 92], attributed the improved performance to better cyrstallinity which decreases competing non-radiative recombination sites. In addition, they suggested the formation of TbOF complex centers which agreed with the findings of Okamoto et al. [OKA 89]. Chemical analysis of the ZnS:TbOF films showed that devices with a Tb/(O-F) ratio close to unity had the highest brightness which supports the idea that TbOF lumocens are formed. The proposed positions for the O and F ions relative to the Tb are as follows: F^{-1} sits in nearby interstitial sites which compensates for the valence mismatch between Tb and Zn, and the O ion substitutes isoelectronically on a nearby sulfur site. This complex center lowers the symmetry of the Tb luminescent center, and because O and F are very electronegative ions, they can strongly polarize the 5s and 5p orbitals [GOD 94]. Both of these mechanisms should increase the oscillator strength of the Tb radiative transitions by further relaxing the Laporte selection rule. In addition, the lumocen has a larger cross section for excitation verses a lone rare earth ion, which also improves the overall efficiency of the device. ZnS:TbOF devices with a luminance of 100 cd/m^2 and efficiencies of 1.3 lum/W have been routinely achieved.

Contrary to the ZnS:Mn and CaS:Eu, the ZnS:Tb transitions are not broad band transitions, rather it consists of narrow so-called line transitions. As already discussed, these Tb radiative transitions occur between 4f levels which are shielded from the host lattice. Because both the ground state and excited state are shielded from the host lattice, niether level couples strongly to the lattice. Therefore, vibrations in the lattice do not affect the Tb transition and only the zero-phonon line is observed even at low temperature.

White

SrS:Eu,Ce

By doping SrS with both Eu and Ce, a white phosphor with a luminance of 36 cd/m^2 and an efficiency of 0.20 lum/W has been produced. The emission processes for the SrS:Eu,Ce are basically the same as for pure SrS:Eu and SrS:Ce system, however, when they are mixed, a white color is achieved (figure 2-26). Mita [MIT 91] demonstrated a prototype multicolor display by using red, green and blue filters, while Tanaka [TAN 92] showed a white ACTFEL display with this material system. One advantage of the

SrS:Eu,Ce white phosphor is the fact that only one phosphor layer has to be deposited. Because SrS is the common host, both Ce and Eu can be introduced simultaneously which significantly reduces the number of processing steps. Though processing the SrS:Eu,Ce phosphor is relatively simple, significant improvements in the overall brightness still needs to be accomplished if it is to be used as a filtered RGB display.

ZnS:Mn/SrS:Ce

Currently, the ZnS:Mn/SrS:Ce multilayered white phoshor has demonstrated the best color-by-white performance with a luminance of 450 cd/m^2 and an efficiency of 1.6 lum/W. Again, the emission processes for each layer does not change, rather, the individual colors simply mix to produce a white light (figure 2-27). Filtered RGB displays with luminances of 80, 170, and 15 cd/m^2 (red, green and blue, respectively) have been achieved by filtering with organic dyes [LEP 93]. While these luminances are sufficient for RGB multicolor displays, the blue CIE coordinates (x=0.21, y=0.32) need to be shifted to a deeper blue for full-color applications. Because two different phosphor layers must be deposited for the ZnS:Mn/SrS:Ce system, there are extra processing steps involved compared to the SrS:Eu,Ce phosphor. However, relative to patterning three different phosphors for an RGB display, the filtered ZnS:Mn/SrS:Ce approach is much simpler to process.

Table 2-1. ACTFEL Insulators and Properties [ONO 95]

Material	**Relative Dielectric Constant (ε_r)**	**Dielectric Breakdown Strength (MV/cm)**	**Figure of Merrit (lC/cm^2)**	**Breakdown Mode**
TiO_2	60	0.2	1	Propagating
SiO_2	4-6	6-7	2-4	Self Healing
Sm_2O_3	15	2-4	3-5	Self Healing
Y_2O_3	12	3-5	3-5	Self Healing
A_2O_3	8	5-8	3.5-6	Self Healing
Ta_2O_5	23-25	1.5-3	3-7	Self Healing
$BaTiO_3$	14	3.3	4	Self Healing
Si_3N_4	8	6-8	4-6	Self Healing
$BaTa_2O_6$	22	3.5	7	Self Healing
$PbTiO_3$	150	0.5	7	Propagating
Ta_2O_5-TiO_2	20	7	12	Self Healing
$SrTiO_3$	140	1.5-2	19-25	Propagating
$SR(Zr,Ti)O_3$	100	3	26	Propagating

Table 2-2. ACTFEL Phosphor Materials and Device Performance [RAC 96]

Phosphor Material	**Color**	**Luminance L40 at 60Hz** (cd/m^2)	**Efficiency** (lm/W)	**Peak Wavelength** (nm)	**CIE coordinates**	
					x	**y**
ZnS:Mn	yellow	300	5	585	0.65	0.35
ZnS:Mn/filter	red	70	0.80	610	0.65	0.35
ZnS:Sm,Cl	red	12	0.08	650	0.64	0.35
CaS:Eu	red	12	0.05	650	0.68	0.31
CaSSe:Eu	red	25	0.25	620	0.66	0.33
ZnS:TbOF	green	100	1.30	545	0.30	0.60
ZnS:Tb	green	90	0.60	545	0.30	0.60
CaS:Ce,Cl	green	10	0.10	505	0.27	0.53
$ZnGa_2O_4$:Mn	green	10	0.20	501	0.08	0.68
Zn_2SiO_4:Mn	green	10	0.20	510	0.15	0.68
SrS:Ce,F	blue-green	16	0.40	478	0.17	0.37
SrS:Ce,Mn,Cl	blue-green	105	1.63	508	0.30	0.50
SrS:Ce	blue-green	100	0.80	515	0.30	0.50
SrS:Ce/filter	blue	10	0.10	480	0.13	0.18
ZnS:Tm,F	blue	0.2	<0.01	450	0.15	0.15
$SrGa_2S_4$:Ce	blue	5	0.02	445	0.15	0.10
$CaGa_2S_4$:Ce	blue	10	0.04	460	0.15	0.19
SrS:Ce,Eu	white	36	0.20	490	0.37	0.39
ZnS:Mn/SrS:Ce	white	450	1.6	580	0.42	0.48

Table 2-3. Anion and Cation Properties for Common ACTFEL Host Materials

Atom	**Ion (Valence State)**	**Electron Configuration**	**Ionic Radius (Angstroms)**
Zinc (Zn)	$Zn^{(+2)}$	$1s^2 2s^2 2p^6 3s^2 3p^6 3d^{10} 4s^2$	0.74
Gallium (Ga)	$Ga^{(+3)}$	$1s^2 2s^2 2p^6 3s^2 3p^6 3d^{10} 4s^2 4p^1$	0.62
Calcium (Ca)	$Ca^{(+2)}$	$1s^2 2s^2 2p^6 3s^2 3p^6 4s^2$	0.99
Strontium (Sr)	$Sr^{(+2)}$	$1s^2 2s^2 2p^6 3s^2 3p^6 3d^{10} 4s^2 4p^6 5s^2$	1.13
Oxygen (O)	$O^{(-2)}$	$1s^2 2s^2 2p^4$	1.4
Sulfur (S)	$S^{(-2)}$	$1s^2 2s^2 2p^6 3s^2 3p^4$	1.84
Selenium (Se)	$Se^{(-2)}$	$1s^2 2s^2 2p^6 3s^2 3p^6 3d^{10} 4s^2 4p^4$	1.98

Table 2-4. Luminescent Center Properties

Atom	**Ion**	**Atom Electron Configuration**	**Ionic Radius**
Manganese (Mn)	$Mn^{(+2)}$	$1s^2 2s^2 2p^6 3s^2 3p^6 3d^5 4s^2$	0.8
Cerium (Ce)	$Ce^{(+3)}$	$1s^2 2s^2 2p^6 3s^2 3p^6 3d^{10} 4s^2 4p^6$ $4f^2 5s^2 5p^6 6s^2$	1.1
Europium (Eu)	$Eu^{(+2)}$	$1s^2 2s^2 2p^6 3s^2 3p^6 3d^{10} 4s^2 4p^6$ $4f^7 5s^2 5p^6 6s^2$	1.12
Terbium (Tb)	$Tb^{(+3)}$	$1s^2 2s^2 2p^6 3s^2 3p^6 3d^{10} 4s^2 4p^6$ $4f^9 5s^2 5p^6 6s^2$	1.01

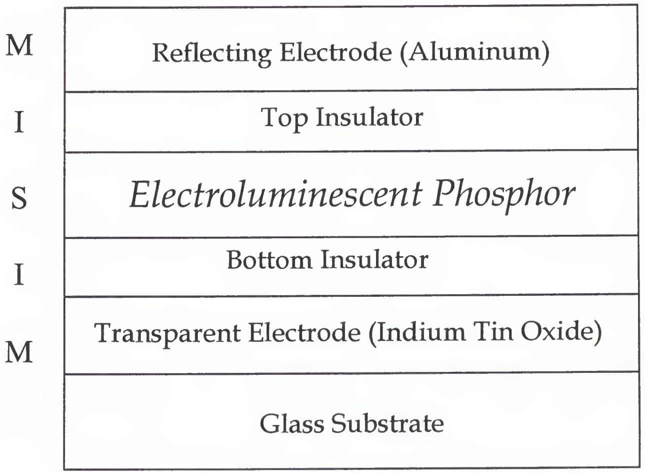
M
Reflecting Electrode (Aluminum)
I
Top Insulator
S
Electroluminescent Phosphor
I
Bottom Insulator
M
Transparent Electrode (Indium Tin Oxide)
Glass Substrate

Figure 2-1. MISIM (metal-insulator-semiconductor-insulator-metal) structure for an ACTFEL device.

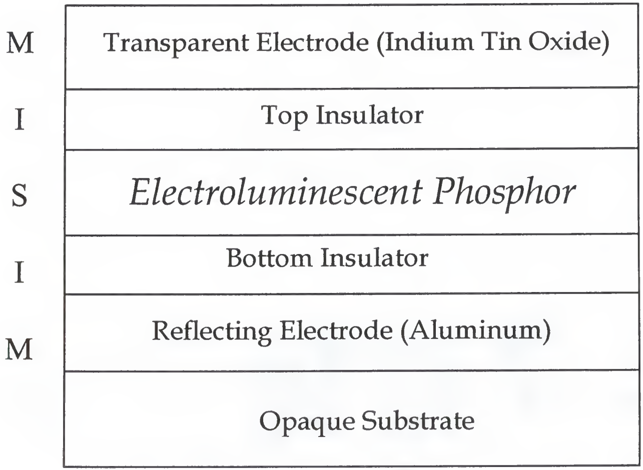
M
Transparent Electrode (Indium Tin Oxide)
I
Top Insulator
S
Electroluminescent Phosphor
I
Bottom Insulator
M
Reflecting Electrode (Aluminum)
Opaque Substrate

Figure 2-2. Inverted structure for an ACTFEL device.

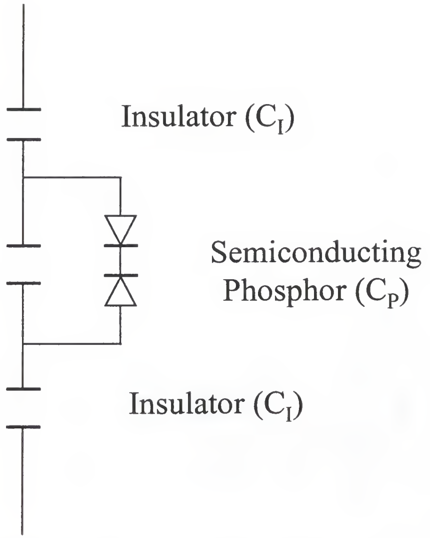

Figure 2-3. Equivalent circuit diagram for an ACTFEL device. C_I and C_P are the insulator and phosphor capacitance, respectively.

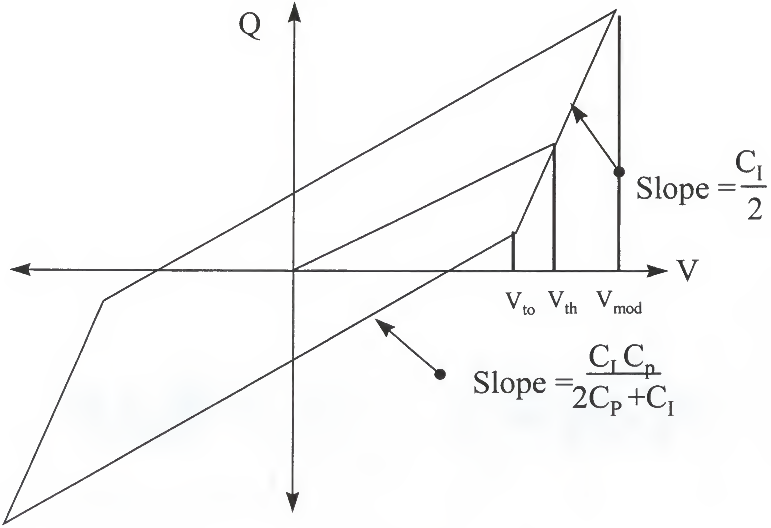

Figure 2-4. Schematic diagram of a Charge-Voltage (Q-V) plot (see text for details).

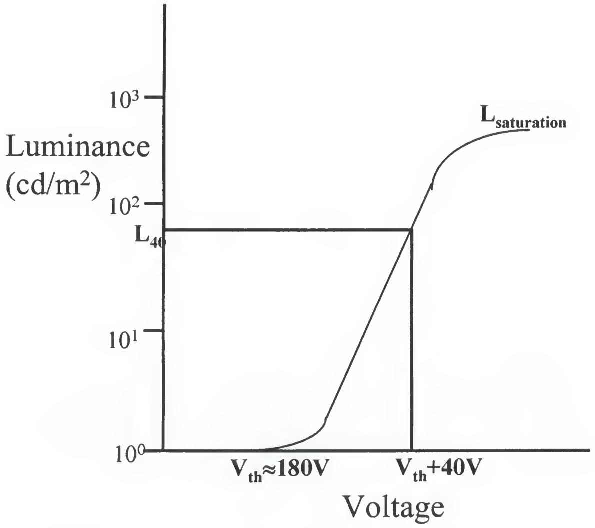

Figure 2-5. Schematic diagram of a Luminance-Voltage (L-V) plot (see text for details).

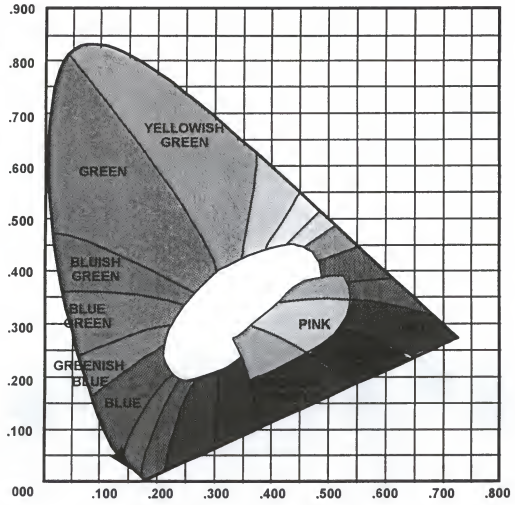

Figure 2-6. Schematic diagram of the 1936 CIE diagram.

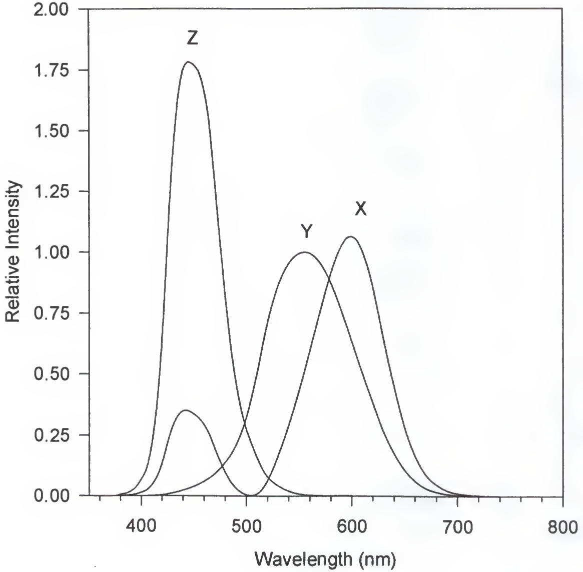

Figure 2-7. Plot of the CIE tristimulus curves.

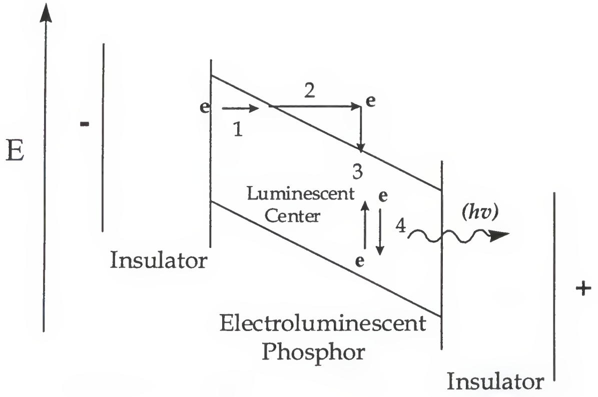

Figure 2-8. Four mechanisms that occur in an ACTFEL device: 1) tunnel emission of electrons from interface states, 2) acceleration of electrons to high energies, 3) impact excitation or impact ionization of the luminescent center, and 4) de-excitation of the excited electron by radiative (photon generation).

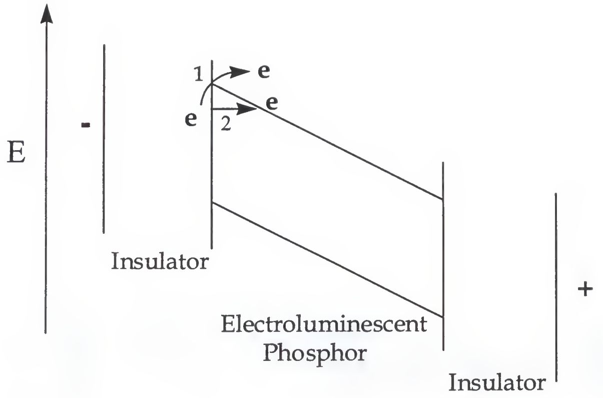

Figure 2-9. Schematic diagram of two carrier injection mechanisms: 1) thermionic, and 2) field emission or tunneling.

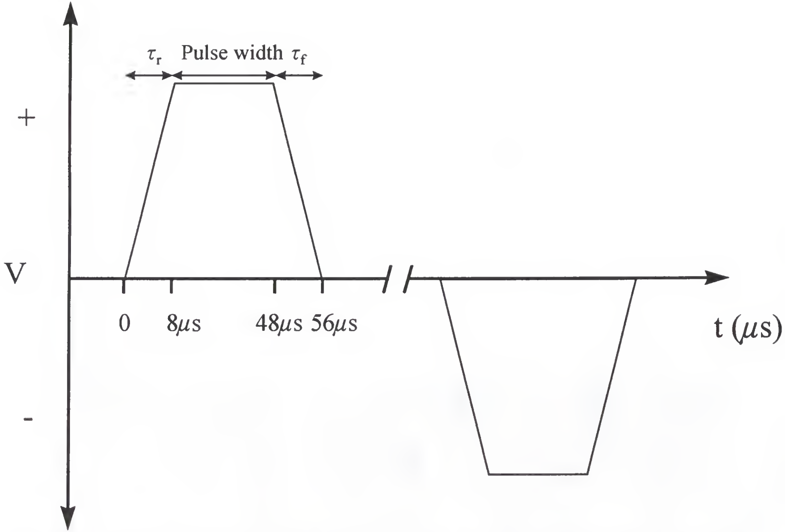

Figure 2-10. Diagram of a typical trapizoidal waveform for driving ACTFEL displays: where τ_r is the rise time, and τ_f is the fall time.

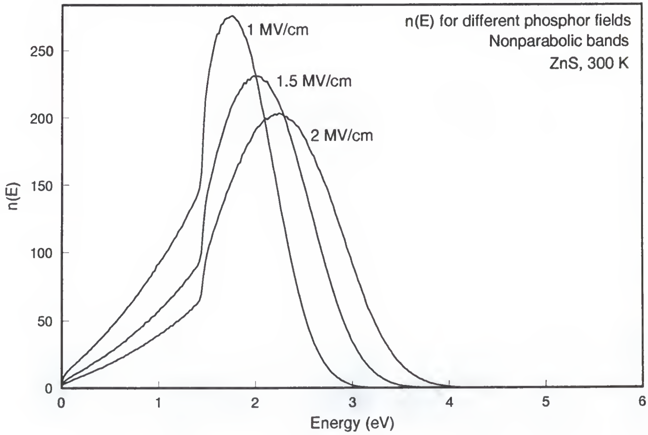

Figure 2-11. Nonparabolic band calculations of the electron energy distribution [n(E)] versus electron energy (E) for phosphor fields of 1.0, 1.5, and 2.0 MV/cm.

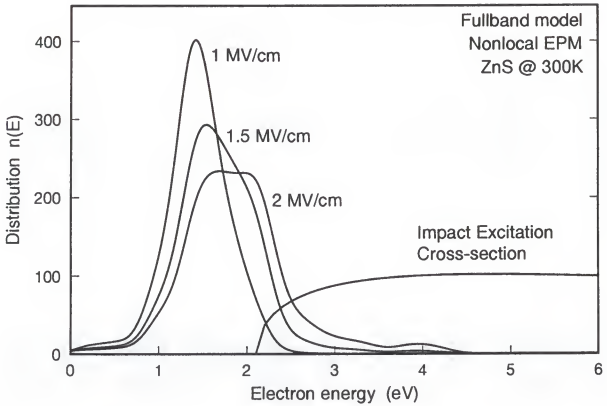

Figure 2-12. Full band calculations of the electron energy distribution [n(E)] versus electron energy (E) for phosphor fields of 1.0, 1.5, and 2.0 MV/cm. Mn excitation cross section also included in figure.

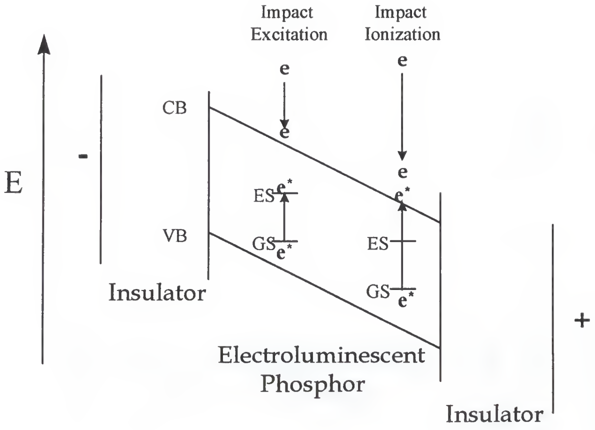

Figure 2-13. Illustration demonstrating the impact excitation and impact ionization mechnisms. CB and VB are the conduction and valence band, respectively, and GS and ES are the luminescent center ground state and excited state respectively.

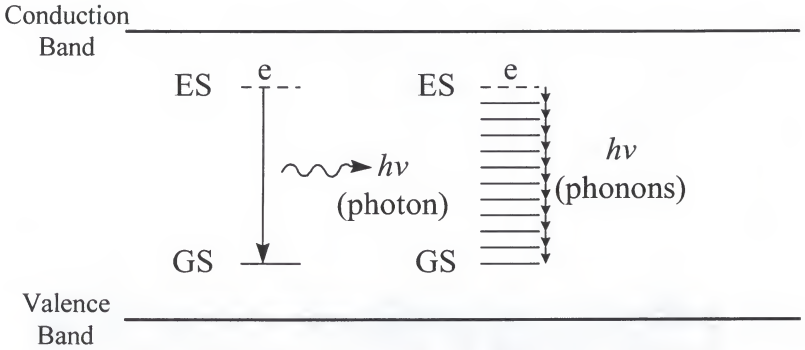

Figure 2-14. Schematic diagram of two de-excitation pathways, namely: 1) radiative recombination from the excited state which produces a photon, and non-radiative recombination which produces phonons.

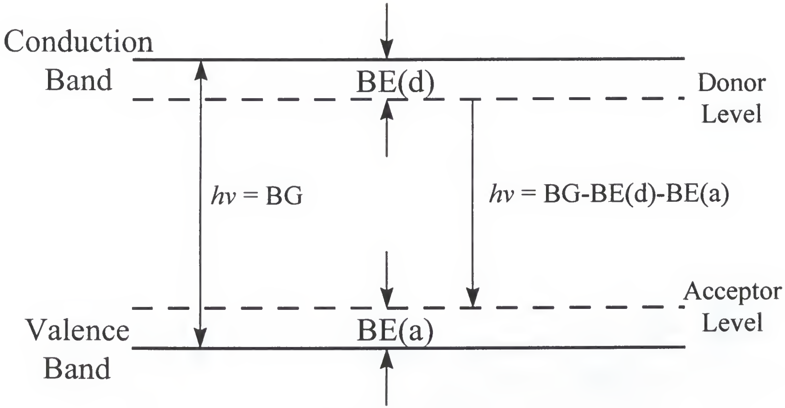

Figure 2-15. Energy band diagram of a typcial CRT phosphor radiative recombination process. BG is the semicodutor bandgap, BE(a) and BE(d) are the acceptor and donor binding energies, respectively, and hv is the photon energy.

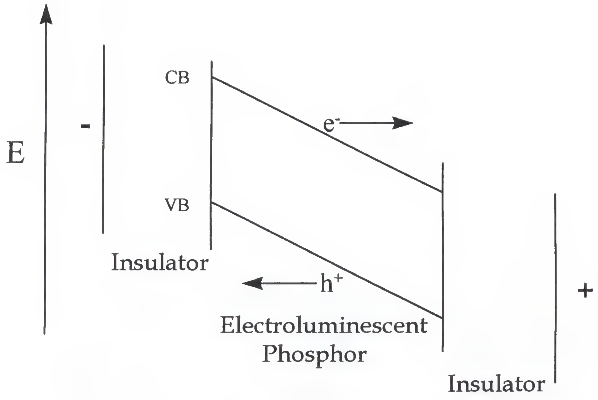

Figure 2-16. Schematic diagram of the separation of an electron and hole pair under bias. The electron travels toward the positive polarity, and the hole travels toward the negative polarity.

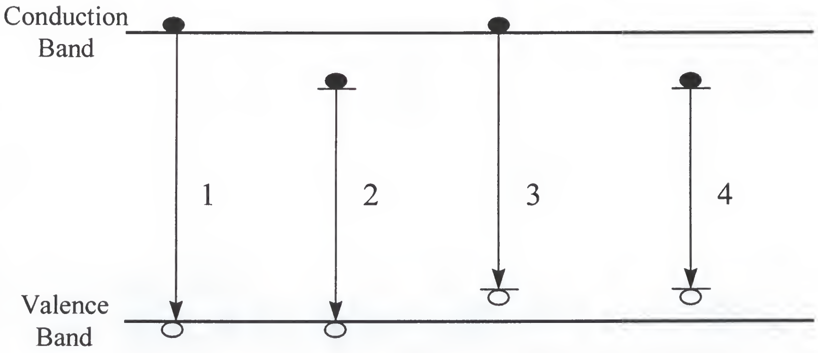

Figure 2-17. Schematic diagram of four electron-hole pair recombination mechanisms, namely: 1) band to band, 2) donor to valence band, 3) conduction band to acceptor, and 4) donor to acceptor recombination.

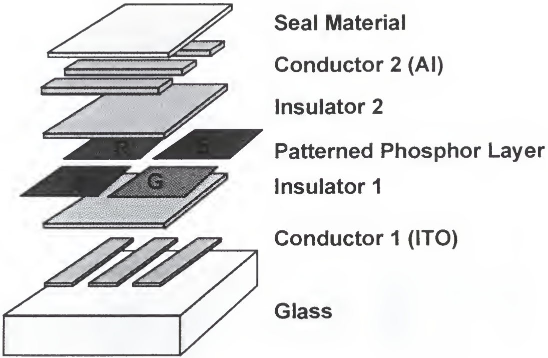

Figure 2-18. Standard full color ACTFEL device structure.

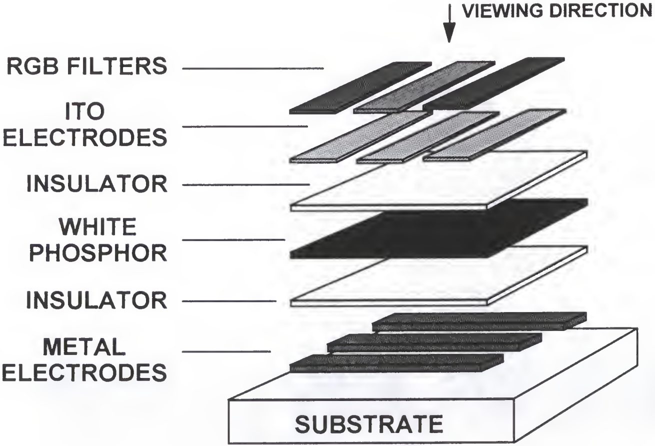

Figure 2-19. Inverted color by white full color ACTFEL device structure.

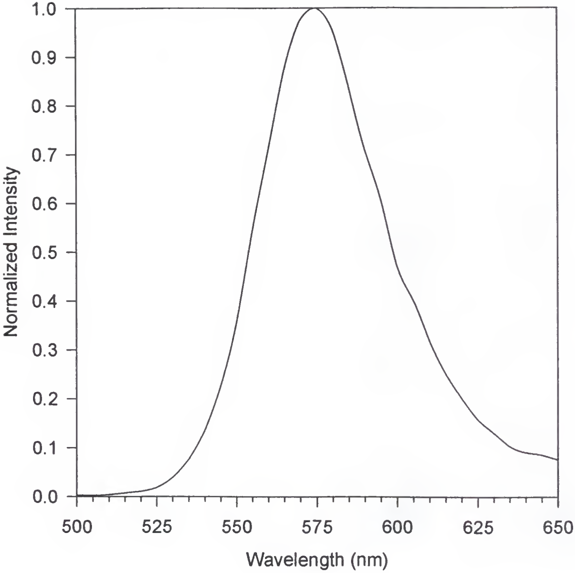

Figure 2-20. ZnS:Mn EL emission spectra.

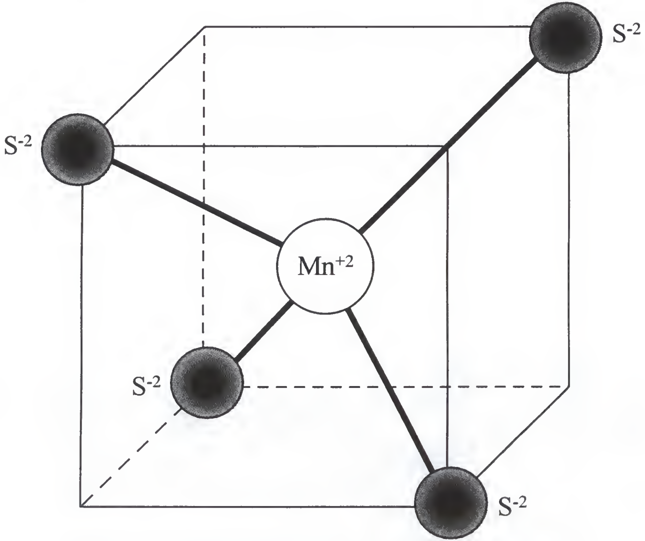

Figure 2-21. Tetrahedral symmetry of the Mn^{+2} luminescent center in ZnS.

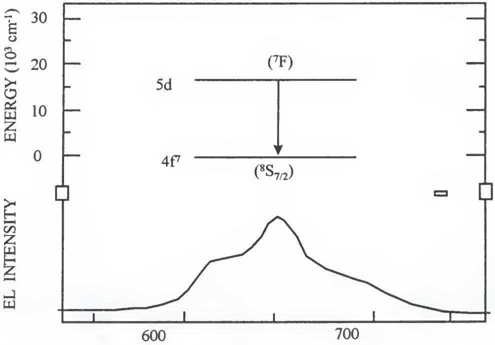

Figure 2-22. CaS:Eu EL emission spectrum.

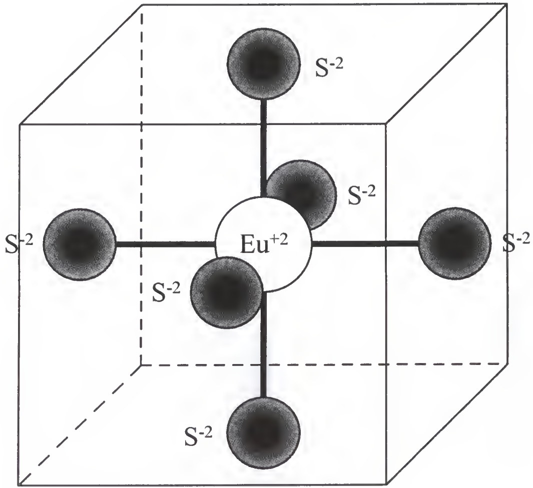

Figure 2-23. Octahedral symmetry of the Eu^{+2} luminescent center in CaS.

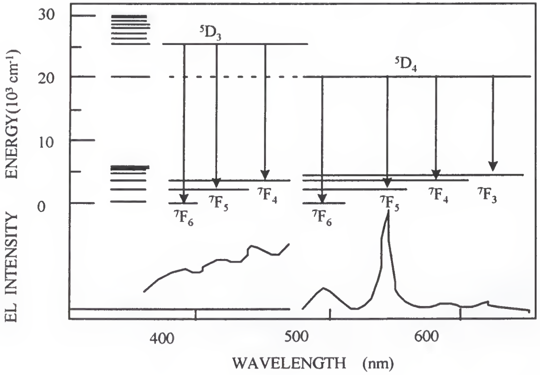

Figure 2-24. ZnS:Tb EL emission spectrum.

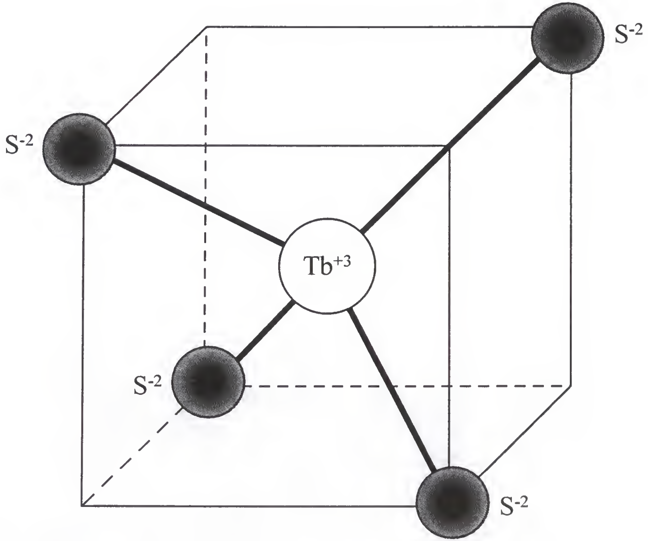

Figure 2-25. Tetrahedral symmetry of the Tb^{+3} luminescent center in ZnS.

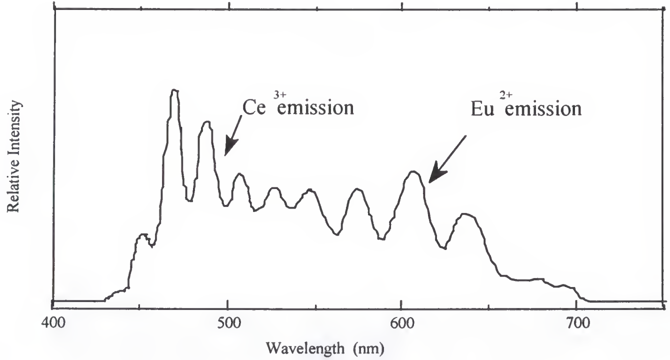

Figure 2-26. SrS:Ce,Eu EL emission spectrum.

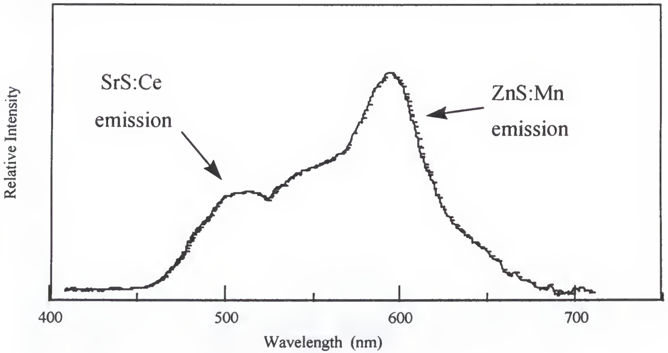

Figure 2-27. ZnS:Mn/SrS:Ce EL emission spectrum.

CHAPTER 3

THE EFFECTS OF OXYGEN DOPING $Ca_{0.55}Sr_{0.45}Ga_2S_4$:Ce THIN FILMS

Introduction

The work in the following chapter describes the effects that oxygen doping has on $Ca_{0.55}Sr_{0.45}Ga_2S_4$:Ce ACTFEL devices. In this work, x-ray photoelectron spectroscopy was used to elucidate the local chemistry of the Ce luminescent center in undoped and oxygen doped devices. A local change in the Ce chemistry was then correlated to the observed changes in the Ce^{+3} 4f-5d transition energy, and qualitatively explained using molecular orbital theory . Finally, molecular orbital calculations were performed on different Ce clusters to quantify the transition energy changes that were observed.

Background

In the $Ca_xSr_{1-x}Ga_2S_4$:Ce phosphor system, Ce^{+3} ions substitute for M^{+2} (where M is Ca or Sr) lattice sites ($Ce_{Ca\ or\ Sr}$). There is a close ionic radius match between Ce^{+3} and both Ca^{+2} and Sr^{+2} (see table 2-3 and 2-4) therfore larger concentrations of Ce can be introduced into the $Ca_xSr_{1-x}Ga_2S_4$ host matrix. Figure 3-1 shows the blue emission spectra of $Ca_xSr_{1-x}Ga_2S_4$:Ce (where x is 1 and 0) which results from $^2D(5d)$-$^7F_{5/2}(4f)$ and $^2D(5d)$-$^7F_{7/2}(4f)$ Ce^{+3} transitions, transitions. Because the Ce^{+3} transition is an intershell transition (5d-4f), there is an angular momentum difference between the ground state and the excited state ($\Delta l=1$), therefore this transition is allowed by the Laporte selection rule.

The $Ca_xSr_{1-x}Ga_2S_4$ host lattice has a rather complex orthorhombic crystal structure [PET 72a] which contains three slightly different M^{+2} lattice sites that have roughly a concentration ratio of 1:2:1. Recently, electron paramagnetic resonance (EPR) confirmed 3 different Ce^{+3} sites with a 1:2:1 concentration ratio in $Ca_xSr_{1-x}Ga_2S_4$:Ce phosphor powders which suggests that there was no preferrential Ce_M site in the lattice [WAR 96]. Though the three different M^{+2} sites differ slightly, the differences apparently do not profoundly impact the luminescent properties. Figure 3-2 shows the antiprismatic symmetry of the Ce_M sites and the relative positions of the 4f ground states and 5d excited states that are involved in the radiative transition.

The luminescent and structural properties of thiogallate powders [MGa_2S_4: M = Ca^{+2}, Sr^{+2}, Ba^{+2}, Pb^{+2}, Eu^{+2}, ($Na^{+1}La^{+3}$), and ($Na^{+1}Ce^{+3}$)] phosphors were first investigated in 1972 by Peters and Baglio [PET 72a, PET 72b]. They reported the crystal structures, as well as the photoluminescent (PL) and cathodoluminescent (CL) properties of thiogallate materials. After this initial report on the luminescence from thiogallates, few publications followed until Barrow, et al. in 1993 reported that MGa_2S_4:Ce (M = Ca, Sr, Ba) was an efficient blue EL phosphor [BAR 93]. Since this discovery, a lot of work has been devoted to optimizing and improving the blue EL phosphor performance. Barrow, et al. sputter deposited the MGa_2S_4:Ce phosphor which was amorphous as-deposited. Subsequent to the deposition, a heat treatment greater than 650C was performed to crystallize the phosphor. Peak wavelengths of 459nm, 445nm, and 452nm were reported for the Ca, Sr, and Ba thiogallates, respectively. The luminance of $CaGa_2S_4$:Ce was reported to be 10cd/m^2 (at 40 volts above threshold voltage measured at 60Hz).

Sun et al. [SUN 94] investigated the effects of varying the cerium concentration and the Sr/(Ca+Sr) ratio. They showed that the peak wavelength was linear with the Sr/(Ca+Sr) ratio (i.e., with an increased Ca concentration, the transition energy decreased), and that the emission spectra was relatively insensitive to the Ce concentration up to 8 mol. %. Because the anitprismatic symmetry is more complex than the tetrahedral or octahedral symmetry, the exact splitting of the Ce 5d orbitals in the $Ca_xSr_{1-x}Ga_2S_4$ is not fully understood. However, because the excited state is the lowest 5d orbital, one can still predict the effects of different alloying elements. For example, the gradual shift to lower energy as the Ca fraction approaches unity is easily explained by the point charge model of crystal field theory. As x approaches one, the lattice spacing becomes smaller which causes the Ce^{+3} 5d orbitals to experience a stronger crystal field. At stronger crystal fields, the low and high 5d energy orbitals are closer and farther, respectively from the ground state and the radiative transition between the lowest energy 5d orbital and the ground 4f levels decreases in energy as the lattice contracts.

One of the main drawbacks of this phosphor is that its complex crystal structure requires a high processsing temperature (>650C) to grow or convert to good crystalline material. These high processing temperatures are above the softening temperature of the standard Corning 7059 glass substrates, therefore a more expensive high-temperature glass ceramic substrate must be used. Consequently, much of the development of the thiogallates has focused on achieving better crystalline quality at lower processing temperatures. To reach these objectives, Inoue, et al. [INO 94] grew $CaGa_2S_4$:Ce by

MBE. They reported crystalline as-grown thiogallate at substrate temperatures between 400-600°C with a luminance up to 3cd/m^2 (at 80 volts above threshold voltage measured at 1kHz). Smith, et al. [SMI 95] developed an MOCVD technique and reported crystalline as-deposited $CaGa_2S_4$:Ce at substrate temperatures below 600°C with a luminance of 2cd/m^2 (L_{40} at 60Hz) and a peak wavelength of 459 nm. While MBE and MOCVD growth has resulted in crystalline thiogallate at lower temperatures, the luminescent properties are still inferior to sputter deposited annealed at temperatures > 650C.

Experimental Procedure

The thin film $Ca_{0.55}Sr_{0.45}Ga_2S_4$:Ce phosphors investigated in this study were prepared by rf magnetron sputtering from compacted powder targets supplied by David Sarnoff Research Center. The samples were doped by introducing gaseous O_2 along with argon as the backfilling gas in the sputter system. The gas flow rates were regulated with mass flow controllers, which varied the Ar/O_2 gas ratio and controlled the amount of oxygen doping in the films. The thiogallate thin films were amorphous as-deposited, and were annealed in an inert nitrogen atmosphere above 650°C to crystallize the thiogallate phosphor and to restore the luminescence. The complete device structure was a typical alternating current thin film electroluminescent (ACTFEL) structure: indium tin oxide (ITO) and aluminum were the two electrodes, aluminum oxide/titanium oxide (ATO) and barium tantalate (BTO) were the bottom and top insulators, respectively, and the $Ca_{0.55}Sr_{0.45}Ga_2S_4$:Ce (thiogallate) thin film was the semiconducting phosphor.

The XPS analysis was performed with a Perkin Elmer PHI 5100 ESCA system. The surface was sputtered with an argon ion beam at 1.5keV, 25mA emission, scanned over 1cm^2 area. The peaks were charge corrected by shifting the adventitious carbon peak to 284.6eV. A magnesium anode was used as the x-ray source with voltage and power settings of 14.5kV and 300W, respectively. XPS data were collected from samples without the top BTO insulator and aluminum electrode. The EL emission spectra were measured with a Pritchard spectrometer from complete device structures.

For comparison, the XPS spectra of a Ce foil was also measured. Ce is known to oxidize readily. The objective was to obtain XPS emission spectra from each of the two stable Ce oxides, CeO_2, and Ce_2O_3, to provide standard XPS spectra for both the +4 and +3 Ce oxidation state. XPS spectra were taken from the as recieved Ce foil and from the foil after sputter cleaning for 10 minutes. The data sets were collected a total of six times on the same area with a total sputter depth of approximately 60 nm (all sputter depths assumed a sputter rate of ~1 nm/min calibrated for Ta_2O_5).

Results

Effects of Oxygen Doping

When oxygen was introduced into the $Ca_{0.55}Sr_{0.45}Ga_2S_4$:Ce EL devices, it was found that the brightness and luminous efficiency increased, and the emission spectra shifted to a higher energy (blue shift). The device characteristics for undoped and oxygen doped $Ca_{0.55}Sr_{0.45}Ga_2S_4$:Ce EL devices are compared in table 3-1. Figure 3-3 shows the

EL emission spectra of the undoped and oxygen doped $Ca_{0.55}Sr_{0.45}Ga_2S_4$:Ce, and the shift in the peak emission wavelength from 460 to 445 nm is obvious.

XPS Analysis

The XPS survey scans (0-1000 eV, 0.5eV/step) of the undoped and oxygen doped $Ca_{0.55}Sr_{0.45}Ga_2S_4$:Ce films are shown in figures 3-4 and 3-5, respectively. To ensure that the XPS spectra were not convoluted with surface contaminants, the scans were taken after a 60 min Argon sputter which removed approximately 60nm of the $Ca_{0.55}Sr_{0.45}Ga_2S_4$:Ce thin film. To obtain specific information about the Ce bonding, higher resolution (0.1 eV/step) XPS scans were taken from 875-925 eV and 570-630 eV which contained the Ce core level $3d_{3/2}$ and $3d_{5/2}$ peaks and the Ce MNN Auger peak, respectively. Figures 3-6 and 3-7 show the charge corrected Ce $3d_{3/2}$ and $3d_{5/2}$ peaks and figures 3-8 and 3-9 show the Ce MNN Auger peak for the undoped and oxygen doped films, respectively .

From figures 3-6 and 3-7 , it is observed that the small shoulders (at ~ 882 and ~ 900 eV) on the low binding energy side of the ground state (GS) $3d_{3/2}$ and $3d_{5/2}$ peaks are larger for the oxygen doped sample versus the undoped sample. These shoulders are referred to as charge transfer (CT) peaks. The Ce MNN Auger peaks in figure 3-8 and 3-9 both have a low signal to noise ratio and are both fairly broad.

For the Ce foil that was analyzed with XPS, two spectra were of particular interest. Figure 3-10 shows the Ce 3d region for the foil after 10 minutes of sputtering (approximately 10nm). This spectra is representative of the Ce^{+4} oxidation state [WAG 79 p.134] which suggests a composition of CeO_2. Figure 3-11 is the XPS spectra of the Ce foil after it was sputtered a total of 60 minutes (60 nm). This figure is representative of the Ce^{+3} oxidation state [PAR 93, figure 2b] which suggests a composition of Ce_2O_3. To determine if the stoichiometries of each spectra were consistent with the apparent Ce oxidation state, the atomic compositions were calculated using the following expression [WAG 79 p.22]:

$$(3\text{-}1)\quad \frac{n_{Ce}}{n_O} = \frac{\left(I_{Ce}/S_{Ce}\right)}{\left(I\ \ /S\ \ \right)}$$

where n is the atomic concentration I_{Ce} and I_O are the areas under the Ce 3d peaks and the 0 1s peak, respectively, and S_{Ce} and S_O are the empirical sensitivity factors for Ce and O, respectively. The peak areas, sensitivity factors and atomic compositions from figures 3-8 and 3-9 are listed in table 3-2, and the compositions are consistent with the stoichiometries expected for CeO_2 and Ce_2O_3.

Discussion

Thermodynamic Considerations

To predict the cationic species (Ca, Sr, Ga, or Ce) with which the oxygen could form a bond in the thiogallate phosphor, the enthalpies of formation for the appropriate sulfide to oxide reactions were calculated based on the data from [LID 91]. The following reactions were considered:

$$(3\text{-}3)\ \ 2Ce_2S_3 + 4O_2 \rightarrow 4CeO_2 + 6S \qquad \Delta H = -117\ \text{kcal/mol}O_2,$$

$$(3\text{-}4)\ \ 2Ce_2S_3 + 3O_2 \rightarrow 2Ce_2O_3 + 6S \quad \Delta H = -97\ \text{kcal/mol}O_2,$$

$$(3\text{-}5)\ \ 2\ CaS + O_2 \rightarrow 2CaO + 2S \quad \Delta H = -72\ \text{kcal/mol}O_2,$$

$$(3\text{-}6)\ \ 2SrS + O_2 \rightarrow 2SrO + 2S \qquad \Delta H = -58\ \text{kcal/mol}O_2.$$

The thermodynamic data used for these calculations are listed in table 3-3. While this list of reactions is not exhaustive, it represents those most likely to occur. The subsequent sulfur reactions were not described because these sulfides commonly contain native sulfur vacancies due to the high vapor pressure of sulfur. Presumably, the sulfur byproduct would either fill some of these vacancies, or alternatively react with oxygen to form a volatile SO_x molecule. While no second phases of CeO_2 or Ce_2O_3 were detected by x-ray diffraction, the thermodynamic data imply that the Ce-O bond is the stronger than Ce-S bonds or Ca-O or Sr-O bonds. Therefore, Ce is the thermodynamically favored cation in the $Ca_{0.55}Sr_{0.45}Ga_2S_4$:Ce with which oxygen would bond.

XPS Analysis

To elucidate the local chemistry of the Ce luminescent center, the Ce 3d and MNN Auger peaks were evaluated for the undoped and oxygen doped $Ca_{0.55}Sr_{0.45}Ga_2S_4$:Ce devices. To determine if oxygen was preferentially bonding to Ce in these devices, Auger parameter calculations were attempted for doped and un-doped samples. The Auger parameter (a) is given by [WAG 79 p. 19]:

$$(3\text{-}2)\ \ a = KE_A - KE_P = BE_p - BE_A$$

where KE and BE are kinetic energy and binding energy, respectively, and subscripts A and P denonte Auger peaks and photoelectron peaks, respectively. When a cation (Ce) is bonded to a different anion (O or S) the change in the binding energy for core level electrons are not always detectable in XPS. Therefore, the difference between the photoelectron peak and the Auger peak is used because this difference cancels out any static charge corrections and usually amplifies chemical bond energy shifts. The Auger parameters calculated for the undoped and oxygen doped $Ca_{0.55}Sr_{0.45}Ga_2S_4$:Ce films were 282 and 285 eV, respectively. While the 3 eV energy difference in the Auger parameter suggested a difference in the local Ce bonding between the undoped and oxygen doped films, complicated electron interactions in the rare earth ions made it difficult to interpret this difference.

To further investigate the changes in the Ce chemistry for the undoped and oxygen doped films, the Ce 3d core level structures were compared. Because Ce has two oxidation states (+3 and +4), it was first important to understand the 3d XPS spectra for each. The reported 3d peak energies for the Ce^{+3} (Ce_2O_3) and Ce^{+4} (CeO_2) are listed in table 3-4 and table 3-5, respectively, along with the corresponding electron configuration that was ascribed to each peak [ROM 93]. These peak energies and the relative peak heights were in excellent agreement with the two spectra (Figure 3-10 and 3-11) taken from the Ce foil. Furthermore the atomic composition calculations were consistent with the stoichiometries for each oxide, therefore figure 3-10 and figure 3-11 were assumed to be CeO_2 and Ce_2O_3, respectively. While the two valence states can be easily distinguished when analyzed separately, when both valence states are present the XPS spectrum is convoluted with overlapping ground state and charge transfer peaks. The only Ce^{+3} or Ce^{+4} 3d peak that does not overlap with another is the Ce^{+4} GS peak located at approximately 917 eV.

To understand the charge transfer process and the interpretation of the Ce 3d XPS data, the fundamentals of XPS must be understood. During XPS the sample is irradiated with a beam of soft x-rays. These x-rays photo-eject core level electrons which have a characteristic binding energy. The kinetic energy of the photo-ejected electrons are energy analyzed and their energy is used to generate a plot of binding energy versus intensity. The binding energy (BE) is determined from the kinetic energy (KE) through the following equation:

$$(3\text{-}7)\quad KE = h\nu - BE - \phi_S$$

where $h\nu$ is the x-ray energy and ϕ_S is the spectrometer work function.

The Ce 3d region is complicated because the 3d level split due to spin-orbital coupling into the $3d_{3/2}$ and $3d_{5/2}$ levels which are separated by about 8 eV of energy. These two spin-orbital states are called the ground state peaks and for the Ce^{+3} they have binding energies of approximately 886 eV ($3d_{5/2}$) and 904 eV ($3d_{3/2}$), and for the Ce^{+4} they have binding energies of approximately 899 eV ($3d_{5/2}$) and 917 eV ($3d_{3/2}$). For the Ce^{+3} oxidation state (i.e. Ce_2O_3), these XPS peaks originate from an incident x-ray beam that photoejects a $Ce3d^{10}$ electron with a valence electron configuration of $Ce4f^1(5d6s)^0$ $O2p^6$ (nomenclature after [NOR 89, ROM 93]). When photoejection occurs, the resulting electron configuration is Ce $3d^9 4f^1(5d6s)^0$ $O2p^6$. The resultant core hole in the Ce may induce a coulombic attraction for electrons which causes the ligand (i.e., oxygen) to donate one of its valence electrons to the Ce metal. This ligand-to-metal transfer process results in a valence electron configuration of $Ce4f^2(5d6s)^0$ and $O2p^5$. This re-arrangement in the electron configuration slightly changes the binding energy of the $3d_{3/2}$ and $3d_{5/2}$ core levels which results in a charge transfer (CT) XPS peak (located at ~ 882 and 900 eV for the $3d_{5/2}$ and $3d_{3/2}$ peaks, respectively). A similar process occurs for the Ce^{+4} oxidation state (i.e. CeO_2) however, two ligand-to-metal charge transfer states are possible because the Ce^{+4} core hole has a larger coulombic attraction than the Ce^{+3}. The ground state and the two charge transfer states of Ce^{+4} have electron configurations of $Ce4f^0(5d6s)^0$ $O2p^6$, $Ce4f^1(5d6s)^0$ $O2p^5$, and $Ce4f^2(5d6s)^0$ $O2p^4$, respectively (see table 3-5 for corresponding energy positions).

Empirical data and model calculations of the cerium tri-halides (Ceh_3 where h is F, Cl, and I) have shown that the ratio of the Ce 3d ground state peaks and their corresponding charge transfer peaks changed as a function of the ligand covalency [SCH 85, PAR 93]. In particular, as the ligand became more covalent, the relative intensity of the charge transfer peak decreases relative to the ground state peak. The CT peak heights change because as the Ce bond becomes more covalent, the electron cloud density near the Ce^{+3} bond becomes larger which screens the electron transfer process.

When comparing the Ce^{+3} peaks for the un-doped and oxygen-doped samples, the small shoulders (at 900.2eV and 881.7eV) on the low binding energy side of the $3d_{3/2}$ and $3d_{5/2}$ peaks increased in intensity when the films were oxygen doped (see figure 3-5 and 3-6). While initially these changes were attributed to a change in the Ce oxidation state (+3 to +4), the Ce^{+4} $3d_{3/2}$ ground state peak located at ~917 eV was not present (compare figures 3-5 and 3-6 to 3-10 and 3-11). This indicated that there was not a change in the Ce oxidation state, but rather there was a change in the local Ce bonding. The location of these shoulders, at ~ 882 and 900 eV, correspond with the Ce^{+3} $3d_{3/2}$ and $3d_{5/2}(5d6s)^0\,4f^2\,3d^9\,O(S)2p^5(3p^5)$ charge transfer peaks, therefore the parameters that affect the charge transfer process were investigated.

The arguments from the Ce-trihalide reports were used to understand the observation that the intensity of the CT peak increased relative to the GS peak for the oxygen doped $Ca_{0.55}Sr_{0.45}Ga_2S_4$:Ce thin films. The relative increase in the CT peaks for the oxygen doped $Ca_{0.55}Sr_{0.45}Ga_2S_4$:Ce thin films suggested that there was a local change in the Ce bonding. In particular, it suggested that the local ionicity of the Ce^{+3} increased which made the ligand-to-metal charge transfer process more likely to occur. This is consistent with oxygen ions replacing sulfur ions bonded to Ce.

To estimate the ionicity of the Ce bond in the oxygen doped $Ca_{0.55}Sr_{0.45}Ga_2S_4$:Ce films, the CT/GS peak height ratio of the Ce $3d_{5/2}$ peaks were plotted as a function of the bond ionicity based on the Ce tri-halide literature data and the measured Ce_2O_3 spectrum (Figure 3-11). In addition, the un-doped $Ca_{0.55}Sr_{0.45}Ga_2S_4$:Ce film was assumed to be domintated by Ce-S bonds so the CT/GS ratio in figure 3-6 was used to represent Ce^{+3}-S bonds. The fraction of covalency, f_c, is expressed by [ASK 94 p.32]:

$$(3\text{-}8) \quad f_c = \exp[(-0.25)\Delta EN^2]$$

where ΔEN is difference in the anion and cation electronegativities. Furthermore, the fraction of ionicity, f_i, is simply:

$$(3\text{-}9) \quad f_i = 1 - f_c.$$

Table 3-6 lists the cation and anion electronegativities used to generate the ionicity versus CT/GS peak ratio plot in figure 3-12.

The plot of ionicity versus CT/GS peak ratio was found to fit well with a linear regression. This empirical plot was used to quantitatively estimate the local stoichiometry of the Ce. The CT/GS peak height ratio for the oxygen doped $Ca_{0.55}Sr_{0.45}Ga_2S_4$:Ce thin films from figure 3-7 was approximately 0.4. From figure 3-12 this correlated to an ionicity and an average anion electrongativity of 0.57 and 2.9, respectively. Because there are eight Ce ligands in the $Ca_{0.55}Sr_{0.45}Ga_2S_4$ lattice, approximately three oxygen and five sulfur ligands would yield an average electronegativity of 2.9. Thus, while the undoped films consisted of Ce centers bonded to eight sulfur ions, the oxygen doped films consisted of Ce centers bonded to three oxygen ions and five sulfur ions.

Another more subtle observation from the XPS spectra showed that the difference between the Ce $3d_{5/2}$ GS and CT state peak slightly decreased when the $Ca_{0.55}Sr_{0.45}Ga_2S_4$:Ce films were oxygen doped (4.4 versus 3.8 eV for undoped and oxygen-doped samples, respectively). This trend agreed with Gunnarsson-Schonhammer calculations performed for Ce-trihalides which showed that the binding energy of the charge transfer state (BE_{CT}) is proportional to Q - Δ; where Q is the ionized Ce core hole attraction energy, and Δ is the difference between the Ce 4f binding energy and the ligand (i.e. O or S) valence electron binding energy [PAR 93]. It can be shown that Δ increased when the Ce ligand changed from S to O because the binding energy of the O 2p valence electrons was larger than the S 3p valence electrons. The Ce core hole attraction energy,Q, also increased, although to a lesser degree than Δ, when S was replaced by O because of the core hole screening phenomenon described earlier. The net effect is that Q - Δ decreased as S was replaced by O, therefore the energy separation between the Ce 3d GS and CT peaks became smaller.

Together the thermodynamic considerations and the XPS results suggest oxygen was ligating to the Ce luminescent center in the oxygen doped $Ca_{0.55}Sr_{0.45}Ga_2S_4$:Ce films.

Effects of Oxygen Doping on the Luminescent Transitions

Figure 3-3 shows the emission spectra for both an undoped and an oxygen-doped sample. A blue spectral shift of 15nm (733cm^{-1}) was observed when oxygen was introduced into the $Ca_{0.55}Sr_{0.45}Ga_2S_4$:Ce films. The emission spectra shows two peaks separated by about 45nm (2063cm^{-1}) which is due to the spin-orbital splitting of the 4f level into $4f_{7/2}$ and $4f_{5/2}$ states. Vercaemst et al. [VER 93]] suggested that the energy separation of the 4f-5d transition should increase as the Ce valence state was changed from the (+3) to (+4), which was in agreement with calculations perfromed by Liberman et al. [LIB 71]. However, a change in valence state from (+3) to (+4) is not a plausible explanation for the observed spectral blue shift, because the (+4) state of Ce results from transferring two 6s electrons and two 4f valence electrons to the anion which leaves the 4f orbital empty. Thus, the 4f-5d transition is not probable because of lack of excitation (empty 4f level). Instead, the spectral shift is apparently due to the sensitivity of the 4f-5d transition to the properties of the host lattice.

While atomic transitions are localized radiative events that occur between atomic states associated with the luminescent center, they are influenced by the host lattice material. The degree to which they are influenced depends primarily on the position of the electronic states that are involved in the transition. When a transition metal or rare earth ion exists in space (i.e., immune to any electric or magnetic field), the electrons arrange themselves in a way that minimizes the total energy of the ion. This free ion arrangement is perturbed however, in the presence of an electric or magnetic field. The degree to which the atomic states are perturbed depends largely on where the states are located with regards to the nucleus. Core level electrons are bound tightly to the nucleus and are shielded by outer electrons which essentially nullify the influence of external fields. Outer shell electrons however, are not bound as tightly to the nucleus and are not shielded; subsequently external fields can have a significant effect on their energy levels.

When free ions are bound together to form a solid, their outer energy levels change significantly because of the influence of nearby ions. In a perfectly ionic solid, cations and anions behave like positive and negative point charges, respectively. Atomic energy levels are modified because coulombic forces exist between the oppositely charged ion. The coulombic forces induce a crystal field in the solid which is a function of the ion arrangement (symmetry), the ion spacing, and the valence or charge of the ions in the solid. While the crystal field model accurately describes a perfectly ionic material, in practice all solids deviate from purely ionic behavior. This arises because nearest neighbor electron clouds overlap with one another and mix to form a partially covalent bond. In addition to the crystal field, the atomic energy level positions are also a function of the covalency/ionicity of the ion-ligand bond. The ion-ligand electron cloud interactions are a function of the symmetry of the lattice, the shape and symmetry of the orbitals of interest, and finally the relative energy positions of the ion and ligand outer shell electrons [ZUM 89 p.924]. Consequently, one must consider the lattice symmetry, the ion spacing, and the properties of the cations and anions to understand the electron energy levels of the luminescent center.

In the undoped versus the oxygen doped $Ca_{0.55}Sr_{0.45}Ga_2S_4$:Ce samples, neither the lattice spacing nor the geometry of the Ce was believed to change significantly. Though the lattice presumably contracted locally to accomodate the smaller oxygen ions, a local contraction should red shift the emission which was contrary to the observations. Oxygen was assumed to simply substitute isoelectronically for sulfur since they have the same valence state (-2), therefore the blue shift in the emission spectra must have resulted from a change in the molecular orbital overlap between Ce and its nearest neighbors. While symmetry and ion spacing will be considered in the chapter 4, this discussion will focus on the effects of the cation and anion molecular orbital overlap. For the Ce transitions that are of interest, only the 5d orbitals will be considered because they are affected by host lattice while the 4f orbitals are shielded.

The degree to which the molecular orbitals overlap in a solid depends on the properties of the cations and anions. One measure of the degree of overlap is the type of bonding (ionic vs. covalent) that dominates in the material: if the bonding is primarly ionic then the MO overlap is small, and if the bonding is primarily covalent then the MO overlap is large [DUF 90 p.103]. Equation 3-8 demonstrates that the bonding between two ions is a function of how strong each ion binds its outer electrons. For elemental semiconductors (i.e., Si and Ge) where ΔEN is zero, these solids are characterized as having perfectly covalent bonds, and valence electrons are shared between neighboring atoms. When the ΔEN increases for III-V and II-VI materials, their bonding becomes more ionic because the anion has a stronger attraction for electrons versus the cation.

In the free ion state, there are obviously no MO interactions and if spin-orbital interactions are ignored, all the d-orbitals are degenerate with respect to energy (i.e., all have the same energy). However, when these orbitals interact with nearest neighbor anions, the d-orbitals hybridize due to electron cloud interactions. This effect is called the nephelauxetic effect, which literally translated means (electron) cloud expanding [BLA 94 p.16]. When a transition metal or rare earth ion is surrounded by a host matrix, the normal electron orbital distributions are perturbed and new energy states are produced. The orbital interactions create lower energy bonding states and higher energy antibonding states through hybridization. As the molecular orbital overlap increases for more covalent solids, the energy position of both the bonding states and antibonding states shift to lower energy. While the bonding states and antibonding states may shift by different amounts, if the details of the ground state and the excited state are known, one can predict how different host materials (more ionic or more covalent) will change the radiative transition energy of a luminescent center.

To model the effect that oxygen ligands would have on the Ce 4f-5d radiative transitions, semiempirical cluster calculations were performed. The details of the semiempirical calculations will be discussed in chapter 4, however a brief descrption of the cluster geometry used to model the effects of the oxygen doping will be presented here. To make the cluster calculations tractable, a SrS host lattice (sodium chloride) was assumed rather than the complex orthorhombic crystal structure of the $Ca_{0.55}Sr_{0.45}Ga_2S_4$. This was a reasonable assumption, because the change in the radiative transition energy was of interest, rather than the absolute transition energy.

Graphically, the Ce^{+3} luminescent center was placed at the origin and six octahedral S(-2) ligands were placed at $a_o/2$ (.301 nm) along each of the positive and negative directions of the three Cartesian axes. Next, six Sr ligands were placed at a_o (.602 nm) along the three Cartesian axes. This thirteen ion cluster was then surrounded by a 15x15x15 matrix of +2 and -2 point charges to account for the electrostatic contribution of the rest of the host lattice (figure 3-13). After calculating the 4f and 5d energy postitions on this cluster, new clusters with one, two, and three S(-2) ligands replaced by O(-2) ligands were constructed, respectively. The calculated 4f and 5d energy levels for the four clusters are listed in table 3-7.

Because the experimental Ce (+3) emission bands are convolutions of electronic and vibronic transitions [YAM 87], to compare calculated results with the experimental data, it was convenient to use the centroids of each spin-orbital level to estimate the average position of each energy level. Table 3-8 lists the centroids of each 4f and 5d spin-orbital levels of the Ce (+3), and table 3-9 lists the the difference betewen the $5d_{3/2}$-$4f_{5/2}$ and $5d_{3/2}$-$4f_{7/2}$ transitions for each of the cluster. From table 3-8 it was clear that the change in the radiative transition energy was dominated by the change in the 5d levels versus the 4f levels. This was expected because the 5d orbitals are much more sensitive to the local environment. From table 3-9, it was observed that the $5d_{3/2}$-$4f_{5/2}$ radiative transition energy increased (blue shifts) 510.5, 1147.6, and 2606.8 cm^{-1} when 1, 2, and 3 oxygens were ligated to the Ce(+3) luminescent center, respectively.

From the XPS results, it was estimated that three oxygen ions sit substitutionally for sulfur sites which results in a O/S ratio of 3/5 (0.6). This correlated with a 733cm^{-1} increase in the $5d_{3/2}$-$4f_{5/2}$ transition energy. For the cluster calculations using the SrS lattice, the closest O/S ratio was 2/4 (0.5), which corellated to an increase in the $5d_{3/2}$-$4f_{5/2}$ transition energy of 1147.6cm^{-1}. The model calculations and experimental results were in reasonable agreement with each other which further confirmed the idea that oxygen replaced sulfur ligands in the oxygen doped $Ca_xSr_{1-x}Ga_2S_4$:Ce devices.

Summary

The effects of oxygen doping of $Ca_{0.55}Sr_{0.45}Ga_2S_4$:Ce blue electroluminescent (EL) phosphor were investigated by EL emission spectra, XPS, and model calculations of hte nephalauxetic effect. Oxygen doping resulted in a 15nm (733cm^{-1}) blue shift in the EL emission spectra. Thermodynamic data showed that the formation of Ce-O bonds were thermodynamically favored over Ce-S and Sr-O or Ca-O bonds, and changes in the Ce 3d XPS peaks indicated that oxygen was ligating to Ce. Blue emission from the thiogallate phosphor was shown to result from the Ce(+3) 5d-4f radiative transitions. Based on the electronegativity difference between oxygen (3.5) and sulfur (2.5), oxygen bonded to Ce should locally increase the ionicity of the Ce luminescent center. The nephelauxetic effect predicts that as Ce bonding becomes more ionic, the electrons are bound stronger to the electronegative anion, which increases the energy of the 5d(T_{2g}) energy level. The increase in the 5d(T_{2g}) energy level was correlated with the observed increase in the radiative transition energy of the 5d-4f radiative transition.

Semiempirical cluster calculations of Ce ligated to S and O revealed a systematic increase in the radiative transition energy as sulfur ligands were replaced by oxygen ligands. Quantitatively, an oxygen to sulfur ratio of 0.5 increased the 5d-4f radiative transition 1147.6cm^{-1}. This was in excellent agreement with the estimated oxygen to sulfur ratio 0.6 in the oxygen doped $Ca_{0.55}Sr_{0.45}Ga_2S_4$:Ce devices which increased 733cm^{-1}.

Table 3-1. Device Properties for Undoped and Oxygen Doped $Ca_{0.55}Sr_{.045}Ga_2S_4:Ce$

$Ca_{0.55}Sr_{.045}Ga_2S_4:Ce$	**L_{40} (60 Hz)**	**Efficiency (lum/W)**	**CIE x**	**CIE y**
undoped	2.5	0.017	0.14	0.17
oxygen doped	4.3	0.03	0.15	0.14

Table 3-2. Parameters for Ce-oxide XPS Atomic Composition Calculations

Figure (Ce-oxide)	**XPS Peak**	**Area (cts-eV/s) (I)**	**Sensitivity Factor (S)**	**Atomic Concentration (n) (%)**
3-10 (CeO_2)	Ce 3d	448,148	10	29.55
	O 1s	70,521	0.66	70.45
3-11 (Ce_2O_3)	Ce 3d	1,100,365	10	41.56
	O 1s	102,113	0.66	58.44

Table 3-3. Thermodynamic Data [LID 91]

Compound/Element	ΔH_f (kcal/mol)
Ce_2S_3	-284
CeO_2	-259
Ce_2O_3	-429
$Ce_2(SO_4)_3$	-945
CaS	-115
CaO	-151
SrS	-112
SrO	-141
O_2	0
S	0

Table 3-4. Reported Ce^{+3} 3d XPS Binding Energies [ROM 93]

Ce^{+3} Peak	3d$_{5/2}$ 4f^2(5d6s)^0 O2p^5	3d$_{5/2}$ 4f^1(5d6s)^0 O2p^6	3d$_{3/2}$ 4f^2(5d6s)^0 O2p^5	3d$_{3/2}$ 4f^1(5d6s)^0 O2p^6
Binding Energy (eV)	881.3	885.5	898.9	903.8

Table 3-5. Reported Ce^{+4} 3d XPS Binding Energies [ROM 93]

Ce^{+4} Peak	3d$_{5/2}$ 4f^2(5d6s)^0 O2p^4	3d$_{5/2}$ 4f^1(5d6s)^0 O2p^5	3d$_{5/2}$ 4f^0(5d6s)^0 O2p^6	3d $_{3/2}$ 4f^2(5d6s)^0 O2p^4	3d$_{3/2}$ 4f^1(5d6s)^0 O2p^5	3d$_{3/2}$ 4f^0 (5d6s)^0 O2p^6
Binding Energy (eV)	882.5	888.6	898.5	900.8	906.9	916.7 eV

Table 3-6. Electronegativity Values for Selected Atoms

Ce	F	O	Cl	S
1.1	4	3.5	3	2.5

Table 3-7. Calculated Ce 4f and 5d Energy Levels (cm^{-1})

Ce (+3) Energy Level	**6 S(-2), 0 O(-2)**	**5 S(-2), 1 O(-2)**	**4 S(-2), 2 O(-2)**	**3 S(-2), 3 O(-2)**
5d$_{5/2}$ (T$_{2g}$)	28,742.6	30,327.6	31,820.5	31,310.9
5d$_{3/2}$ (T$_{2g}$)		29,614.4	29,197.1	30,416.7
5d$_{3/2}$ (T$_{2g}$)	27,666.6	26,907.4	28,587.8	30,327.9
4f$_{7/2}$		2,604.1	2,633.1	2,588.2
4f$_{7/2}$	2,399.4	2,465.6	2,438.4	2,459.6
4f$_{7/2}$	2,357	2,360.7	2,352.8	2,451.8
4f$_{7/2}$	2,334.8	2,325.8	2,314.8	2,321.6
4f$_{5/2}$		248.9	267.3	193.9
4f$_{5/2}$	50	77.6	42.7	177.9
4f$_{5/2}$	0	0	0	0

Table 3-8. Centroids of the Calculated Ce 4f and 5d Spin Orbital Levels (cm^{-1})

Ce (+3) Energy Level	**6 S(-2), 0 O(-2)**	**5 S(-2), 1 O(-2)**	**4 S(-2), 2 O(-2)**	**3 S(-2), 3 O(-2)**
$5d_{5/2}$	28,742.6	30,327.6	31,820.5	31,310.9
$5d_{3/2}$	27,666.6	28,260.9	28,892.5	30,372.3
$4f_{7/2}$	2,363.7	2,439.1	2,434.8	2,455.3
$4f_{5/2}$	25	108.8	103.3	123.9

Table 3-9. Calculated Ce 5d-4f Transition Energies (cm^{-1})

Ce (+3) Radiative Transition	**6 S(-2), 0 O(-2)**	**5 S(-2), 1 O(-2)**	**4 S(-2), 2 O(-2)**	**3 S(-2), 3 O(-2)**
$5d_{3/2}$-$4f_{7/2}$	25,302.9	25,821.8	26,457.7	27,917
$5d_{3/2}$-$4f_{5/2}$	27,641.6	28,152.1	28,789.2	30,248.4

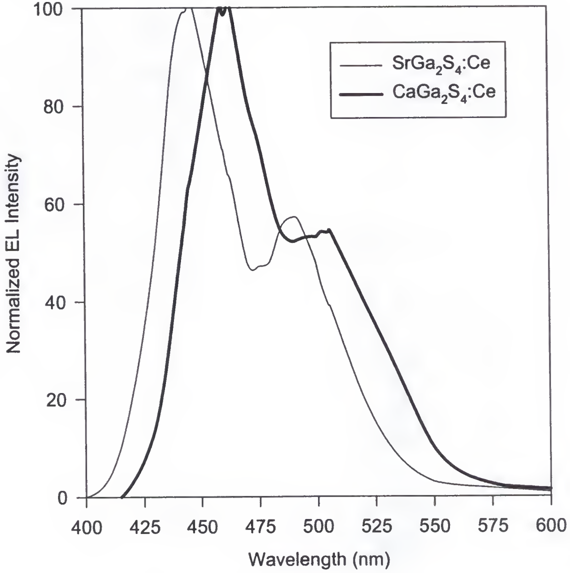

Figure 3-1. $CaGa_2S_4$:Ce and $SrGa_2S_4$:Ce EL emission spectra.

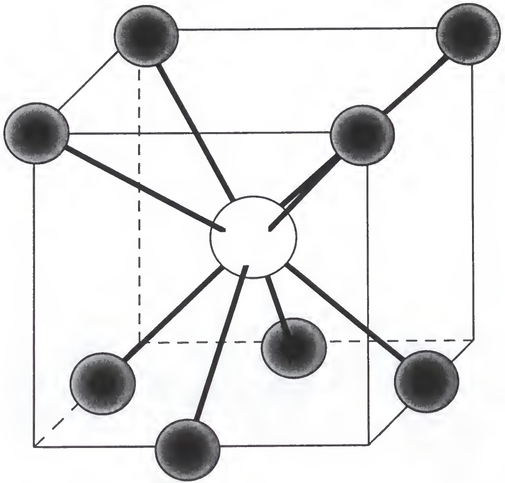

Figure 3-2. Schematic of the antiprismatic symmetry of the Ce^{+3} ion in the thiogallate host latice.

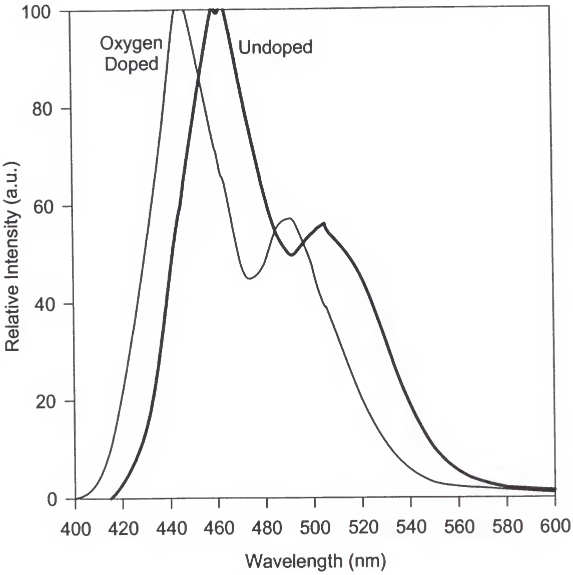

Figure 3-3. Undoped and oxygen doped $Ca_{0.55}Sr_{0.45}Ga_2S_4$:Ce EL emission spectra.

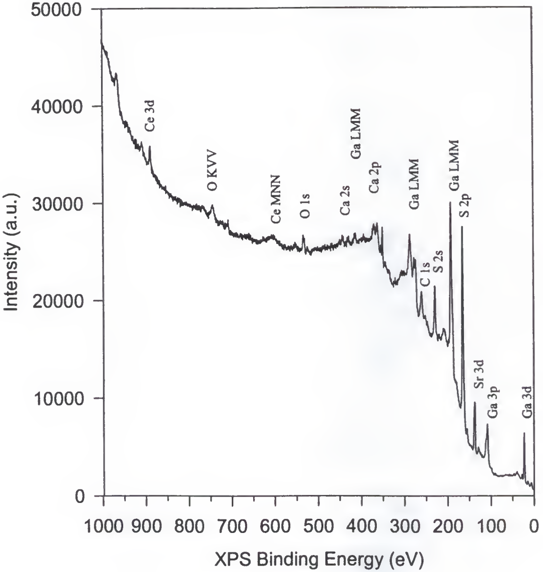

Figure 3-4. XPS survey scan of undoped $Ca_{0.55}Sr_{0.45}Ga_2S_4$:Ce.

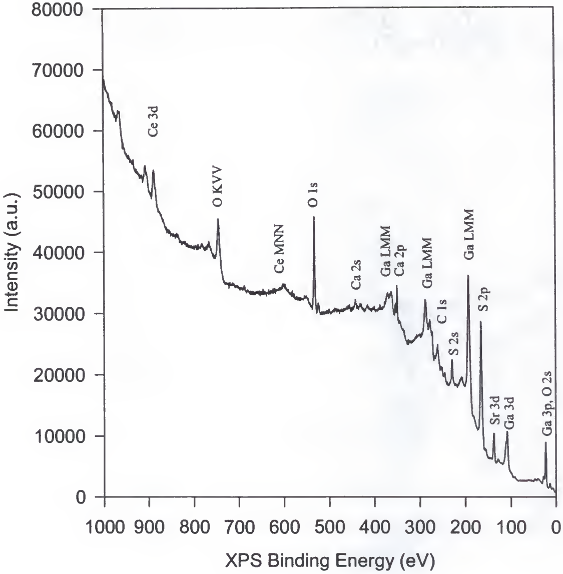

Figure 3-5. XPS survey scan of oxygen doped $Ca_{0.55}Sr_{0.45}Ga_2S_4$:Ce.

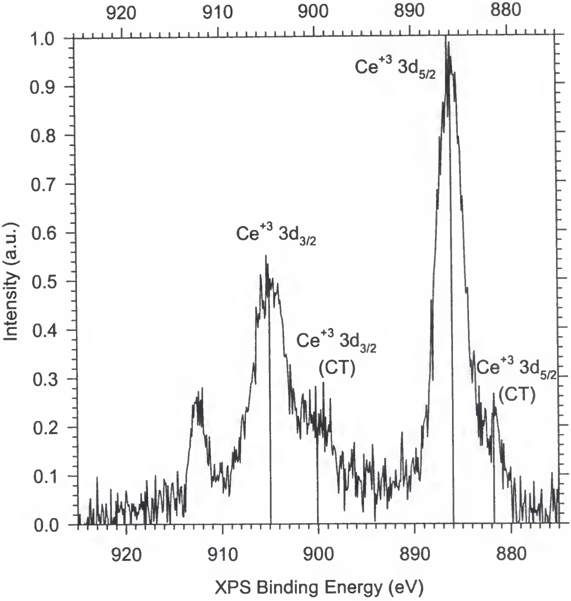

Figure 3-6. Ce 3d XPS spectra of undoped $Ca_{0.55}Sr_{0.45}Ga_2S_4$:Ce.

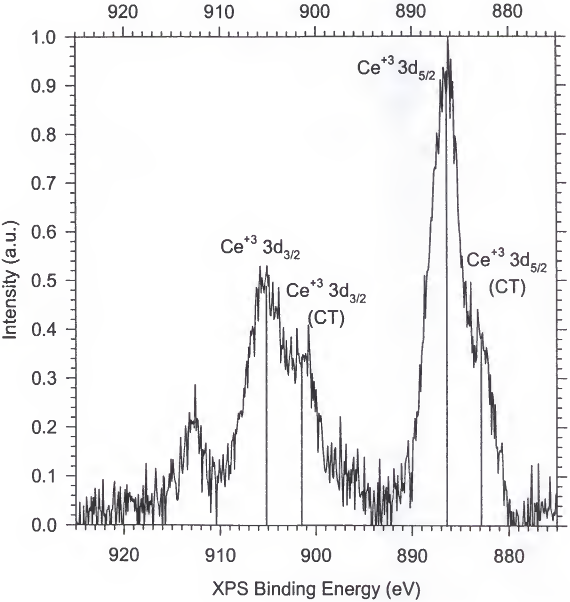

Figure 3-7. Ce 3d XPS spectra of oxygen doped $Ca_{0.55}Sr_{0.45}Ga_2S_4$:Ce.

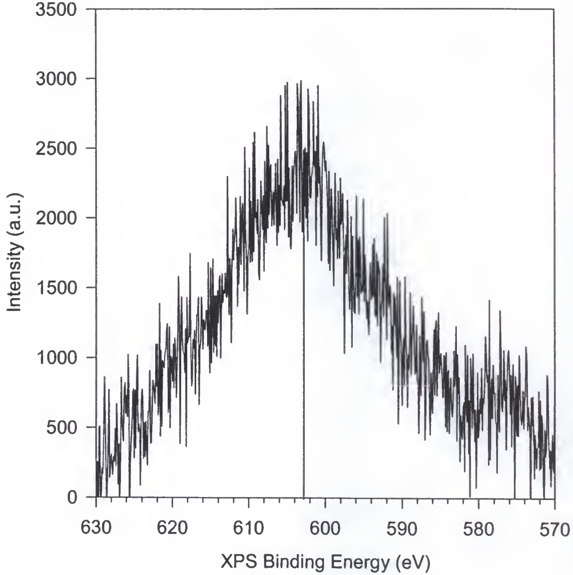

Figure 3-8. Ce MNN Auger XPS spectra of the undoped $Ca_{0.55}Sr_{0.45}Ga_2S_4$:Ce.

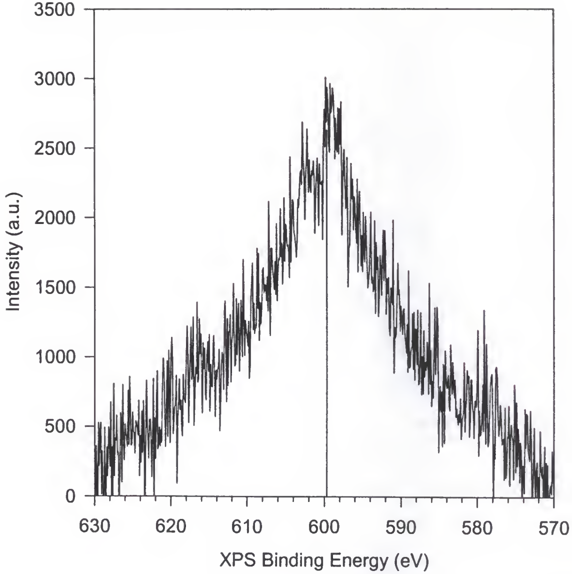

Figure 3-9. Ce MNN Auger XPS spectra of the oxygen doped $Ca_{0.55}Sr_{0.45}Ga_2S_4$:Ce.

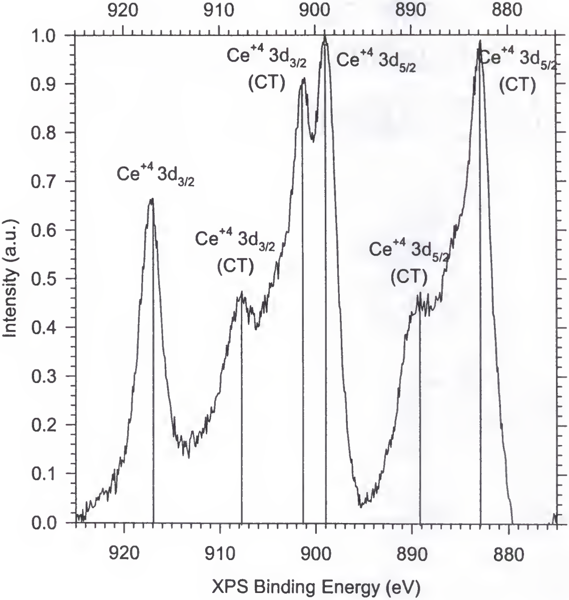

Figure 3-10. Ce 3d XPS spectra of a Ce foil after a 10 minute sputter clean. The spectra suggests that the CeO_2 oxide dominates.

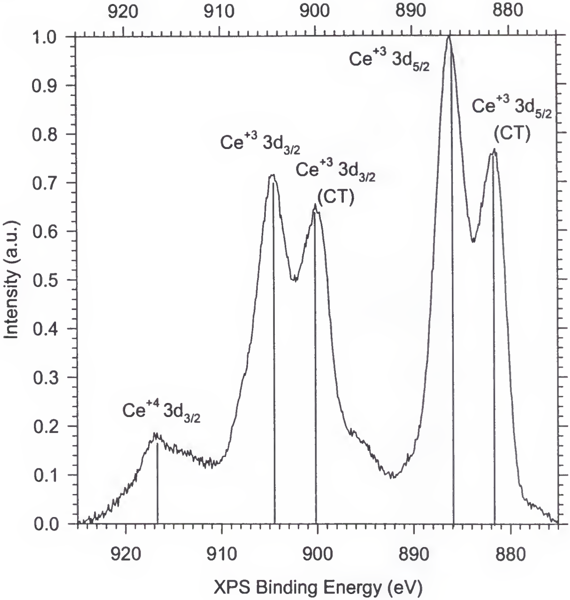

Figure 3-11. Ce 3d XPS spectra of a Ce foil after a 60 minute sputter clean. The spectra suggests that the Ce_2O_3 oxide dominates.

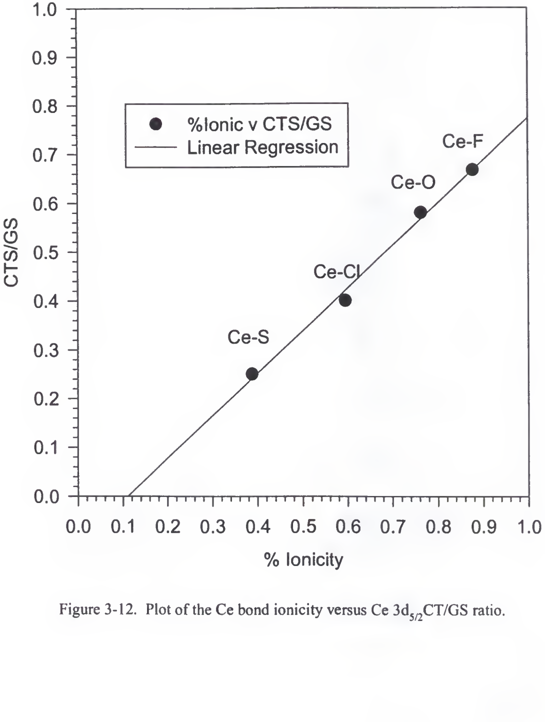

Figure 3-12. Plot of the Ce bond ionicity versus Ce $3d_{5/2}$CT/GS ratio.

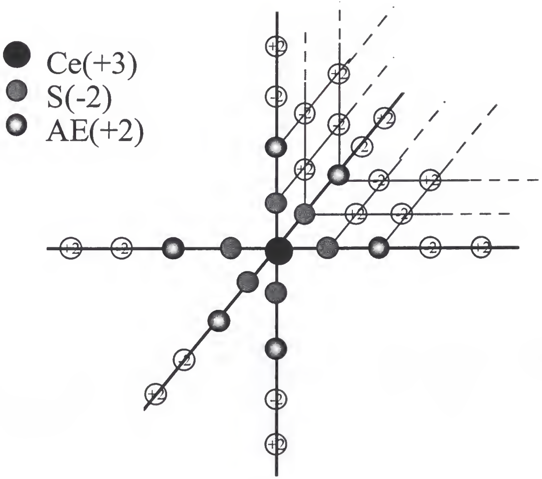

Figure 3-13. Illustration showing the ion and point charge positions for the semiempirical molecular orbital cluster calculations.

CHAPTER 4

EMISSION SPECTRA CHANGES IN Ce DOPED ALKALINE EARTH (Mg, Ca, Sr, AND Ba) SULFIDE PHOSPHORS

Inroduction

The following chapter describes the effects that different alkaline earth (AE) sulfide host materials have on the Ce^{+3} emission process. In this work, both semiempirical molecular orbital cluster calculations and crystal field calculations were performed on MgS:Ce, CaS:Ce and SrS:Ce, respectively. The calculated Ce^{+3} transition energies were compared with literature data and then crystal field calculations were performed on BaS:Ce. $Sr_xBa_{1-x}S$:Ce thin film alloys were sputter deposited and the composition and microstructure was characterized with x-ray diffraction. Electroluminescent devices were fabricated and the emission properties of these films were compared to the theoretical predictions.

Background

The highest reported luminance and efficiency for pure SrS:Ce ACTFEL devices was 100 cd/m^2 and 0.8 lum/W, respectively. In the SrS:Ce phosphor system, Ce^{+3} ions substitute for Sr^{+2} lattice sites (Ce_{Sr}). Figure 4-1 shows the blue-green emission spectra of SrS:Ce which results from the $^2D(5d)$-$^7F_{5/2}(4f)$ and $^2D(5d)$-$^7F_{7/2}(4f)$ Ce^{+3} transitions. SrS has the NaCl crystal structure therefore, the symmetry of the Ce^{+3} in the SrS is octahedral. Figure 4-2 shows the octahedral arrangement of the Ce^{+3} ion in the SrS matrix.

SrS:Ce was first introduced as a potential blue ACTFEL phosphor in 1984 by Barrow et al. [BAR 84]. Several different deposition techniques have been explored as a way to produce bright blue SrS:Ce EL films, such as electron beam evaporation [TAN 85], sputtering [OHN 90], atomic layer epitaxy (ALE) [LEP 91], multisource deposition NIR 88], and reactive evaporation [MAU 92]. Because there is a valence mismatch between the Ce^{+3} and the Sr^{+2}, many groups have also investigated different co-dopants to compensate for the local charge imbalance, including F, Cl, Na, P, Mn, and Ga (as well as various combinations). While each of the co-dopants shift the SrS:Ce emission spectra to slightly lower energies, there is a concomitant increase in the luminance and efficiency. Several groups have also investigated the effects of post-deposition annealing in different atmospheres (Ar [OKA 93], Ar-S [OHM 92], N) and each showed significantly increased brightnesses versus the as-deposited devices. It is generally thought that annealing the SrS:Ce films leads to decreased point, line, and grain boundary defects which are non-radiative recombination sites.

Low temperature PL measurements of MgS:Ce [ASA 80], CaS:Ce [ASA83], and SrS:Ce [YAM 87] in the literature have demonstrated a systematic blue shift in the emission spectra when the AE metal goes from Mg to Ca to Sr. In addition, Maneval et al. [MAN 94] synthesized $Ca_xSr_{1-x}S$:Ce powders and showed a gradual increase in the Ce PL transition energy as the Sr/(Ca+Sr) ratio approached one. Figure 4-3 is a plot of the reported change in the emission energy (relative to CaS:Ce) for the 4f-5d transition as a function of the AE-S bond length.

Experimental Procedure

To understand how the host lattice affects the Ce^{+3} radiative transitions, semiempirical molecular orbital calculations were performed for Ce doped alkaline earth sulfide phosphors (where AE was Mg, Ca, and Sr, respectively). Crystal field calculations were also performed to further model these phosphor systems. While Ba parameters were not available for molecular orbital calculations, crystal field calculations were also made to predict the transition energy for a $Sr_xBa_{1-x}S$:Ce alloy.

To compare the theoretical predictions, thin film $Sr_xBa_{1-x}S$:Ce phosphors were prepared by rf magnetron sputtering from compacted BaS:Ce and SrS:Ce powder targets supplied by David Sarnoff Research Center. The substrates were mounted on a rotating substrate holder so alternating layers of SrS:Ce and BaS:Ce could be grown. To vary the Sr and Ba composition, different sputtering pressures were used and the sputtering powers for the SrS:Ce target and the BaS:Ce target were varied. Table 4-1 lists the processing conditions for each of the thin film alloys that were grown. The $Sr_xBa_{1-x}S$:Ce were deposited onto both silicon substrates and thin film EL device substrates (glass/ITO/ATO/ZnS). The silicon substrates were used for PL measurements while the thin film EL substrates were used for x-ray diffraction analysis and were then fabricated into full EL devices.

In order to investigate the crystal structure and film composition, x-ray diffraction patterns of several thin films were taken with a Phillips APD 3720. PL spectra were measured to determine the peak position of the Ce^{+3} emission in the these alloys. A He-Cd laser (325 nm excitation) was used and the spectra were measured at room temperature. Finally, the $Sr_xBa_{1-x}S$:Ce thin films were fabricated into full devices and the following EL properties were measured with a Pritchard PR-650 spectrometer/calorimeter by driving the devices at 60 Hz from 0-300V: Vth, L_{40}, Eff_{40}, and the CIE coordinates.

Results

The results of the semiempirical molecular orbital calculations for the Ce^{+3} 4f and 5d levels are given in tabular form in tables 4-2, 4-3, and 4-4. For the Ce^{+3} free ion (i.e. gas phase), table 4-2 compares the experimental [MOE 63] and calculated energy levels while table 4-3 compares the experimental and calculated 4f and 5d spin orbital splitting. Table 4-4 compares the measured and calculated energy levels in the MgS, CaS, and SrS host lattices and table 4-5 shows the measured and calculated 4f and 5d spin orbital splitting.

Because the crystal field calculations only treats the splitting of the 5d level, these calculations were used to compare the change in the transition energy rather than the absolute transition energy. Figure 4-4 shows the calculated change in the emission energy versus the AE-S bond length (relative to CaS:Ce) for the MgCaS:Ce and CaSrS:Ce alloys. Finally, figure 4-5 shows the predicted change in the emission spectra for the $Sr_xBa_{1-x}S$:Ce alloy.

For the $Sr_xBa_{1-x}S$:Ce alloys that were grown, the as-deposited XRD patterns for samples L6A1-L6B2 all demonstrated single diffraction peaks for each orientation which suggested that the SrS:Ce and BaS:Ce mixed thoroughly during the deposition to form a solid solution. While XRD patterns were not taken for higher BaS concentrations (>50.2% BaS), the XRD data suggested that BaS and SrS may have complete solubility, which was expected because these compounds satisfy the Hume-Rhothery rules. A summary of the XRD results for samples L6A1-L6B2 are given in table 4-6. Included in the table is the (220) d-spacing, and the calculated SrS and BaS composition, respectively. Because BaS and SrS both have the sodium chloride crystal structure, the $Sr_xBa_{1-x}S$:Ce thin film composition was estimated using Vegard's law (L6A3 and L6A5 d-spacing was used to represent pure BaS and SrS, respectively). The (220) peak was used for the Vegard's law calculations because it was the dominant XRD peak in most of the thin films. While XRD patterns were not taken for samples L6B3-B8, the BaS and SrS concentrations were estimated assuming the sputter rate ratio of SrS/BaS was 0.625. These values (denoted with an *) are also given in table 4-6.

PL emission spectra were measured on each $Sr_xBa_{1-x}S$:Ce thin film, however most of the film thicknesses were close to the emission wavelength and severe interference patterns were observed (i.e. figure 4-6). The interference patterns made it difficult to determine the peak position of the Ce^{+3} emission, however the emission appeared to shift from a blue-green to green-yellow (red shift), as the BaS concentration increased. Figure 4-7 shows the emission spectra for samples L6A1, L6A2, L6A3, and L6B4, respectively, which did not have interference peaks in the spectra. Figure 4-8 plots the change in the peak wavelength from figure 4-7 versus the approximate thin film composition which demonstrates gradual shift to lower energy at higher BaS concentrations. Finally, table 4-7 summarizes the EL results (Vth, L_{40}, Eff_{40}, and CIE coordinates) that were obtained from several $Sr_xBa_{1-x}S$:Ce EL devices.

Discussion

The objective of this study was understand the Ce^{+3} radiative transition so a bright blue EL phosphor could be engineered. Molecular orbital and crystal field models were used to understand the reported differences in the Ce^{+3} radiative transitions for different AES lattices (where AE is Mg, Ca, Sr). While molecular orbital theory was discussed in detail in chapter 3, crystal field theory will be discussed here. In particular, the effects that symmetry and ion spacing have on a luminescent center's energy levels will be considered.

Symmetry

The first property that will be considered is the symmetry that is associated with the specific lattice position of the luminescent center. When introduced into a pseudo-ionic solid, a rare earth ion substitutes for a cation site. Therefore, one is interested in how the nearest neighbor anions are arranged with respect to the cation site. In addition, it is important to understand the shape and symmetry of the electron orbitals involved in the radiative transition. For rare earth (lanthanide) transitions, both 4f-5d intershell and 4f-4f intrashell transitions occur. By examining the electron configuration of the lanthanide rare earths series, it can easily be shown that the 4f levels are shielded by the 5s and 5p electrons, and are subsequently unaffected by the host lattice. The lanthanide series have an electron configuration of: $1s^22s^22p^63s^23p^64s^23d^{10}4p^65s^24d^{10}5p^66s^24f^x$. While the radial probability distribution of the 4f orbital has its maxima closer to the nucleus than the 5s, 5p, and 6s orbitals, the 5s, 5p, and 6s orbitals fill first. This is due to the fact that the radial probabilty distribution of the 5s, 5p, and 6s penetrate closer to the nucleus and have local maxima that are greater than the 4f radial probability distribution near the nucleus. This phenomenon, called penetration, causes the 5s, 5p and 6s orbitals to fill before the 4f orbitals [ZUM 89 p.302]. Because the most probable distribution of the 5s, 5p and 6s level is radially farther from the nucleus however, the 4f orbitals are shielded by these outer orbitals (Figure 4-9). The 4f orbitals are therefore relatively immune to host lattice interactions which simplifies our discussion because only the 3d and 5d orbitals need to be considered.

The shape and symmetry of the d-orbitals have essentially 5 orientations: the d_{xz}, d_{xy}, and d_{yz} each have the same distribution, and the $d_{x^2-y^2}$ and d_{z^2} each have unique distributions. The energy level position associated with each orientation depends on how the neighboring anions are situated. For most of the metal sulfide hosts lattices, there are basically two types of crystal symmetries that are important: 1) octahedral symmetry (sodium chloride structure), and 2) tetrahedral symmetry (zinc blend structure). Each orbital orientation has an energy associated with it which is dependent on the orbital-ligand interaction. If one assumes that the anions are simply point charges, then the relative energy positions for each orbital orientation can be estimated. For octahedral symmetry, the d_{z^2} and the $d_{x^2-y^2}$ lobes point directly at the anions and the d_{xz}, d_{xy}, and d_{yz} lobes point between anions. Because the anion interaction is stronger for the d_{z^2} and the $d_{x^2-y^2}$ lobes versus the d_{xz}, d_{xy}, and d_{yz} lobes, the d_{z^2} and the $d_{x^2-y^2}$ are repelled more and have a higher energy than the d_{xz}, d_{xy}, and d_{yz} orientations. A similar argument can be applied to the tetrahedral symmetry which demonstrates that for this arrangement, the d_{xz}, d_{xy}, and d_{yz} have a higher energy relative to d_{z^2} and the $d_{x^2-y^2}$ orientations. Though it will not be derived here, simple geometric considerations show that the d-orbital splitting (Δ) of the tetrahedral symmetry is $\frac{4}{9}$ the magnitude of the octahedral splitting ($\Delta_{tet} = \frac{4}{9}\Delta_{oct}$) [ZUM 89 p.922]. Figure 4-10 shows the d-orbital splitting for both the octahedral and tetrahedral symmetry.

Ion Spacing (Bond length)

In addition to point symmetry, the atomic energy level positions of the luminescent center are also dependent on the ion spacing or bond length of the host material. The bond length dependence of the d-orbital splitting can be easily understood by approximating the ions as point charges and considering Coulomb's law. Coulombs law relates the force (F) (or electric field) between two charged particles (q_1 and q_2) is written as:

$$(4\text{-}1)\quad F = \frac{q_1 q_2}{4\pi\varepsilon r^2}$$

and the electric field (E_q) due to charge q is,

$$(4\text{-}2)\quad E_q = \frac{q}{4\pi\varepsilon r^2}$$

where r is the distance between the point charges, and e is the permittivity of the medium between the two charges. These equations demonstrate the $\frac{1}{r^2}$ dependence of the electrostatic force and electric field between two charged particle, respectively. This implies that as the charged particles get closer together (small r), the force and electric field increase. Conversely, as charged particles get farther apart (large r) the force and electric field decrease. Applying this same logic to ions in a solid, as the bond length decreases (small r) between anions and cations, the crystal field in the solid increases. Conversely, when the bond length increases (large r), the crystal field decreases and the atomic states become more like the free ion case. From this, it is possible to consider how the energy levels of rare earth ions are affected by the host lattice.

Here again, the discussion will be limited to the d-orbital splitting because these orbitals are the only ones affected by the host lattice for rare earth ions. The results of the so-called "point charge model" can be used to demonstrate how the bond length modifies or splits the d-orbitals [GER 73 p.31]. This model represents anions with point charges, and takes into account the radial nature of the d-orbital wavefunction (while only the result of the point charge model will be considered here, interested readers are referred to [Gerloch] for a thorough derivation). It should be noted that for the metal sulfides that are of interest, this model is a good approximation because the bonding in these materials is primarily ionic. The point charge model applied to d-orbital splitting results in the simple algebraic expression [GER 73 p.36]:

$$(4\text{-}3)\quad Dq = \frac{1}{6} z e^2 \left(\frac{r^4}{a^5} \right)$$

where Dq is a measure of the energy level separation, z is the charge or valence of the anion, e is the charge of an electron, r is the radius of the d wavefunction, and a is the bond length. Equation 4-3 clearly shows that when a radiative transition involves an outer d-orbital (3d or 5d), the emission color can vary depending on the lattice spacing of the host material. When the symmetry of the cation site is considered, the magnitude of the d-orbital splitting for octahedral symmetry is given by 10Dq, and tetrahedral symmetry given by $\left(\frac{4}{9}\right)$10Dq. The splitting of these levels relative to the free-ion condition is illustrated in figure 4-11, and the influence that the bond distance has on the splitting is demonstrated in figure 4-12.

Molecular Orbital Cluster Calculations

To model the Ce doped alkaline earth sulfide radiative transitions, semiempirical molecular orbital cluster calculations were performed. The model used is referred to as the configuration interaction spectroscopic version of the intermediate neglect of differential overlap (INDO/S-CI) model [KOT 91]. The f-orbital-containing systems were recently parameterized which made it possible to calculate the spectroscopy of the Ce^{+3} rare earth ion [CUL 87]. In addition to calculating the splitting that results from molecular orbital overlap, calculations of the spin orbital splitting were also performed. This splitting is due to the interaction of an electron's spin and orbital momentum, which is significant for rare earth atoms.

Before discussing the specific results that were obtained, it is necessary to briefly review the details of the semiempirical calculation and also discuss some of the simplifications that were utilized. First of all, the main goal of quantum chemistry is to write a set of wave functions which describe all of the particles (nuclei and electrons) in a given system. The wave function for a molecule can be described as a solution of Schrodinger's time independent wave equation,

$$(4\text{-}4)\quad \hat{H}\Psi = E\Psi$$

where H is the Hamiltonian operator, Ψ is the wavefunction and E is the energy of the molecule. The Hamiltonian operator is a summation of five operators which is expressed by:

$$(4\text{-}5)\quad \hat{H} = \frac{1}{2}\sum_{A}^{N}\nabla_A^2 + \sum_{A,B}^{N}\frac{Z_A Z_B}{R_{AB}} + \frac{1}{2}\sum_{i}^{n}\nabla_i^2 + \sum_{i,A}^{n,A}\frac{Z_A}{r_{iA}} + \sum_{i,j}^{n}\frac{1}{r_{ij}}\ ,$$

where Z_A and Z_B is the charge of nucleus A and B, respectively, R_{AB} is the distance between particles A and B, r_{iA} is the distance between the electron i and the particle A, $r_{i,j}$ is the distance between electrons i and j, and ∇^2 is the square of the Laplacian operator which contains second derivatives with respect to the particle position. For the summation limits, N is the number of nuclei in the molecule, and n is the number of electrons. The first and third term corresponds to the nucleus and electron kinetic energy, respectively. The second term describes the Coulombic repulsion between the nuclei. The fourth term represents the Coulombic attraction between the nuclei and electrons. The fifth term is the Coulombic repulsion between the electrons. While some ab initio quantum calculations solve each of these contributions analytically, semiempirical calculations simplify several of these terms to make larger atom clusters more tractable. While the mathematical details will not be presented (see reference [KOT 91] for details), a qualitative description of the simplifications will be discussed.

The first simplification employed was that the kinetic energy of the nuclei was set to zero, which was a reasonable assumption because the speed that the nucleus travels is negligible compared to that of the orbiting electrons. Second, the repulsion between the nuclei was treated as a constant, since their positions were assumed to be constant. The third simplification dealt with the electron-electron repulsion term. Because the energy of each electron depends on the positions of all the other electrons, they are coupled and mathematically inseparable. For these semiempirical calculations, each electron's energy was calculated separately, and therefore the interelectronic repulsion was only treated as a statistical average. This third approximation was actually the most severe, and therefore a method called "configuration interaction (CI)" was implemented to correlate the electrons. In this approach, the energy of different electron configurations are calculated as electrons are allowed to occupy otherwise unoccupied molecular orbitals.

Initially, calculations of the 4f and 5d energy levels for the Ce^{+3} free ion were performed to confirm that the Ce parameters were accurate. This system represented a Ce^{+3} ion at infinity without external perturbations of the energy levels (i.e., only spin-orbital interactions are considered). Table 4-2 shows the experimental gas phase analysis data for the Ce^{+3} ion which lists the energy level positions of the two spin orbital 4f levels ($4f_{5/2}$ and $4f_{7/2}$) and the two spin orbital 5d levels ($5d_{3/2}$ and $5d_{5/2}$) [MOE 63]. Table 4-2 also shows the calculated 4f and 5d spin orbital levels of the Ce^{+3} free ion which was generated by inputing a single Ce^{+3} ion without any ligands. Finally, table 4-3 lists the

4f and 5d spin orbital splitting for the experimental and calculated Ce^{+3} free ion. As demonstrated by tables 4-2 and 4-3, a very good agreement between the experimental and calculated energies was obtained. The calculated 5d energy levels were about 2500 cm^{-1} lower in energy than the experimental (42610 and 45085 versus 45045 and 47505), and the spin orbital splitting of the 5d and 4f levels were within 15 cm^{-1} (2475 cm^{-1} versus 2460 cm^{-1}) and 224 cm^{-1} (2173 cm^{-1} versus 2397 cm^{-1}) , respectively.

Subsequent to calculating the Ce^{+3} free ion energy levels, the thirteen ion cluster with the 15x15x15 matrix of +2 and -2 point charges was developed to calculate the Ce^{+3} energy levels in alkaline earth (Mg, Ca, and Sr) sulfide host lattices (see chapter three and figure 3-15 for details). Examination of the experimental electron energy levels for MgS:Ce, CaS:Ce, and SrS:Ce shown in tables 4-4 and 4-5 reveals two trends: 1) the 5d levels occur at higher energies (relative to the 4f levels) as the radius of the alkaline earth ion increases from Mg to Ca to Sr, and 2) the spin-orbit splitting of the 4f and 5d level decreased as the alkaline earth ion radius increased. While the differences between the calculated versus experimental energies increased from MgS to CaS to SrS, the calculated results show the same two trends as the experimental data. Figure 4-13 schematically illustrates the splitting of the 5d and 4f levels which demonstrates that the 5d level splitting is dominated by the molecular orbital splitting, while that of the 4f level is dominated by spin orbital splitting. The largest error in the calculations was the splitting of the 4f level, and though this splitting was important, its magnitude was relatively small compared to the difference between the 5d and 4f levels. Because transitions between the 5d and 4f levels (~20,000 cm^{-1}) were of interest, the error (~300 cm^{-1}) in the 4f splitting did not significantly impact the calculated photon energy of the luminescent transition.

Crystal Field Calculations

Because the Ce^{+3} luminescent center has octahedral symmetry in each alkaline earth sulfide host, the relative position of the excited 5d state for each material was determined assuming a constant 4f level. This was a justified procedure because the 4f electrons do not participate in bonding and are not significantly affected by the chemical surroundings. Figure 4-14 shows the crystal field energy level diagram of the Ce^{+3} 4f and 5d levels with octahedral symmetry. From figure 4-14, the 4f level splitting is dominated by spin orbital coupling (~2000cm^{-1}), and the 5d level splitting is dominated by the crystal field (~10,000 cm^{-1}). It should be noted that the higher 5d crystal field level lies in the conduction band in these AE sulfides, so only the position of the lower 5d crystal field level is important.

To calculate the relative 5d energy level position, equation 4-3 was used to calculate Dq where the radius of the Ce 5d wavefunction (r) was 0.08 nm, Z was 2, and the bond distance was set equal to half of the AE sulfide host lattice parameter ($a_o/2$). Table 4-8 lists the lattice parameters, and bond lengths for the appropriate AE sulfide lattices. Calculations for the two binary alloys (i.e., $Mg_xCa_{1-x}S$:Ce and $Ca_xSr_{1-x}S$:Ce) were also performed where the alloy lattice parameter was assumed to obey Vegard's law. The calculated change in the lower 5d crystal field level is compared to the reported empirical values as a function the AE-S bondlength in figure 4-4. The change in the lower 5d level also represents the change in the transition energy because the 4f level was assumed to be constant. Table 4-9 compares the empirical and calculated changes in the emission energy for MgS:Ce, CaS:Ce, and SrS:Ce. Figure 4-4 and table 4-9 demonstrate that while the point charge model accurately predicted the change in the Ce^{+3} transition energy for SrS versus CaS, it predicted a much lower transition energy value for the MgS versus CaS.

To understand why the point charge model accurately predicted the change between the CaS and SrS, but not for the MgS, the ionic radii for the Ce^{+3} and the AE^{+2} ions were compared. From tables 2-3 and 2-4, note that Ce^{+3} (0.11 nm) has a close ionic radius match with Sr^{+2} (0.113 nm) and Ca^{+2} (0.099 nm) but is much larger than Mg (0.078 nm). Therefore, while Ce^{+3} fits well in a Ca^{+2} or Sr^{+2} site, there must be a local expansion of the MgS lattice to accommodate the Ce^{+3} on a Mg^{+2} site. While Sher et al. [SHE 84] developed a sophisticated model to calculate the local bond distance for impurity atoms in semiconductors, the necessary bond energies for the Mg-S and Ce-S bonds have not reported. Therefore the local bond distance (a_{loc}) used for the MgCaS:Ce calculations were determined from the expression:

$$(4\text{-}6)\quad a_{loc} = \left(\frac{\frac{a_o}{2} - IR_{S(-2)} + IR_{Ce(+3)}}{2} \right) + IR_{S(-2)}\,,$$

where again a_o was the lattice parameter, and $IR_{S(-2)}$ and $IR_{Ce(+3)}$ were the ionic radii of the S^{-2} and Ce^{+3} ion, respectively. This expression assumed the bond distance was equal to the sum of the cation and anion radii, and that the host cation radius term ($a_o/2 - IR_{S(-2)}$) was replaced with a term representing the average ionic radius of the Ce^{+3} and the host cation. Figure 4-15 shows the corrected bond distance versus change in transition energy for a MgCaS:Ce alloy, which was in much better agreement with the experimental data. This supports the explanation that the MgS lattice locally expanded to accommodate the Ce^{+3}

luminescent center and lead to a large error between the calculated and experimental data.

Thin Film $Sr_xBa_{1-x}S$:Ce

Based on these calculations for Ce doped alkaline earth sulfides, it was thought that alloying the SrS:Ce with BaS would blue shift the emission spectra. The point charge calculations were extended to the $Sr_xBa_{1-x}S$:Ce alloy, and figure 4-16 compares the results for the uncorrected and corrected bond distances. The results suggest a blue shift (versus SrS:Ce) of 824cm^{-1} and 513cm^{-1} for the uncorrected and corrected BaS:Ce bond distances, respectively.

The CIE coordinates from EL data from the $Sr_xBa_{1-x}S$:Ce devices reported in table 4-7 do not show a blue shift versus pure SrS:Ce devices. In addition, there is no clear trends in the values of efficiency, L_{40}, and threshold voltage indicating better performance for $Sr_xBa_{1-x}S$:Ce alloys. From figure 4-17 the experimental change in the $Sr_xBa_{1-x}S$:Ce transition energy was found to conflict with the theoretical crystal field calculations. Even the corrected bond distance calculations suggested a small blue shift in the Ce^{+3} transition energy for $Sr_xBa_{1-x}S$:Ce alloys, whereas the experimental observations demonstrated a distinct red shift in the emission spectra for higher BaS concentrations. Sample L6B4, which had an estimated BaS concentration of ~10%, demonstrated a small blue shift in the Ce^{+3} emission spectra.

As discussed previously, Ce^{+3} substituted in the CaSrS:Ce alloy readily sits on the alkaline earth site because of the close ionic radius match. Even in MgS where there is undoubtedly distortion in the lattice to accommodate the Ce^{+3}, this distortion is likely isotropic so the symmetry is preserved. When the lattice site is larger than the substitutional ion the lattice locally contracts to accommodate the impurity. When there is significant mismatch however, it becomes energetically favorable for the impurity to be locally displaced in the lattice to avoid profuse vibration. This local displacement will change the local symmetry which can have a profound impact on the radiative transitions of a luminescent center.

The XRD results showed that a $Sr_xBa_{1-x}S$:Ce solid solution was formed over the range of SrS:Ce/BaS:Ce films that were grown. From table 4-6 a systematic increase in the d-spacing was observed with higher BaS:Ce concentrations which suggested that the average alkaline earth lattice site increased in size. Interpolating the data in figure 4-8, a minimum BaS concentration of ~20% was required to cause the red shift observed in the emission. Therefore, it is proposed that when the BaS concentration was > 20%, the alkaline earth site was too large for the Sr_xBaS_{1-x}:Ce lattice to accommodate the Ce^{+3} without a change in symmetry leading to a blue shift. For BaS concentrations < 20%, it was proposed that the Sr_xBaS_{1-x} lattice can accommodate a Ce^{+3} ion without a change in the local symmetry. Figure 4-18 shows schematically the proposed tetragonal distortion of the Ce^{+3} octahedral (O_h) symmetry which would result in a C_{4v} symmetry, and figure 4-19 shows qualitatively the change in the energy level positions of the Ce 5d orbitals to explain the observed red shift.

Summary

The reported Ce^{+3} radiative transitions in the MgS, CaS, and SrS host lattices were modeled with molecular orbital cluster and crystal field calculations. The model used for the molecular orbital calculations was the configuration interaction spectroscopic version of the intermediate neglect of differential overlap (INDO/S-CI) model. Excellent agreement between the reported and the calculated transition energies were obtained for Ce in MgS, CaS, and SrS, as demonstrated in table 4-4. The crystal field calculations assumed a point charge model, and the calculated difference in the emission energy between CaS:Ce and SrS:Ce was close to the experimental values (Figure 4-4). For the MgS:Ce, a simple model was developed to compensate for the local lattice expansion presumed to occur when large Ce^{+3} ions substituted for smaller Mg^{+2} ions. After correcting for this local lattice expansion, data in figure 4-15 showed that the crystal field model accurately described the change in the transition energy.

While molecular orbital calculations could not be performed for BaS:Ce, the crystal field model was used to predict the change in the Ce^{+3} transition energy. The bond distance calculation, corrected for a local lattice expansion, predicted a 513 cm^{-1} blue shift in the BaS:Ce transition energy relative to SrS:Ce. However, the emission spectra for BaS concentrations greater than 20% in $Sr_xBa_{1-x}S$:Ce thin films were red shifted relative to SrS:Ce. This red shift was attributed to a change in the Ce^{+3} octahedral symmetry to a C_{4v} symmetry. The EL performance of $Sr_xBa_{1-x}S$:Ce thin films did not show any consistent improvements versus pure SrS:Ce devices.

Table 4-1. Processing Conditions for Sputter Deposited $Sr_xBa_{1-x}S$:Ce Thin Films

Sample ID	Temp. (C)	Pressure (mtorr)	Time (hours)	BaS:Ce Power (W)	SrS:Ce Power
16a1	350	20	2	0	80
16a2	350	20	4	40	90
16a3	350	20	3	40	0
16a4	350	20	3	30	100
16a5	350	20	2	0	100
16a6	350	20	2	50	80
16a7(layered)	350	20	2	40	100
			1	0	100
16b1	350	20	3	30	100
16b2	350	20	3	20	100
16b3(layered)	350	7	1.5	0	100
			10(min)	30	0
			20	0	100
			10	30	0
			20	0	100
			10	30	0
			20	0	100
16b4(layered)	350	7	30(min)	0	100
			10	10	0
			20	0	100
			10	10	0
			20	0	100
			10	10	0
			20	0	100
16b5	350	7	2.5	5	100
16b7	350	20	3	60	80
16b8	350	20	3	80	80

Table 4-2. Experimental [MOE 63] and Calculated 4f and 5d Energy Levels of the Ce^{+3} Free Ion

Energy Level	Experimental (cm^{-1})	Calculated (cm^{-1})
$5d_{5/2}$	47,505	45,085
$5d_{3/2}$	45,045	42,610
$4f_{7/2}$	2,397	2,173
$4f_{5/2}$	0	0

Table 4-3. Experimental [MOE 63] and Calculated 4f and 5d Spin Orbital Splitting of the Ce^{+3} Free Ion

Energy Level Splitting	**Experimental (cm^{-1})**	**Calculated (cm^{-1})**
Δ5d	2,460	2,475
Δ4f	2,397	2,173

Table 4-4. Experimental [ASA 80, ASA 83, YAM 87] and Calculated 4f and 5d Energy Levels of Ce^{+3} in AES Host Lattices (where AE is Mg, Ca, and Sr)

Energy Level	**MgS:Ce (cm-1)**		**CaS:Ce (cm-1)**		**SrS:Ce (cm-1)**	
	Experiment	Calculated	Experiment	Calculated	Experiment	Calculated
$5d_{5/2}$ (T_{2g})	21,340	22,550	22,017	23,361	23,164	27,381
$5d_{3/2}$ (T_{2g})	20,340	21,402	21,088	22,302	22,287	26,408
$4f_{7/2}$	2,980	2,700	2,847	2,427	2,710	2,331
$4f_{7/2}$	2,870	2,531	2,753	2,362	2,656	2,290
$4f_{7/2}$	2,580	2,313	2,542	2,302	2,524	2,263
$4f_{5/2}$	520	282	461	96	429	51
$4f_{5/2}$	0	0	0	0	0	0

Table 4-5. Experimental [ASA 80, ASA 83, YAM 87] and Calculated 4f and 5d Spin Orbital Splitting of Ce^{+3} in AES Host Lattices (where AE is Mg, Ca, and Sr)

Energy Level Splitting	**MgS:Ce (cm-1)**		**CaS:Ce (cm-1)**		**SrS:Ce (cm-1)**	
	Experiment	Calculated	Experiment	Calculated	Experiment	Calculated
Δ5d	1,000	1,148	929	1,059	877	973
Δ4f	2,580	2,313	2,542	2,302	2,524	2,263

Table 4-6. Experimental XRD d-spacing and the Calculated Compositions of the $Sr_xBa_{1-x}S$:Ce Thin Films

Sample ID	d-spacing of 220 (Angstroms)	Calculated BaS%	Calculated SrS%
L6A1	2.1538	6.6 (pure SrS)	93.4
L6A2	2.2003	41.5	58.5
L6A3	2.2784	100	0
L6A4	2.1786	25.2	74.8
L6A5	2.145	0	100
L6A6	2.2119	50.2	49.8
L6A7	2.1965	38.6	61.4
L6B1	2.1829	28.4	71.6
L6B2	2.1703	18.9	81.1
L6B3		* ~ 10	* ~ 90
L6B4		* ~ 6	* ~ 95
L6B5		* ~ 7	* ~ 93
L6B7		* ~ 55	* ~ 45
L6B8		* ~ 62	* ~ 38

Table 4-7. EL Device Properties for the $Sr_xBa_{1-x}S$:Ce Thin Films

Sample	V_{th} (Volts)	Luminance L40 at 60Hz (fL)	Efficiency (lm/W)	CIE coordinates	
				x	y
L6A1	136	1.10	0.027	.201	.351
L6A2	221	2.98	0.038	.245	.431
L6A4	171	3.26	0.074	.238	.449
L6A5	127	1.27	0.049	.186	.345
L6A6	186	1.03	0.015	.287	.487
L6A7	232	3.36	0.040	.226	.417
L6B1	191	3.79	0.076	.233	.444
L6B2	182	4.41	0.094	.220	.423
L6B7	213	1.18	0.013	.285	.485

Table 4-8. Lattice Parameters and Bond Lengths for the AES Host Lattices (where AE is Mg, Ca, Sr, and Ba)

Alkaline Earth Sulfide	**Lattice Parameter (nm)**	**Bond Length (nm)**
MgS	0.52	0.26
CaS	0.567	0.284
SrS	0.602	0.301
BaS	0.638	0.319

Table 4-9. Experimental [ASA 80, ASA 83, YAM 87] and Calculated Change in the Emission Energy for Ce^{+3} in AES Host Lattices (where AE is Mg, Ca, and Sr)

Alkaline Earth Sulfide	**Calculated Change in Emission Energy(cm^{-1})**	**Empirical Change in Emission Energy (cm^{-1})**
MgS	-2,356	-750
CaS	0	0
SrS	1,126	1,303

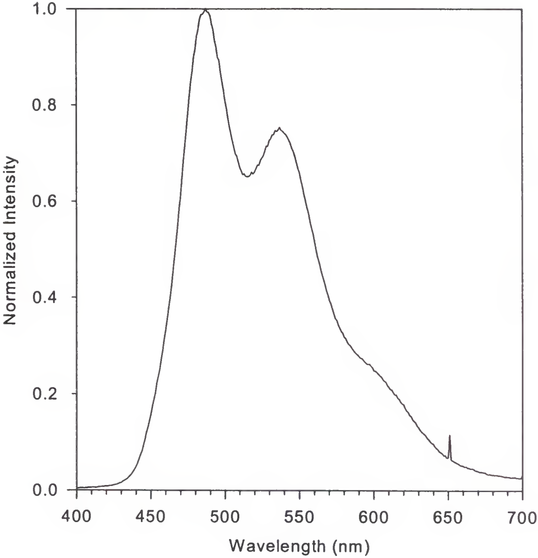

Figure 4-1. SrS:Ce EL emission spectra.

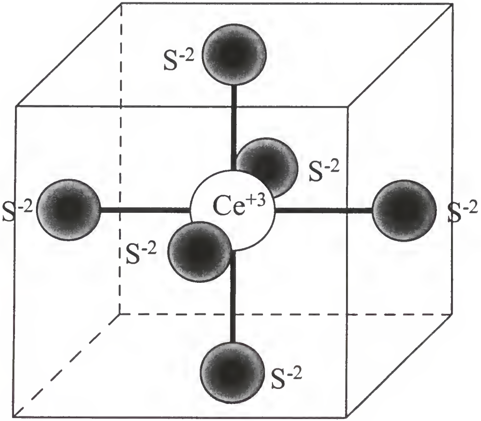

Figure 4-2. Schematic of the octahedral symmetry of the Ce^{+3} ion in the SrS host lattice.

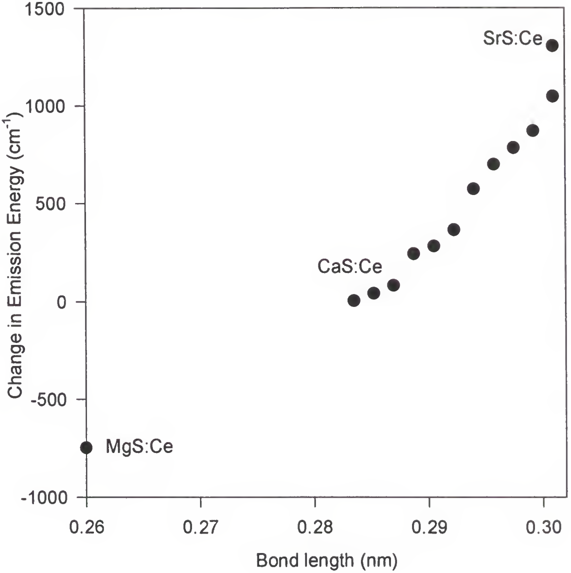

Figure 4-3. Experimental change in the emission energy (relative to CaS:Ce) as a function of bond length for different Ce^{+3} doped alkaline earth sulfides [ASA80, ASA 83, YAM 87, MAN 94].

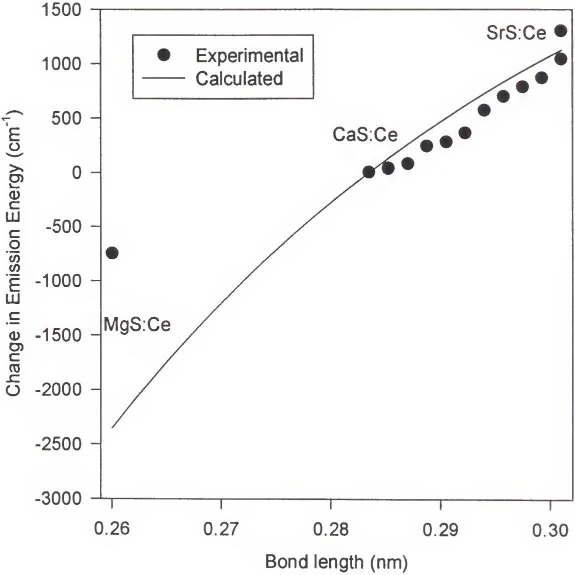

Figure 4-4. Calculated and experimental change in the emission energy (relative to CaS:Ce) as a function of bond length for different Ce^{+3} doped alkaline earth sulfides.

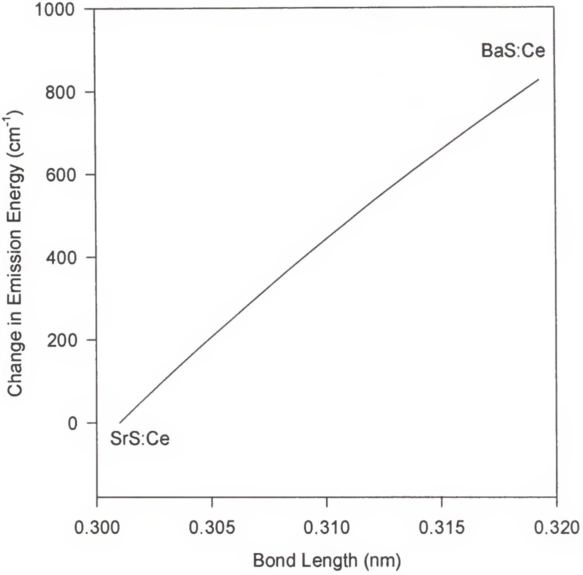

Figure 4-5. Predicted change in the emission energy as a function of the bond length for $Sr_xBa_{1-x}S$:Ce.

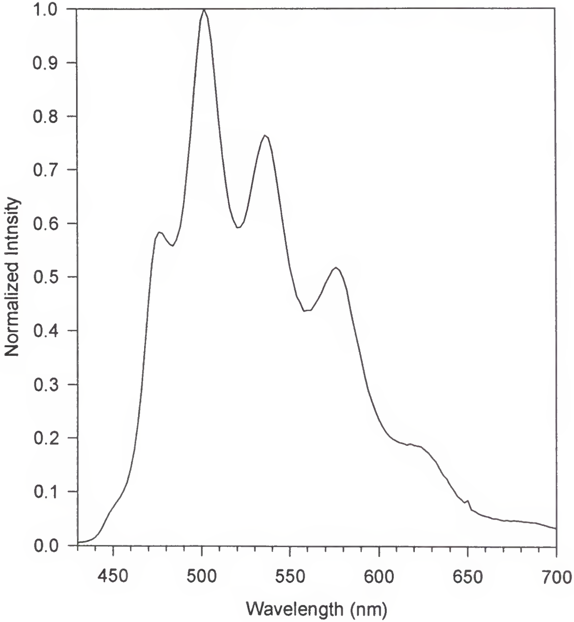

Figure 4-6: Example of a PL emission spectra for a $Sr_xBa_{1-x}S$:Ce PL that had optical interference patterns due to the thickness of the film.

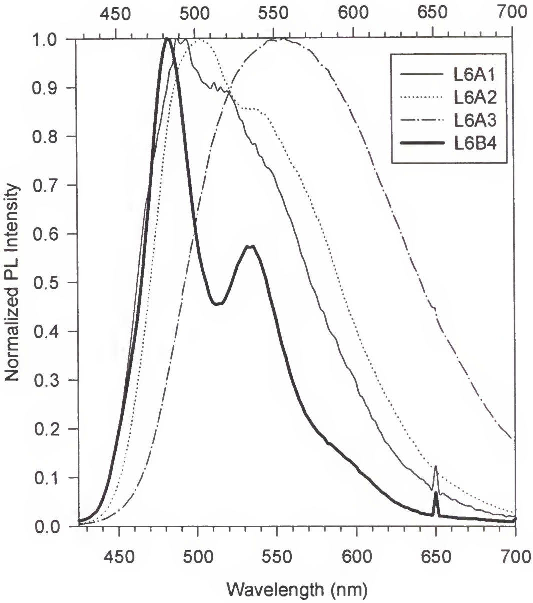

Figure 4-7. Emission spectra for several $Sr_xBa_{1-x}S$:Ce thin film samples (L6A1, L6A2, L6A3, L6B4).

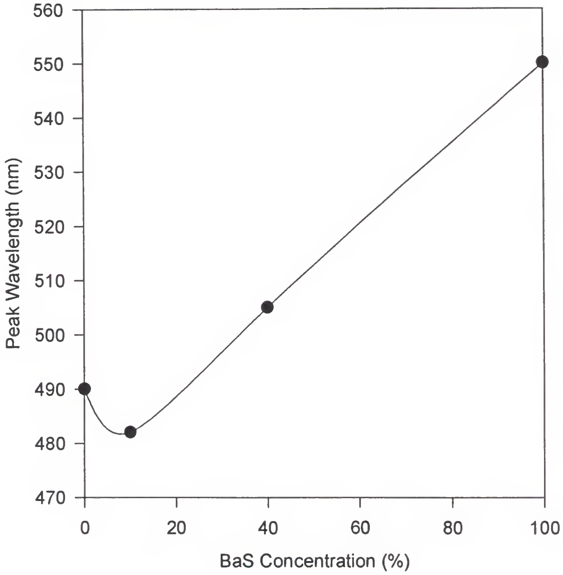

Figure 4-8. Peak wavelengths from figure 4-7 plotted as a function of the BaS concentration. Figure demonstrates an initial blue shift in the peak wavelength at low BaS concentrations and then a red shift at higher BaS concentrations.

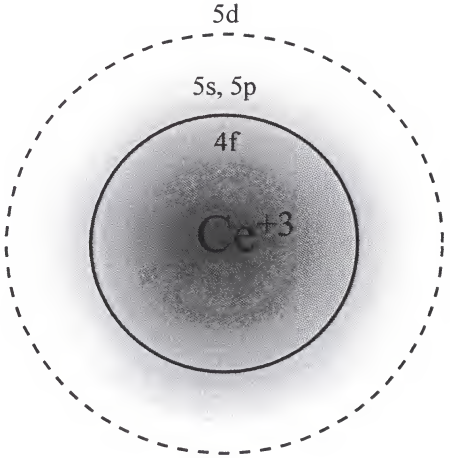

Figure 4-9. Schematic of the Ce^{3} ion which shows the radial positions of the outer orbitals. This figure demonstrates that the 4f level is shielded by the 5s and 5p elcetrons, and the 5d level is unshielded.

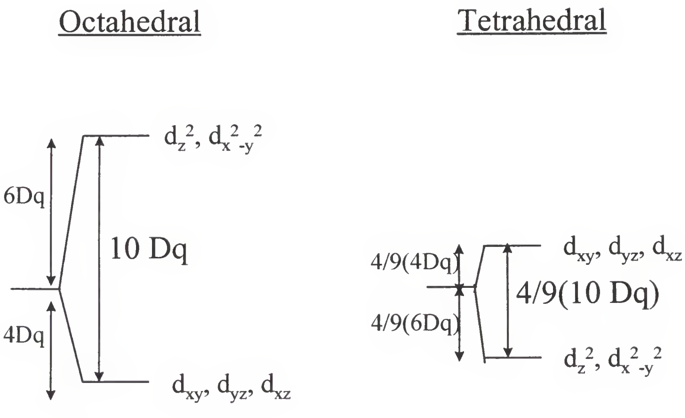

Figure 4-10. The relative d-orbital crystal field splitting for an octahedral and tetrahedral symmetry.

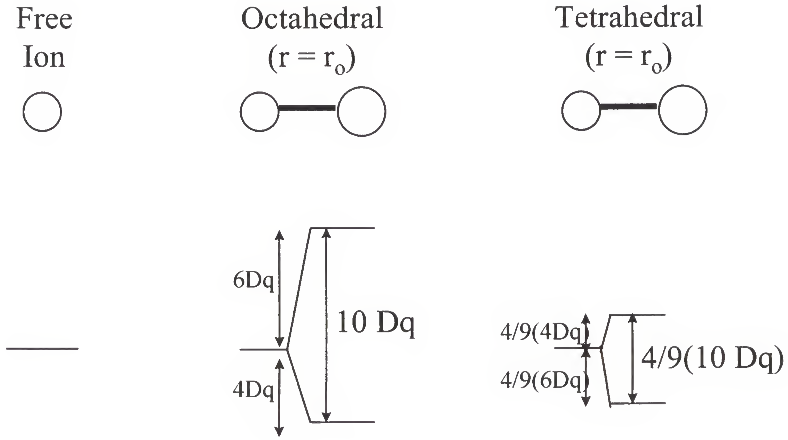

Figure 4-11. The relative d-orbital crystal field splitting for an octahedral and tetrahedral symmetry versus the free ion .

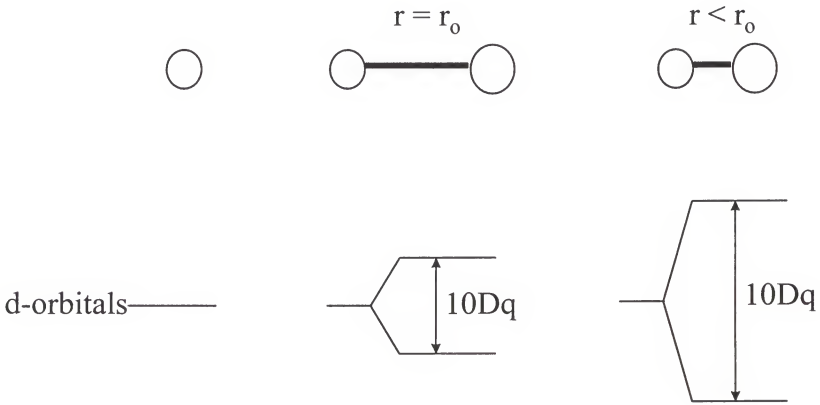

Figure 4-12. Schematic showing the influence of the bondlength on the d-orbital crystal field splitting.

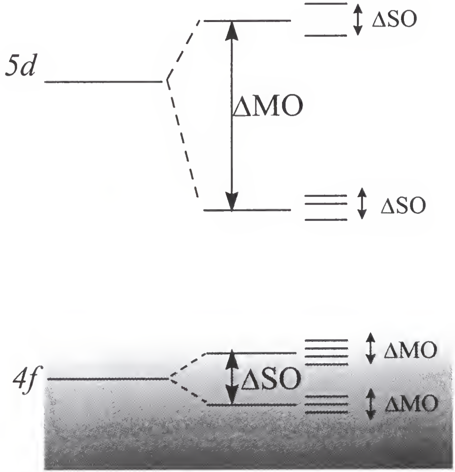

Figure 4-13. Schematic energy level diagram showing that for molecular orbital theory, the 4f splitting is dominated by spin orbital (SO) interactions and the 5d splitting is dominated by molecular orbital (MO) interactions.

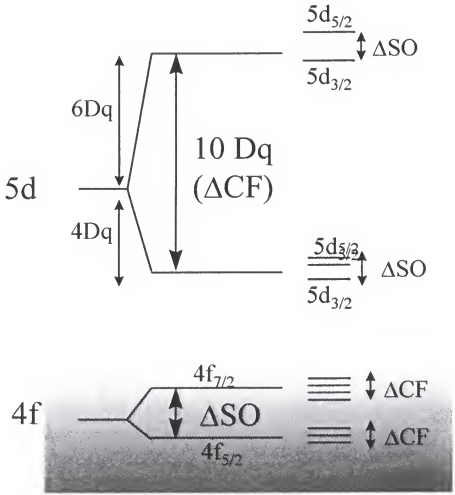

Figure 4-14. Schematic energy level diagram showing that for crystal field theory, the 4f splitting is dominated by spin orbital (SO) interactions and the 5d splitting is dominated by crystal field (CF) interactions.

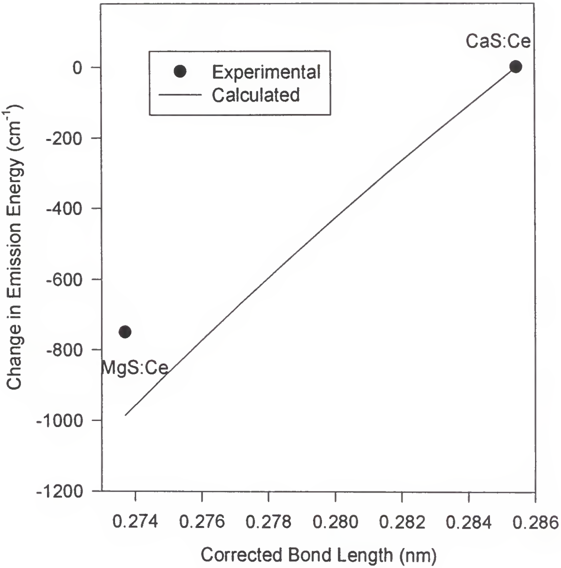

Figure 4-15. Experimental and crystal field calculations for the change in the emission energy (relative to CaS:Ce) versus the corrected bond length for $Ca_xMg_{1-x}S$:Ce.

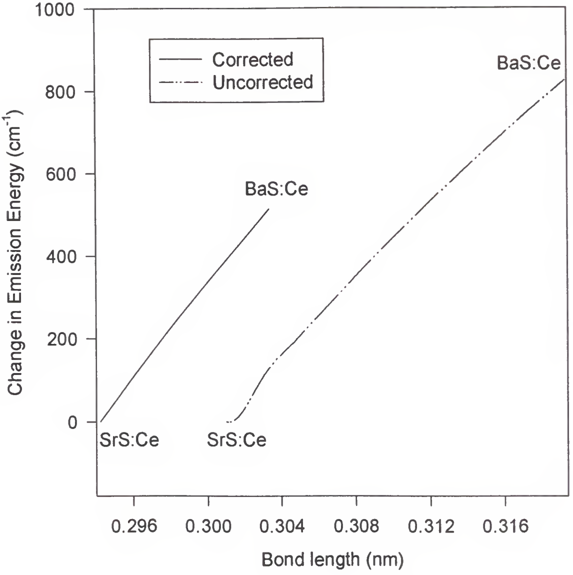

Figure 4-16. Crystal field calculations for the change in the emission energy (relative to SrS:Ce) versus the corrected and uncorrected bond lengths for $Sr_xBa_{1-x}S$:Ce.

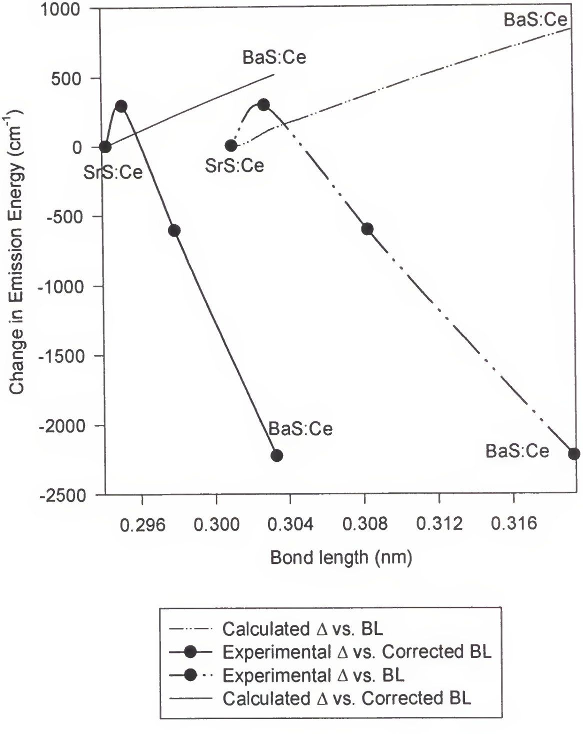

Figure 4-17. Crystal field calculations and experimental data of the change in the emission energy (relative to SrS:Ce) versus the corrected and uncorrected bond lengths for $Sr_xBa_{1-x}S$:Ce.

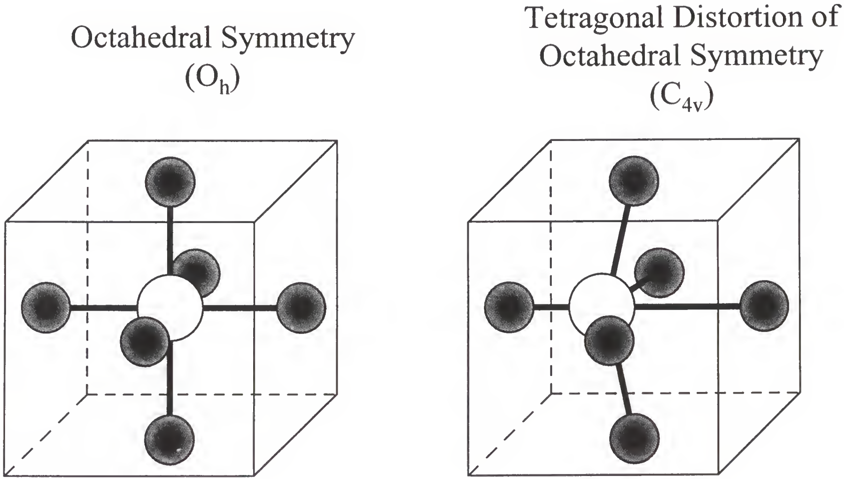

Figure 4-18. Illustration of an octahedral and a tetragonally distorted octahedral arrangement. The observed red shift that occurs in the $Sr_xBa_{1-x}S$:Ce thin films is attributed to this distortion.

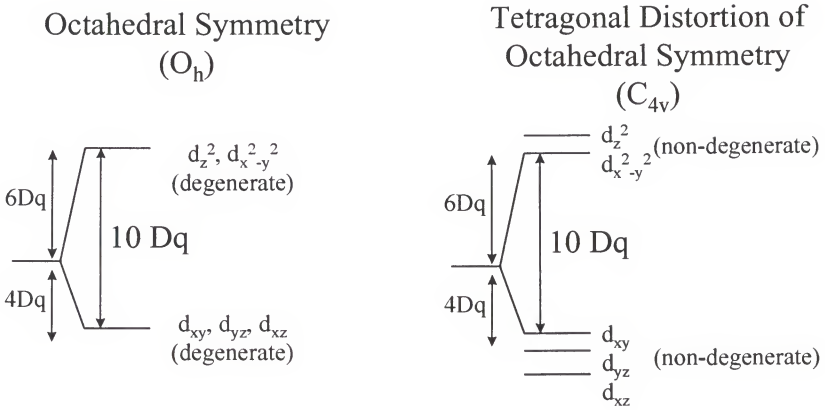

Figure 4-19. Energy level diagram which shows the qualitative effect of a tetragonally distorted octahedral symmetry. The crstal field levels are no longer degenerate because of the change in the ion position, and therefore some of the energy levels are at a lower energy

CHAPTER 5

SrS:Te BOUND EXCITONS

Introduction

This chapter describes the synthesis and characterization of SrS:Te powders which were found to have two high energy emission bands under photoluminescent excitation. To understand the radiative recombination mechanism, PL emission spectra were measured as a function of temperature. A simple configuration coordinate model was used to explain the emission band broadening and luminescence quenching that was observed with increasing temperature. Luminescence decay measurements were also performed, and the empirically determined transition rates were compared to theoretical calculations. Finally, SrS:Te ACTFEL devices were fabricated and tested under EL excitation.

Background

The idea of an isoelectronic trap was first introduced by Thomas et al. [THO 65] in 1965 when they used this theory to describe the photoluminescence observed in GaP:N. They suggested that even though nitrogen had the same valence as phosphorus (isoelectronic), nitrogen acted as an electron trap in the GaP lattice. They reasoned that because nitrogen is significantly more electronegative than phosphorus, electrons are preferentially trapped at nitrogen sites. Subsequently, the N-electron complex has a net negative charge which sets up a short range coulombic attraction for holes. Finally, when the hole is trapped, the electron and hole couple together and form an exciton. Because they are bound spatially in the nitrogen vicinity, these excitons are called bound excitons.

Since this model was suggested, the luminescent properties of other III-V, II-VI, and I-VII materials have been described by it. The focus of this discussion will be on bound excitonic behavior in II-VI semiconductor materials, and in particular MS:Te (where M = Zn, Cd, or Sr). For MS:Te semiconductors, the bound exciton formation is similar to the GaP:N system except that the S host anion has a larger electronegativity than Te dopant. Because Te has a higher hole affinity than S, holes are trapped at Te sites forming a Te-hole complex. The Te-hole complex has a net positive charge which induces a coulombic attraction for electrons. When the electron is trapped at this complex, a bound exciton is formed.

Of the MS:Te systems, CdS:Te and ZnS:Te have been studied the most. Aten et al. [ATE 65] first reported luminescence at 77K in lightly doped CdS:Te ($10^{18}cm^{-3}$). They observed an emission band at 600 nm which was largely quenched at room temperature. Cuthbert and Thomas [CUT 68] later investigated both lightly and heavily doped CdS:Te ($10^{18}cm^{-3}$-$10^{20}cm^{-3}$). They observed the 600 nm band and discovered another emission band at 730 nm in heavily doped samples. They attributed the 600 nm band to single Te_S sites (where Te_S represents a Te atom sitting substitutionally for a sulfur lattice site), and the 730 nm band to Te_S-Te_S pairs. They measured electron beam excited fluorescence spectra as a function of temperature and found that while the 600 nm band quenched severely above 175K, the 730 nm band was stable up to room temperature. Later, Rossler [ROE 70] extensively studied the CdS:Te system, and from temperature dependent photoluminescent excitation and emission spectra he developed a configuration coordinate model to describe the CdS:Te bound exciton behavior. The 600 nm band zero-phonon line was estimated to be at 2.36 eV, and the phonon energy of the ground state and excited state was reported to be 21 and 14 meV, respectively. The thermal quenching of the luminescence was described, and it was found that the addition of shallow donors helped to raise the temperature where significant quenching of the luminescence occurred.

Isler and Strauss [ISL 70] were the first to report the optical properties of the ZnS:Te system. They showed two emission bands for the ZnS:Te with peak energies at 3.2 and 2.8 eV for the wurtzite phase and 3.1 and 2.7 eV for the zincblende phase. They also attributed the high energy peaks to Te_S sites and the low energy peak to Te_S-Te_S sites. Fukushima and Shionoya [FUK 73] also studied the ZnS:Te system, and determined the phonon energies of the ground states and excited states, respectively. They also developed a configuration coordinate model to explain the bound exciton behavior in ZnS:Te, and used a similar model to describe the thermal quenching behavior they observed.

In this work, SrS:Te powders were synthesized and bound exciton emission from SrS:Te is reported for the first time. The luminescence properties of the SrS:Te powders are discussed in detail. In particular, the binding energy, the phonon energy, and the activation energy of non-radiative recombination for the bound excitons have been determined from temperature dependent PL emission spectra measurements. Finally, the physical meaning of the SrS:Te bound exciton binding energy, phonon energy, and activation energy for non-radiative recombination is discussed.

Experimental Procedure

SrS:CeTe, and SrS:Te powders were synthesized by mixing different amounts of SrS, SrTe, with and without CeF_3 (SrTe = 5, 10, 15, and 20 wt. %, SrS = 100 - SrTe wt. %, and CeF = 0 or 1 mol%). The powder mixtures were then fired at 850C for 1 hour in a nitrogen atmosphere, where they were cooled and then mixed with a mortar and pestle. The firing and mixing step was repeated for a total of 4 cycles for the SrS:Te,Ce powders and 6 cycles for the pure SrS:Te powders (i.e., 4 hours and 6 hours of total firing time).

For the SrS:Te,Ce powders, temperature dependent photoluminescent measurements were taken with a 275 nm Ar ion laser. The 275 Ar ion laser had a 295 nm filter at the spectrometer to filter any reflected laser light, and the PL spectra were measured with a 1 nm resolution and the typical wavelength range was 300-500 nm. A liquid helium cold finger was used to cool the powder samples, and a temperature controller was used to monitor the sample temperature during the PL measurements. X-ray diffraction scans were taken at room temperature for each powder using a Phillips APD 3720 diffractometer. For the Ce co-doped powders, electron paramagnetic resonance (EPR) data were collected to determine the concentration of Ce^{+3} incorporated into the powders. Finally, cathodoluminescence (CL) efficiency measurements were measured for a range of voltages (500-5000V) with a target current of 0.5 μA over a 0.06 cm^2 area using a VG 32 E-gun

For the SrS:Te powders, XRD data were again taken for these powders to characterize the composition and crystal structure, and the 275 Ar ion laser was used to measure temperature dependent PL emission spectra with similar settings as discussed above. For this set of powders, however, temperature dependent PL spectra were also measured with a 325 nm He-Cd laser. The 325 nm He-Cd laser had a 350 nm filter at the spectrometer to filter any reflected laser light, and the spectra were measured with a 1 nm resolution and a 350-550 nm wavelength range.

To determine whether the SrS:Te thin films would emit under EL excitation, thin films were grown by molecular beam epitaxy (MBE) onto silicon and EL device substrates. To confirm whether Te was incorporated into the SrS, PL emission spectra of the SrS:Te thin films were measured using the Ar ion laser described above. The thin films were also used to measure the Te concentration responsible for the observed PL in the SrS:Te powders. Rutherford back scattering (RBS) was used to measure the Te concentration in one of the SrS:Te thin films.

Results

The normalized room temperature PL data (275nm excitation) for each SrS:Te,Ce composition is shown in figure 5-1. The emission peak maxima was approximately 400 nm, with a small shoulder at 475nm which varied from about 20-35% of the maximum peak intensity. The emission spectra of two powders (initial SrTe concentration of 10 (1A) and 15 (1B) wt % SrTe) were measured as a function of temperature to investigate the temperature dependence of the emission bands. Figure 5-2 shows the normalized emission spectra at 25K and the corresponding PL intensities as a function of temperature for these SrS:Te,Ce powders. For the lower Te concentration powder (1A), three peaks were observed (360, 400 and 475 nm), while in the higher Te concentration powder (1B), only the two peaks observed at room temperature (400 and 475 nm) were evident. For powder 1A, the three emission bands were observed up to 200K. For temperatures above 200K the high energy band (360 nm) was quenched and only the lower energy bands (390 and 475 nm) remained. For powder 1B only the low energy emission bands (390 and 475 nm) were observed over the entire temperature range.

For each powder, the XRD patterns contained peaks from both SrS and SrTe with the (200) and (220) peaks being dominant for both. High resolution scans of the SrS (200) and the SrTe (220) peaks were collected to determine if there were shifts in the XRD peaks from the fired powder mixtures relative to pure SrS and SrTe. Table 5-1 summarizes the high resolution XRD results which demonstrates the very small shifts in the SrS and SrTe peaks that were observed. While the small peak shifts in the XRD patterns suggested a small amount of Te incorporation ($< 10^{21}$ cm^{-3}), the peak shifts were not significant enough to precisely determine the Te concentration. Because not all of the SrTe went into solution with the SrS, at 850C there was either limited solubility for Te in SrS, or the Te diffusion in SrS was kinetically limited. The excess SrTe in the powders made it difficult to experimentally determine the Te concentration in the SrS:Te particles. The approximate Te concentrations will be discussed further in the discussion section.

The EPR measurements on the Ce-doped powders revealed that while 1 mol.% CeF_3 was introduced in the starting powders, there was < 0.01 mol.% Ce^{+3} in the fired powders. The room temperature CL efficiency was measured for three (initial SrTe concentrations of 5, 10, and 15 wt. %) of the SrS:Te,Ce powders and the highest efficiency obtained was 0.2 lum/W at 4000V and λ_{max} = 400nm (3.1 eV). Table 5-2 summarized the results of the CL efficiency measurements. It should be mentioned that while these are relatively low efficiencies, this efficiency is a photopic measurement which is known to have low sensitivity at high energies. Therefore, while the eye does not respond well to this emission (400 nm), it may have good emission properties.

The normalized room temperature PL data (325 nm excitation) for the second batch of SrS:Te powders (noCeF_3) are shown in figure 5-3. The emission peak maxima were positioned at about 400 nm, with a small shoulder at 475 nm. The XRD scans for each powder again contained peaks from both SrS and SrTe with the (200) and (220) peaks being dominant for both. High resolution scans of the SrS (200) and the SrTe (220) peaks were again collected to determine if there were any detectable shifts in the XRD peaks from the fired powder mixtures relative to pure SrS and SrTe. Table 5-3 summarizes the high resolution XRD results which demonstrated even smaller shifts in the SrS and SrTe peaks.

The temperature dependent PL emission spectra for sample 2A (initial SrTe concentration of 5 wt.%) and 2B (initial SrTe concentration of 15 wt.%) are shown in figure 5-4 and 5-5, respectively. 275 nm excitation was used for powder 2A, and 325 nm excitation was used for powder 2B. The half width at half max (H) versus temperature for the powders 2A and 2B are shown in figure 5-6 and 5-7, respectively. Furthermore, the peak intensity versus temperature for powders 2A and 2B are shown in figure 5-8 and 5-9, respectively.

The 10K and 300K PL emission spectra for a SrS:Te thin film are shown in figure 5-10, which confirmed that Te was successfully incorporated in the SrS. The Te concentration for this film, as measured by RBS, was approximately $4.1\text{x}10^{19}$ cm^{-3}.

Standard EL devices were fabricated and tested under EL excitation however, no luminescence was observed.

Discussion

The original objective of this study was to synthesize SrS_xTe_{1-x}:Ce (1.0 mol.%) powders to investigate crystal field and ligand field effects of the Ce^{+3} 5d-4f radiative transition. Initially the two room temperature emission peaks at 390 nm and 475 nm were thought to be due to the Ce^{+3} radiative transition (5d-$4f_{5/2}$ and 5d-$4f_{7/2}$). However, the energy separation between the two peaks (0.61 eV) is more than twice the characteristic spin-orbital splitting (0.25 eV) of the Ce^{+3} 4f level. In addition, the XRD results suggested that the concentration of Te incorporated in the SrS was $< 10^{20}$ cm^{-3}, which is too low to account for the significant shift in observed in the emission spectra. Electron paramagnetic resonance (EPR) data also showed that the concentration of Ce^{+3} centers was below 0.01 mol%, probably due to most of the Ce being oxidized to form $Ce^{(+4)}O_2^{(-2)}$ during the 4 hour anneal. The diamagnetic Ce^{+4} state is EPR inactive because there are no unpaired electrons, and optically inactive because there are no electrons in the 4f level to excite into the 5d level. To verify that the emission peaks were not from Ce, the second set of SrS-SrTe powders were synthesized without the addition of CeF_3. The PL spectra from these powders were similar to the Ce-doped powders, which confirmed that Ce^{+3} was not responsible for the luminescence.

To determine the processes responsible for the SrS:Te,Ce emission, temperature dependent PL measurements were collected for two of the SrS:Te,Ce powders (1A and

1B). By comparing the temperature versus intensity plots in figure 5-2 to plots reported for ZnS:Te [ROE 73], similar trends in the emission spectra were observed. Both high energy peaks quenched at approximately 200K, the intensity fluctuations as a function of temperature were similar, and for higher Te concentrations, the high energy peak did not exist for either system. Following the mechanism proposed for the ZnS:Te system, the two emission bands at 360 and 400 nm observed in the SrS:Te powders were attributed to bound exciton states created when Te substitutes isoelectronically on S lattice sites. Specifically, the 360 nm peak was assigned to excitons bound to single Te_S sites, whereas the 400 nm peak was assigned to excitons bound to Te_S-Te_S pairs. The exact mechanism responsible for the 475 nm emission is not fully understood, however, a defect center is suspected. The basis for assigning these transitions to bound excitons is discussed below.

From figure 5-2, the PL intensity for the high and low Te concentrations did not follow a systematic pattern as a function of temperature. This behavior was attributed to competing non-radiative recombination events which typically decrease luminescence with increasing temperature, and energy transfer mechanisms which can increase luminescence as a function of temperature [BLA 94 p.91]. It was speculated that the single Te_S exciton emission band overlaps the excitation band for the Te_S-Te_S pairs, and similarly, the Te_S-Te_S pair exciton emission peak overlaps the defect center excitation spectra. When one emission band overlaps the excitation band of another, the emitted photon of the higher energy band can be re-absorbed by the lower energy band. In addition, the thermionic emission of bound electrons and holes can quench bands with lower binding energies and can recombine at deeper electron and hole traps. When energy transfer mechanisms occur between emission bands, it is difficult to distinguish between non-radiative recombination mechanisms and energy transfer mechanisms.

To characterize the 360 nm emission, PL emission spectra (excited at 275 nm) for powder 2A were measured as a function of temperature. From the high resolution XRD data, this powder was believed to have a very low Te concentration because of the negligible SrS (200) peak shift. At sufficiently low Te concentrations, Te_S-Te_S pairs should not exist, therefore only the Te_S exciton band and the defect emission band should exist. Figure 5-4 confirmed that the single Te_S exciton band dominated the emission in this powder, and that the Te_S-Te_S band was virtually obsolete. Assuming similar bonding characteristics for Te in SrS versus ZnS or CdS and based on the concentrations necessary to eliminate the Te_S-Te_S band in ZnS:Te and CdS:Te, the Te concentration in the powder was estimated to be ~$5\text{x}10^{18}$ cm^{-3}.

By examining the 10K emission spectra for this powder, the binding energy of the single Te_S bound exciton can be estimated. The bound exciton binding energy (BE_{ex}) is simply expressed by:

$$(5\text{-}1)\quad BE_{ex} = BG - P(0),$$

where BG is the semiconductor band gap, and P(0) is the zero-phonon line. Though the zero-phonon line was not observed even at 10K, its energy position can be estimated as the high energy edge of the emission band. For the 360 nm band, the zero phonon line was approximately 3.76 eV (330 nm) and the SrS band gap is 4.32 eV. Therefore, the single Te_S bound exciton binding energy was approximately 0.56 eV.

Another useful parameter that can be determined from temperature dependent PL measurements is the phonon energy responsible for peak broadening. From the simple configuration coordinate model, the half width at half max (H) as a function of temperature is given by [ROE 70]:

$$(5\text{-}2)\quad H(T)^2 = H(0)^2 \coth\left(\frac{\hbar\omega}{2kT}\right) + \quad ,$$

where $h\omega$ is the phonon energy, k is Boltzman's constant, T is temperature, and A is a parameter used when the Frank-Condon approximation is not valid. Fitting equation 5-2 to the data in figure 5-6 and assuming the Frank-Condon principle applies (A=0), the phonon energy ($h\omega$) responsible for broadening the single $\mathrm{Te_S}$ exciton peak was determined to be 18.2 meV. Figure 5-11 compares the experimental H versus T data to the points generated by the model.

To understand the physical significance of this phonon energy, it was compared to the phonon energies of the host SrS matrix. From reflectivity measurements, Kanekeo et al. [KAN 82] determined that the longitudinal optical (LO) phonon energy and the transverse optical (TO) phonon energy of SrS were 35 and 23 meV, respectively. Assuming the Frank-Condon principle applies for the single $\mathrm{Te_S}$ bound exciton, the phonon energy responsible for the peak broadening (22.2 meV) matched well with that the SrS TO phonon energy. While it was suspected that SrS would control the excited state vibrational energy for low Te concentration powders, the Frohlich interaction suggests that LO phonons usually couple better with excitons than do TO phonons [CHO 79 p.136]. The Frohlich interaction says that while both TO and LO phonons are accompanied by an electric field in ionic materials, that electrons and holes preferentially interact with the longitudinal fields. According to the Frohlich interaction, it was then expected that the single Te_S exciton should couple with the SrS LO phonon energy.

Because the initial vibrational mode conflicted with the Frohlich interaction, the H vs. T results were fit to equation 5-2 with $A \neq 0$ (i.e., Frank-Condon principle does not apply). The best fit of the H vs. T data resulted in a phonon energy of 37.8 meV which was in good agreement with the LO phonon frequency of SrS (35 meV). Figure 5-12 compares the best fit of equation 5-2 with the H vs. T PL data. From these results, it appears that for the Te_S bound exciton the vibrational energy is dominated by the SrS LO phonons, and for this transition the Frank-Condon principle does not apply. Because the Frank-Condon principle does not apply, this implies that there is a significant difference between the ground state and excited state configuration.

From figure 5-8 it is observed that the 360 nm peak was significantly quenched with increasing temperature. To understand this quenching phenomenon, the basic expression for radiative efficiency as a function of temperature $\eta(T)$ is given by [CHO 79 p.132]:

$$(5\text{-}3)\quad \eta(T) = \frac{I}{I(0)} = \frac{W_R}{W_R + W_{NR}}$$

where I is intensity, and W_R and W_{NR} are the radiative and non-radiative recombination rates, respectively. W_{NR} is expressed by the temperature dependent expression:

$$(5\text{-}4)\quad W_{NR}(T) = W(0)\exp\left(\frac{-E}{kT}\right)$$

where W(0) is of the order of the lattice vibrational frequency, E is an activation energy, k is Boltzman's constant and T is temperature. Combining equations 5-3 and 5-4 results in the following expression of intensity (I) as a function of temperature:

$$(5\text{-}5)\quad I(T) = \frac{I(0)}{1+A\exp\left(\frac{-E}{kT}\right)},$$

where A = W(0)/W_R. From these expressions, the non-radiative recombination rate increases with temperature while the radiative recombination rate is temperature insensitive. Subsequently, the radiative efficiency decreases as the temperature increases due to an increase in the non-radiative recombination rate.

Fitting equation 5-5 to the I versus T data in figure 5-8 results in an activation energy of 25.5 meV and an A value of 18.4. A plot of the experimental I vs. T data compared to the theoretical model is shown in figure 5-13. The calculated activation energy was significantly lower than the binding energy (0.56 eV) of the single Te_S bound exciton, so the quenching mechanism was not attributed to thermalization of the bound exciton. Fukushima and Shionoya [FUK 73] and Roessler [ROE 70] observed that the luminescence quenching activation energy was comparable to the bound exciton binding energy in ZnS:Te and CdS:Te, respectively. They postulated a two step mechanism in which the electron is released first and then the hole. Therefore, the thermal quenching activation energy they calculated was associated with the binding energy of the hole. For the SrS:Te system, this mechanism is not plausible because the bound exciton depth was too deep to be responsible for the experimentally determined activation energy.

The mechanism that could be responsible for the 25.5 meV activation energy is the thermal release of the electron from the bound exciton. The released electron could either be recaptured by the same Te_S site or a nearby Te_S site, or conversely it could be trapped by other defects resulting in the non-radiative return to the ground state. If the distance between nearest neighbor Te_S sites was greater than the electron diffusion length, then the thermally released electron would likely recombine non-radiatively before it has a chance to be recaptured by another Te_S site. This process would effectively quench the bound exciton luminescence. If one assumed a perfectly uniform concentration of $5x10^{18}$ cm^{-3} Te atoms, the average distance between nearest neighbor Te_S sites would be 5.8 nm. Because the free electron diffusion coefficient nor the mobility are known for SrS, accurate diffusion lengths for SrS could not be calculated. To estimate a diffusion length for SrS, ZnS parameters (free electron diffusion coefficient and mobility) were used to calculate the free electron diffusion length. At 300 K, the electron diffusion length in ZnS is 3 nm which is significantly shorter than the nearest neighbor distance (10 nm). Because the calculated diffusion length (3 nm) was smaller than the average distance between Te_S sites (5.8 nm), the thermalized electron will likely recombine non-radiatively before it reaches another Te_S site. While more sophisticated calculations are necessary to confirm this model, these rough calculations suggest that that the thermal release of electrons could be responsible for the observed temperature quenching of single Te_S bound excitons.

To characterize the 390 nm peak, attributed to Te_STe_S bound excitons, a 325 nm He-Cd laser was used to measure the temperature dependent emission spectra for the heavier doped (2B) SrS:Te powder. Sample 2B was assumed to have a higher Te concentration because it had the highest initial SrTe concentration of 15 wt.%. While the exact Te concentration was not experimentally determined, comparing the emission spectra of 2B to the ZnS:Te and CdS:Te data suggested a concentration of ~10^{20} cm^{-3}. The 325 nm laser was used because the single Te_S exciton peak has a zero phonon line at approximately 330 nm, therefore, excitation of the single Te_S band at 325 nm is negligible. Consequently, energy transfer from the single Te_S band to the Te_S-Te_S band should be minimized, which would otherwise complicate the interpretation of the temperature dependent PL emission spectra.

By examining the 25K emission spectra for this powder, the binding energy of the Te_S-Te_S bound exciton can also be approximated by using equation 5-1. Though the zero phonon line was not observed at 25K, its energy position was approximated to be 3.44 eV (360 nm) and the SrS band gap is 4.32 eV. The single Te_S bound exciton binding energy is approximately 0.88 eV.

Using expression 5-2, the phonon energy responsible for broadening of the single Te_S-Te_S exciton peak was determined to be 17.0 meV when A=0, and 18.4 meV when A≠0. Figure 5-14 compares the experimental H versus T data to the points generated by the model. Again, when comparing this phonon energy to the LO (35 meV) and TO (23 meV) phonon energies of SrS, the experimentally determined phonon energy was significantly smaller. Because this emission peak comes from Te_S-Te_S pairs, it was suspected a local vibrational mode representative of the SrTe phonon energy could be dominating the vibration of the Te_S-Te_S pairs. While the LO and TO phonon energies of SrTe have not been reported, the SrTe phonon energies can be calculated using data from other alkaline-earth chalcogenide semiconductors. From the central force model, the TO and/or LO phonon frequency (at k=0) is given by [KAN 82]:

$$(5\text{-}6)\quad \omega = \sqrt{2f\left(\frac{M_A+M_B}{M_A M_B}\right)}$$

where ω is the phonon frequency, f is the force constant, and M_A and M_B are the masses of the constituent ions in the semiconductor. The force constant (f) for the alkaline-earth chalcogenide semiconductors can be determined by taking the slope of the plot ω^2 versus $2(M_A + M_B)/M_A M_B$ (figure 5-15 where the phonon frequencies are taken from [KAN 82]). From the linear regression of the data in figure 5-15, the TO and LO force constants for these materials were determined to be 422,914 and 879,757 mol/(g*cm^2), respectively. Using the calculated force constants and the masses of Sr and Te, the TO and LO frequencies for SrTe were calculated to be 127.6 cm^{-1} (15.8 meV) and 184 cm^{-1} (22.8 meV), respectively.

Initially, the experimentally determined vibrational energy of 17.0 meV (when A=0) was also ascribed to the SrTe TO phonon energy, but because of the Frohlich interaction discussed previously, the A=0 restriction was lifted and the model was re-fit to the experimental data. For the condition A≠0, a phonon energy of 18.4 meV was determined which is in reasonable agreement with the calculated SrTe LO phonon energy (22.8 meV). This implies that the Te_S-Te_S pairs are vibrating at a different frequency than the SrS lattice, and the frequency is approximately that of the LO mode of SrTe. Because equation 5-2 satisfies the Frohlich interaction better when A≠0, this again implies that the Frank-Condon principle does not apply for the Te_S-Te_S bound exciton. Therefore, there is a significant difference between configuration of the ground state and excited state of the bound exciton.

The temperature quenching behavior of the Te_S-Te_S excitons, was again modeled by fitting equation 5-5 to the experimental data (figure 5-9) as shown in figure 5-16. An activation energy of 46.1 meV and an A value of 33.5 were determined. As for the lightly doped sample, the calculated activation energy was considerably lower than the binding energy (0.88 eV) of the Te_S-Te_S bound exciton, so the quenching mechanism was not attributed to thermalization of the bound exciton. The preferential thermalization of electrons is proposed as the quenching mechanism.

To determine whether the thermal activation of electrons could again be responsible for the observed temperature quenching, the distance between Te_S-Te_S pairs was again estimated. If a uniform distribution of 10^{20} pairs cm^{-3} is assumed, then the average distance between nearest neighbor Te_S-Te_S pairs is about 2.1 nm. This is slightly smaller than the diffusion length calculated for ZnS above. From this rough calculation, it is difficult to conclude whether or not this mechanism could be responsible for the thermal quenching. Detailed simulations which consider the free electron trajectory, the temperature dependence of the SrS diffusion length, and the influence of the Te_S-Te_S coulombic attraction are necessary to accurately model the mechanism and draw a conclusion.

Because the pre-exponetial term (A) in equation 5-5 is inversely proportional to the radiative recombination rate, the ratio of $A(Te_S\text{-}Te_S)/A(Te_S)$ can be used to predict the relative radiative recombination rate of the Te_S and Te_S-Te_S bound excitons. If one assumes W(0) is a constant then,

$$(5\text{-}7)\quad A(Te_S - Te_S)/A(Te_S) = W_R(Te_S)/W_R(Te_S - Te_S) \simeq 1.8\ ,$$

which suggests that the Te_S radiative recombination rate is approximately 1.8 times greater than that of the Te_S-Te_S bound exciton. To confirm whether this model accurately predicted the relative radiative recombination rates of the two bound excitons, this ratio was compared to the ratio of the decay lifetimes (τ) of the two emission bands. Figure 5-17 shows the decay curves for the 360 (Te_S) and 400 nm (Te_S-Te_S) peaks. The decay constants (taken at 1/e) were determined to be 0.6 (Te_S) and 0.9 μs (Te_S-Te_S), respectively. The ratio of these decay lifetimes indicate that the Te_S bound exciton radiative recombination rates is 1.5 times greater than the Te_S-Te_S bound excitons, which is in excellent agreement with the model predictions.

One final point should be mentioned about the temperature dependence of the emission spectra for higher Te concentrations. Data in figure 5-5 for the 475 nm emission band shows the peak at 475 gradually increased until 190K and then slowly decreases again. This temperature dependent behavior suggests that energy transfer from the Te_S-Te_S exciton to the 475 nm defect could be occurring. While there are several different energy transfer mechanisms possible (Auger processes, photon absorption, electron transfer [GOD 94]) this behavior is consistent with the capture of released electrons from the Te_S-Te_S pairs.

The 10K and 300K PL spectra of the MBE grown SrS:Te film in figure 5-10 show that both the 360 nm peak (Te_S) and 400 nm peak (Te_S-Te_S) exists at 10K and the 400 nm peak is dominant at 300K. According to ZnS:Te literature data, the Te concentration should be between $5\text{x}10^{18}$ and 10^{20} cm^{-3} (i.e. ~ $5\text{x}10^{19}$ cm^{-3}) since the two peak intensities were about equal at low temperature. From RBS measurements, the Te concentration was determined to be ~$1.1\text{x}10^{-3}$ atomic % (~$4.1\text{x}10^{19}$ cm^{-3}), which was consistent with the

ZnS:Te concentrations. While the goal of investigating this phosphor material was to develop a bright blue EL phosphor, the SrS:Te did not emit under EL excitation. It is believed that the Te bound excitons are ionized by the high electric fields which is a process referred to as field quenching.

Summary

SrS:Te phosphor powders were synthesized, and their luminescent properties were investigated. At low temperature, three high energy emission bands with peak energies of 360, 400 and 475 nm were identified. The 360 nm band was attributed to single Te_S bound excitons, the 400 nm band was attributed to Te_S-Te_S bound excitons, and the 475 nm band was tentatively attributed to a defect in the SrS lattice. By estimating the zero-phonon line of the bound exciton peaks, the binding energies for the Te_S and the Te_S-Te_S were calculated to be 0.56 and 0.88 eV, respectively. Using a simple configuration coordinate model, the Te_S phonon energy was calculated to be 37.8 meV. This value was in excellent agreement with the LO phonon energy of SrS, which suggests that the excited state is coupled with the host lattice. Similarly, the Te_S-Te_S phonon energy was calculated to be 18.4 meV which was in excellent agreement with the calculated LO phonon energy of SrTe.

The temperature quenching of the exciton emission was investigated, and the data were found to fit well with a common temperature quenching mechanism. The model used assumes that the radiative recombination rate is insensitive to temperature, however the competing non-radiative recombination rate increases exponentially with increasing temperature. Non-radiative recombination activation energies of 25.5 and 46.1 meV were calculated for the Te_S and Te_S-Te_S excitons, respectively, which was interpreted to be the binding energy of the trapped electrons. The pre-exponential term in expression 5-5 that was used to model the temperature quenching behavior is inversely proportional to the radiative recombination rate. Thus, it was predicted that the Te_S bound exciton (A=18.4) should decay approximately 1.8 times faster than the Te_S-Te_S bound exciton (A=33.5). From the radiative decay lifetimes, the radiative recombination rate of Te_S bound exciton (τ=0.6 μs) was found to be approximately 1.5 times faster than the Te_S-Te_S bound exciton (τ=0.9 μs) which is in excellent agreement with the predicted value.

Table 5-1. Summary of High Resolution XRD Results from SrS:Te,Ce Powders

Material	SrS (200) Intensity	SrS (200) Peak Position	SrTe (220) Intensity	SrTe (220) Peak Position	SrTe/SrS Intensity (%)
SrS	-	29.686	-	-	-
SrTe 5%	65,536	29.68	92	38.18	0.14
SrTe 10%	45,668	29.6925	225	38.34	0.49
SrTe 15%	44,690	29.675	350	38.32	0.78
SrTe 20%	29,481	29.64	454	38.325	1.54

Table 5-2. CL Efficiency Data for SrS:Te,Ce Powders

Voltage	Efficiency(lum/W) SrTe 5%	Efficiency(lum/W) SrTe 10%	Efficiency(lum/W) SrTe 15%
500	0	0	0
600	0	0	0
700	0	0	0
800	0	0	0
900	0	0	0
1,000	0.02	0.002	0.005
2,000	0.092	0.014	0.018
3,000	0.123	0.025	0.03
4,000	0.195	0.035	0.035

Table 5-3. Summary of High Resolution XRD Results from SrS:Te Powders

Material	SrS (200) Intensity	SrS (200) Peak Position	SrTe (220) Intensity	SrTe (220) Peak Position	SrTe/SrS Intensity (%)
SrS	-	29.686	-	-	-
SrTe 5%	40,080	29.6825	841	37.8075	2.09
SrTe 10%	48,620	29.6775	882	37.855	1.81
SrTe 15%	37,090	29.677	1,221	37.86	3.29

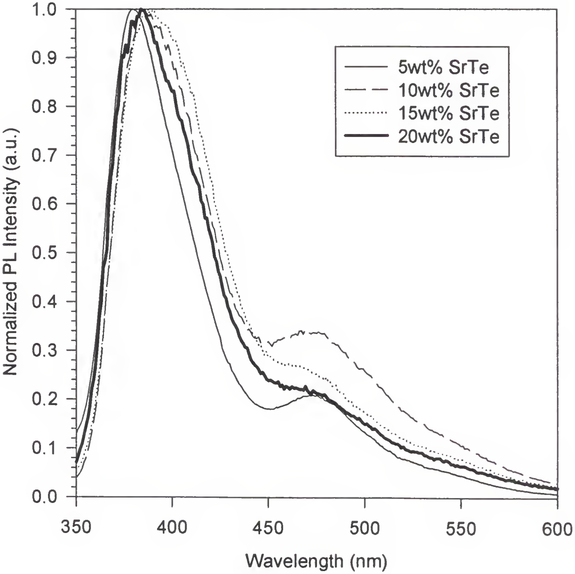

Figure 5-1. Normalized PL spectra for SrS:Te,Ce powders where SrTe additions were 5,10, 15, and 20 wt%, and CeF_3 additions were 1mol%.

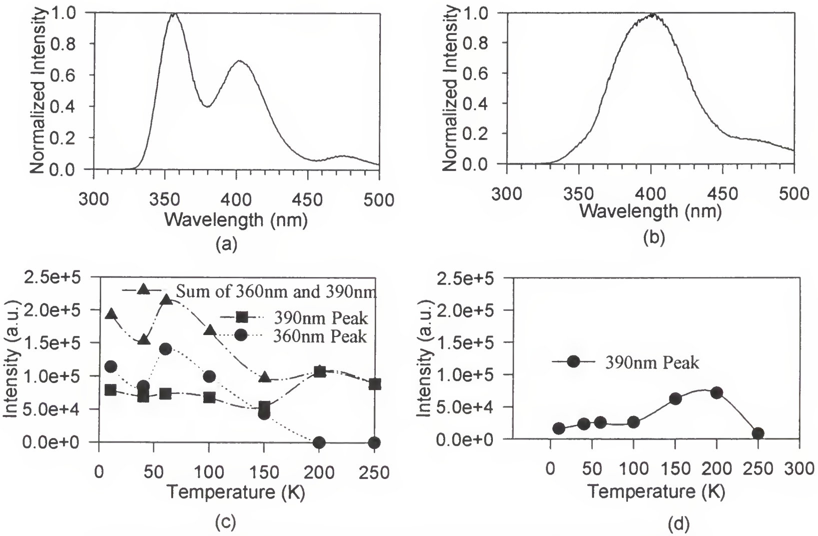

Figure 5-2. 25K emission spectra for powder 1A (a) and 1B (b), and their corresponding peak intensity as a function of temperature (c) and (d), respectively.

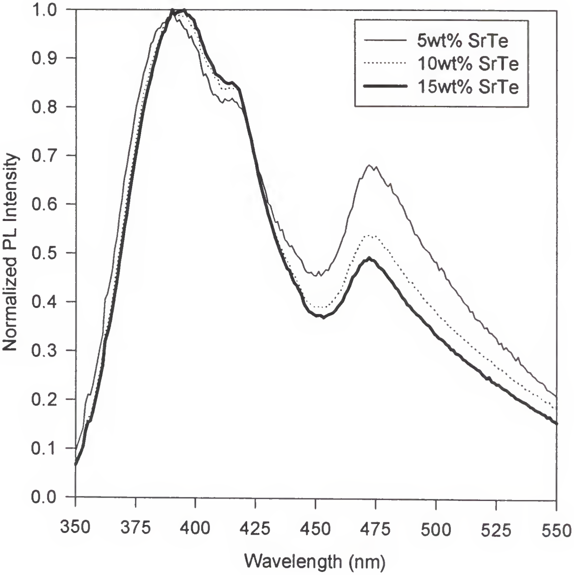

Figure 5-3. Normalized PL spectra for SrS:Te powders where SrTe additions were 5,10, and 15 wt%.

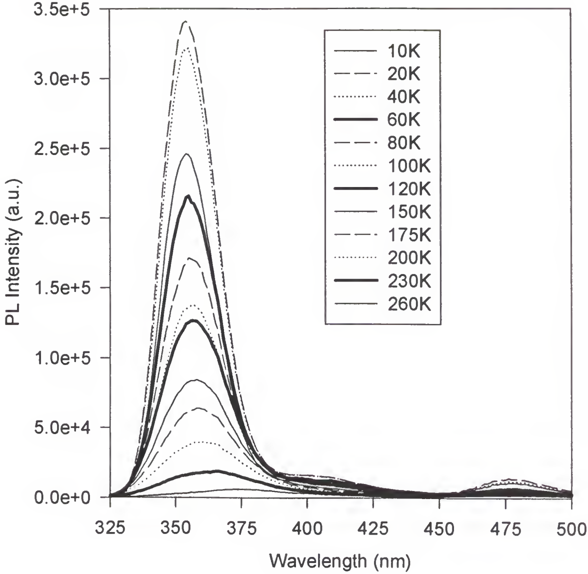

Figure 5-4. PL emission spectra as a function of temperature for powder 2A (SrTe addition 5wt%).

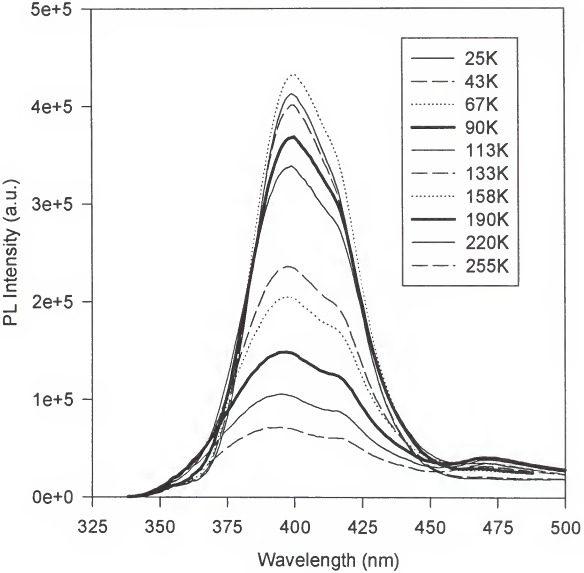

Figure 5-5. PL emission spectra as a function of temperature for powder 2B (SrTe addition 15wt%).

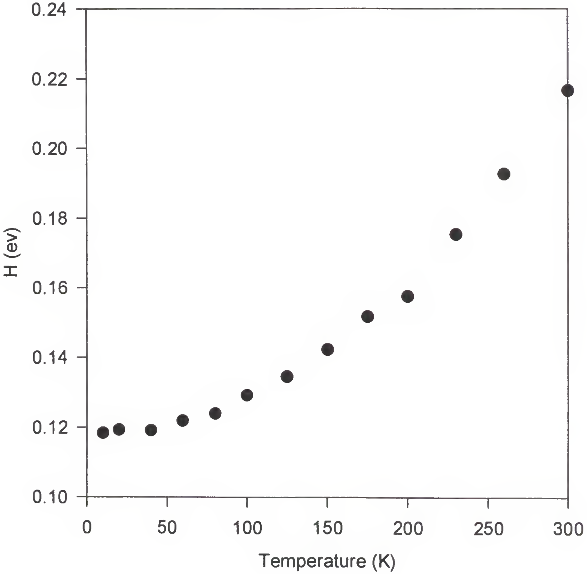

Figure 5-6. Half width at half max (H) verses temperature for powder 2A.

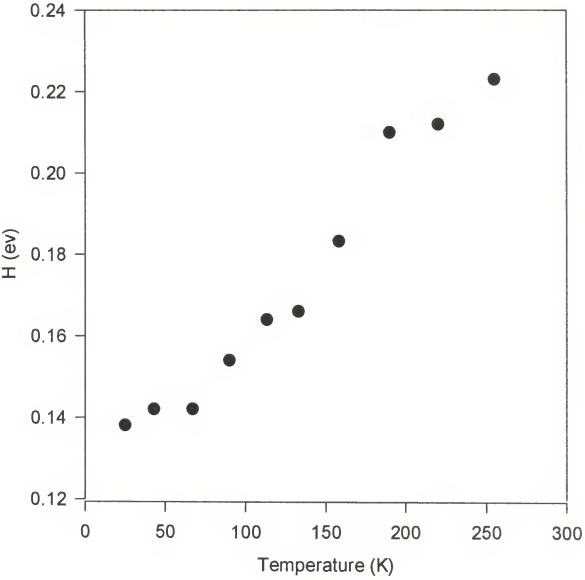

Figure 5-7. Half width at half max (H) verses temperature for powder 2B.

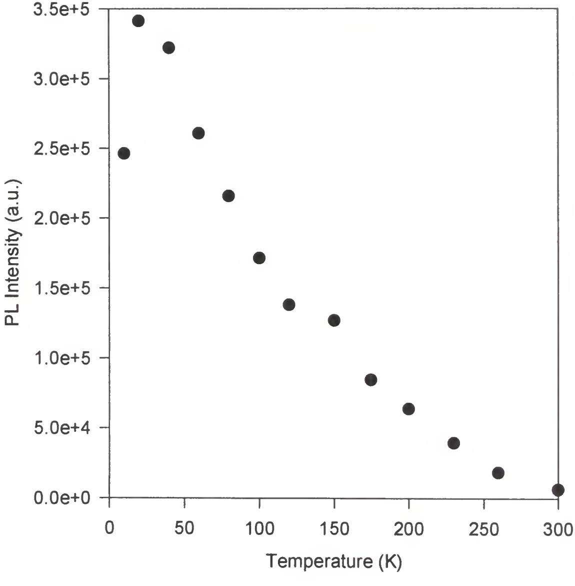

Figure 5-8. PL intensity versus Temperature for powder 2A.

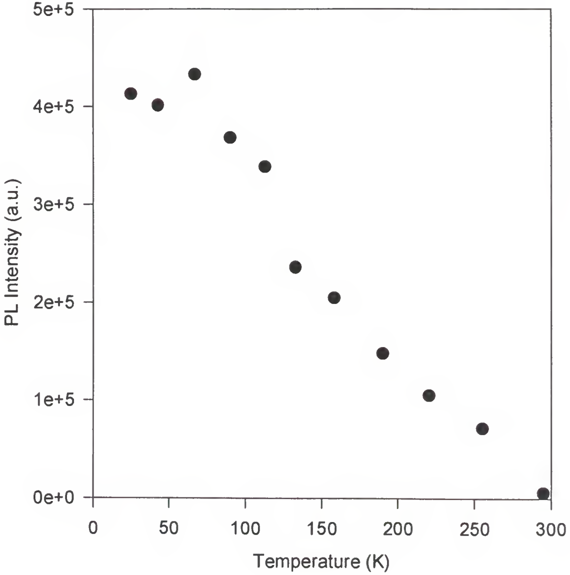

Figure 5-9. PL intensity versus Temperature for powder 2B.

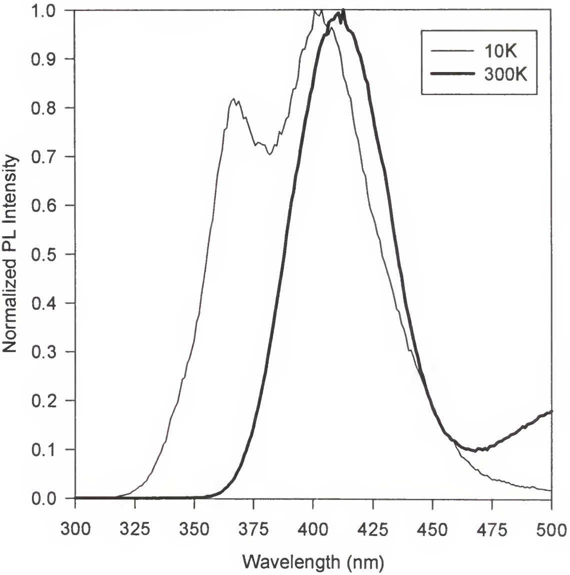

Figure 5-10. 10K and 300K PL emission spectra for a SrS:Te thin film.

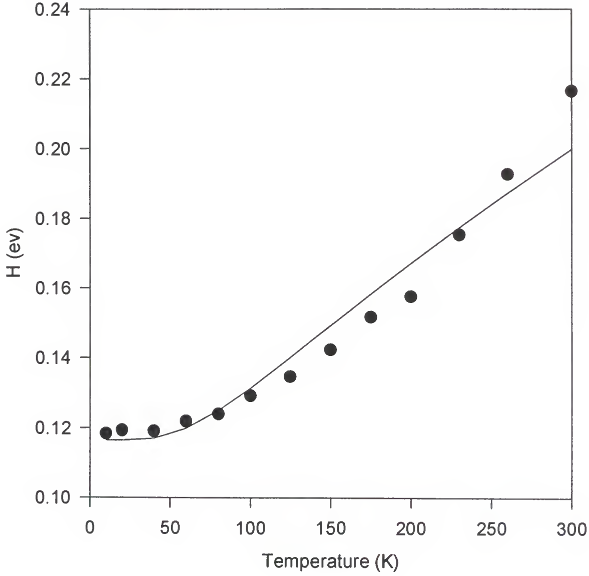

Figure 5-11. Experimental half width at half max (H) versus temperature and best fit of equation 4-2 (A=0) for powder 2A.

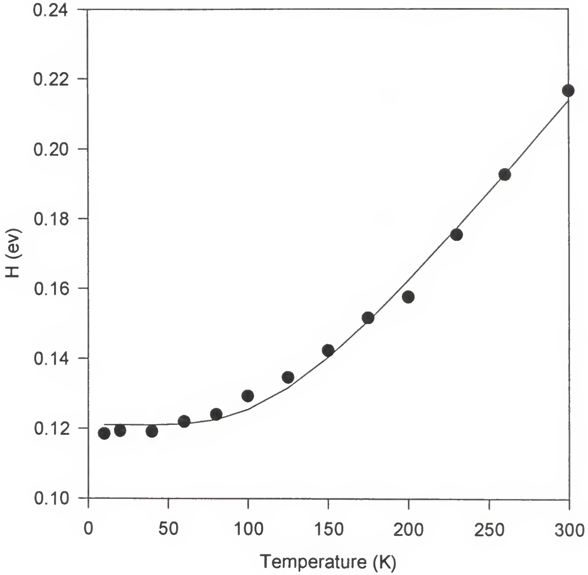

Figure 5-12. Experimental half width at half max (H) verses temperature and best fit of equation 4-2 ($A\neq0$) for powder 2A.

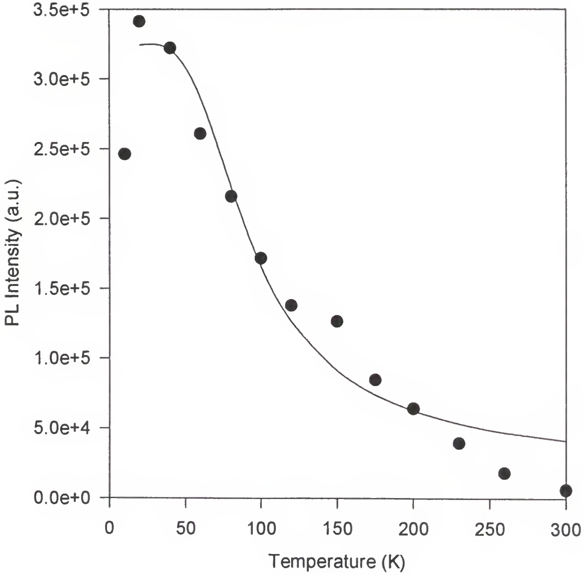

Figure 5-13. Experimental PL intensity verses temperature and best fit of equation 4-5 for powder 2A.

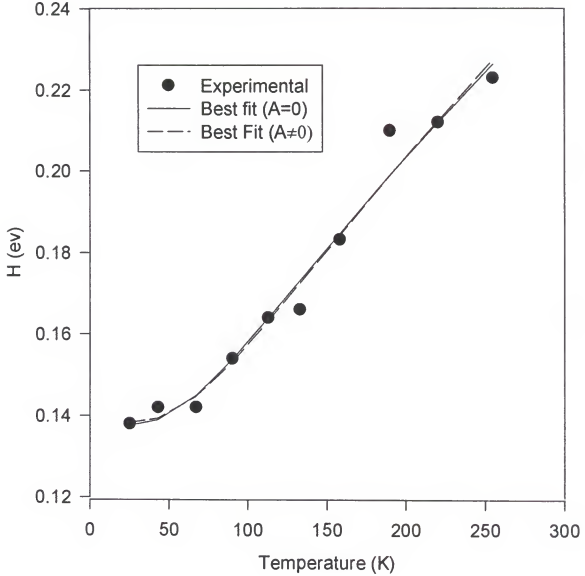

Figure 5-14. Experimental half width at half max (H) verses temperature and best fit of equation 4-2 (A=0 and A≠0) for powder 2B.

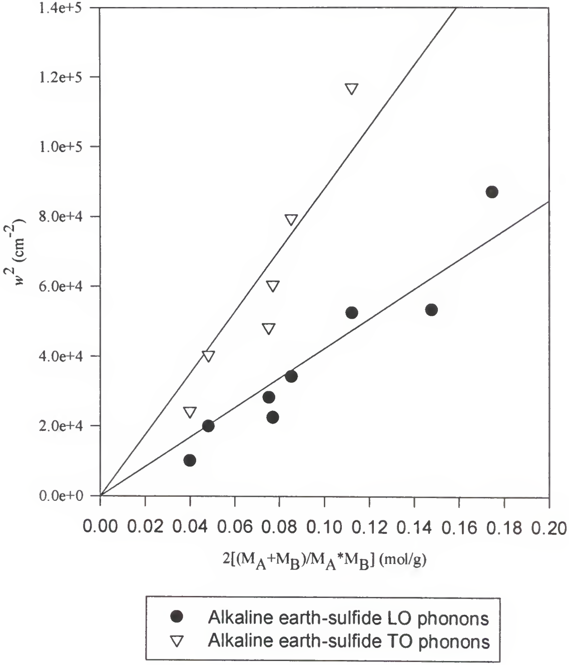

Figure 5-15. Plot of phonon frequency w^2 versus 2[(M$_A$+M$_B$)/M$_A$+M$_B$] for several alkaline earth sulfides [KAN 82]. The slope of the linear regressions is equal to the force constant (*f*) in equation 5-6.

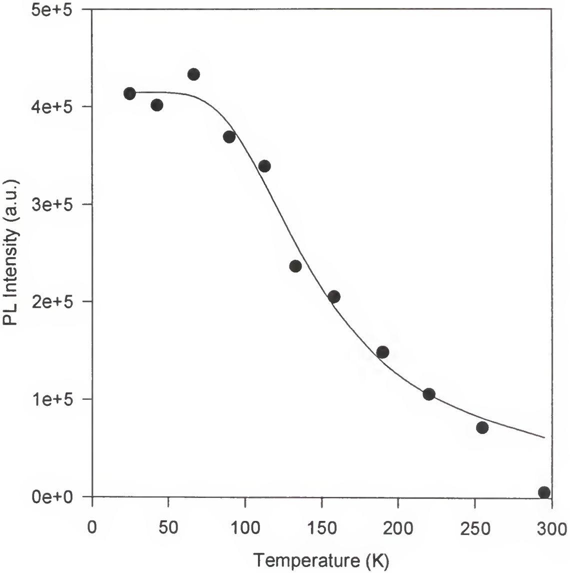

Figure 5-16. Experimental PL intensity verses temperature and the best fit of equation 4-5 for powder 2B.

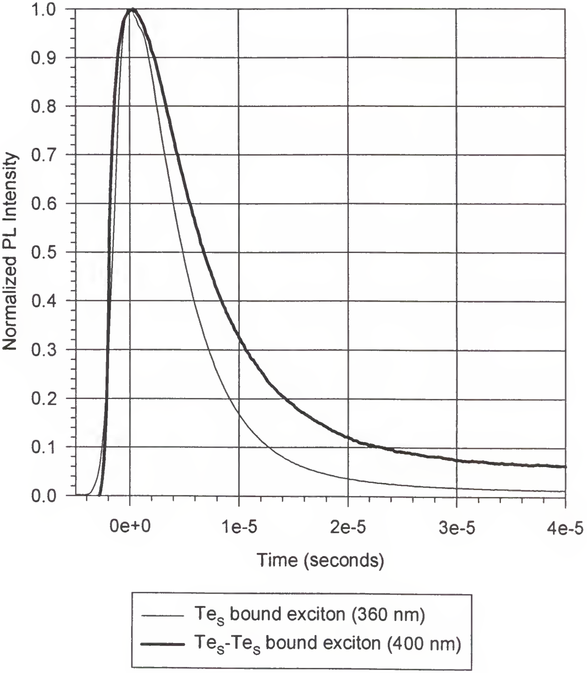

Figure 5-17. Luminescence decay plot of Te$_S$ (360 nm) and Te$_S$-Te$_S$ (400 nm) bound excitons

CHAPTER 6

CONCLUSIONS

The Effects of Oxygen Doping $Ca_{0.55}Sr_{0.45}Ga_2S_4$:Ce Thin Films

When the $Ca_{0.55}Sr_{0.45}Ga_2S_4$:Ce thin films were oxygen doped the luminance and efficiency increased, and the emission spectra shifted to higher energy (blue shift). Thermodynamic calculations showed that the Ce-O bond is favored over Ce-S or Ca-O and Sr-O, which suggested that oxygen ions may preferentially replace sulfur ions bonded to Ce. XPS analysis was performed to understand the local chemistry of the Ce^{+3} ion in the undoped and oxygen doped thin films. The 3 eV difference (282 versus 285 eV for undoped and oxygen doped $Ca_{0.55}Sr_{0.45}Ga_2S_4$:Ce thin films, respectively) in the Auger parameter indicated that there was a change in the local Ce^{+3}, however the complicated bonding characteristics of the rare earth ions made it difficult to interpret these results.

Detailed analysis of the core level Ce 3d XPS peaks showed that the small shoulders on the low binding energy side of the ground state peaks increased when oxygen was introduced into the $Ca_{0.55}Sr_{0.45}Ga_2S_4$:Ce thin films. To confirm that these changes were not associated with a change in the oxidation state of the Ce (i.e. +3 to +4), XPS spectra were taken on an oxidized Ce foil. The spectrum taken after a 10 minute sputter clean was found to be CeO_2 (Ce^{+4}), and the spectrum taken after a 60 minute sputter clean was found to be Ce_2O_3 (Ce^{+3}). By comparing these XPS spectra to the undoped and oxygen doped $Ca_{0.55}Sr_{0.45}Ga_2S_4$:Ce spectra, it was concluded that the Ce oxidation state did not change in the oxygen doped $Ca_{0.55}Sr_{0.45}Ga_2S_4$:Ce thin films. The small low binding energy shoulders were determined to be charge transfer peaks, and the increased intensity of these peaks was correlated to oxygen ions replacing three of the eight sulfur ligands bonded to the Ce luminescent center. As oxygen ions replaced sulfur ligands, the Ce-ligand bond became more ionic and the electron cloud density around the Ce decreased. This caused the ligand-to-metal charge transfer probability to increase because the screening effect of the electron cloud was reduced.

Semiempirical cluster calculations of Ce bonded to S and O showed that the Ce^{+3} radiative transition energy systematically increased as sulfur ligands were replaced with oxygen ligands. Specifically, an oxygen to sulfur ratio of 0.5 increased the radiative transition energy 1147 cm^{-1}. This was in good agreement with the estimated oxygen to sulfur ratio of 0.6 in the oxygen doped $Ca_{0.55}Sr_{0.45}Ga_2S_4$:Ce thin films whose transition energy was observed to increase 733 cm^{-1}.

Emission Spectra Changes in Ce Doped Alkaline Earth (Mg, Ca, Sr AND Ba) Sulfide Phosphors

The reported Ce^{+3} 4f-5d radiative transition energies in MgS, CaS, and SrS were accurately modeled with crystal molecular orbital and crystal field calculations. The molecular orbital calculations were performed using the configuration interaction spectroscopic version of the intermediate neglect of differential overlap (INDO/S-CI) model. The Ce^{+3} parameters were initially tested by calculating the 4f and 5d energy levels of the free ion which, in an field free environment, only split due to spin orbital coupling.

The calculated 4f and 5d spin orbital levels of the Ce^{+3} free ion were found to be in excellent agreement with the experimental gas phase analysis.

To calculate the Ce^{+3} 4f and 5d energy levels in an AES host lattice, a thirteen ion cluster surrounded by a 15x15x15 array of +2 and -2 point charges was generated (details of cluster geometry given in chapter 3). The calculated Ce^{+3} energy levels were found to be in excellent agreement with the experimentally reported energy levels. Furthermore, two trends were observed in the experimentally determined 4f and 5d energy levels: as the AE size increased from Mg to Ca to Sr, 1) the 5d levels occur at higher energies relative to the 4f levels, and 2) the spin orbital splitting of the 4f and 5d levels decreased. Both of these trends were also observed in the calculated results.

The crystal field calculations for Ce^{+3} in the different AES host lattices assumed a point charge model. This model calculates the change in the 5d levels as a function of the Ce^{+3}-S bond distance and was found to accurately model the difference between the CaS:Ce and SrS:Ce transition energies. These calculations however, were found to over estimate the difference between MgS:Ce and CaS:Ce. It was concluded that the Ce-S bond distance was modified in the MgS to account for local lattice distortions caused by the severe size mismatch between Ce^{+3} and Mg^{+2}. A simple model was developed to account for a local lattice expansion at the Ce^{+3} luminescent center, and subsequent crystal field calculations were made. The crystal field calculations using the modified bond distances were in good agreement with the experimental data, which supported the explanation that the MgS lattice locally expands to accommodate the Ce^{+3}.

After modeling the reported literature data, the crystal field calculations were extended to $Sr_xBa_{1-x}S$:Ce to predict the change in the transition energy. Using the expression used to modify the MgS:Ce bond distance, it was predicted that BaS:Ce would blue shift approximately 513 cm^{-1} relative to SrS:Ce. SrS:Ce/BaS:Ce thin films were grown and XRD results suggested that SrS and BaS were soluble over the composition range that was investigated (0% < BaS% < 50.2%) . The emission spectrum was found to blue shift slightly at low BaS concentrations (< 20%), and then red shift at higher BaS concentrations (> 20%), which was contrary to the crystal field calculations. From these results, it was concluded that a local change in Ce^{+3} symmetry was occuring at higher BaS concentrations. A tetragonal distortion (C_{3v}) of the octahedral symmetry (O_h) was proposed.

SrS:Te Bound Excitons

SrS:Te powders were synthesized and found to have two high energy emission bands with peak wavelengths at 360 and 400 nm. The 360 nm emission band dominated at lower Te concentrations and was attributed to Te_S bound excitons. The 400 nm emission band dominated at higher concentrations and was attributed to Te_S-Te_S bound excitons. The zero-phonon lines of the Te_S and Te_S-Te_S excitons were estimated to be 3.76 eV and 3.44 eV, respectively, and from these lines the bound exciton binding energies were determined to be 0.56 (Te_S) and 0.88 eV (Te_S-Te_S).

To investigate the bound exciton emission process more extensively, PL emission spectra were taken as a function of temperature. Using a simple configuration coordinate model, the phonon energies associated with the peak broadening for each emission band was determined. The phonon energy calculated for the Te_S emission band was 37.8 meV, which was in excellent agreement with the SrS LO phonon energy (35 meV). This suggests that the Te_S site is coupled strongly to the vibrational energy of the SrS lattice. The calculated Te_S-Te_S phonon energy was 18.4 meV which was close to the SrTe LO phonon energy (22.8 meV -- calculated using the central force model for diatomic molecules). This suggests that the Te_S-Te_S site has a local vibrational mode which is independent of the host lattice.

From the PL intensity versus temperature data, the thermal quenching activation energy for the Te_S and Te_S-Te_S bound excitons were determined to be 25.5 and 46.1 meV, respectively. Because these activation energies were significantly lower than the binding energy of the two bound excitons, this activation energy was ascribed to the binding energy of the electrons. From the expression that describes the intensity versus temperature, it was found predicted that the Te_S bound excitons were 1.8 times faster (more efficient) than the Te_S-Te_S bound excitons. Luminescence decay measurements were performed to compare the radiative rates of each bound exciton and the Te_S bound exciton was found to be 1.5 times faster (more efficient) than the Te_S-Te_S bound exciton.
SrS:Te thin films were deposited on silicon and glass EL device substrates. The SrS:Te thin films deposited on silicon were tested under PL excitation and both the 360 and 400 nm emission bands were observed at 10K. Previous work on other metal sulfide systems doped with tellurium suggested a concentration range of ~ $5x10^{19}$ cm^{-3} was necessary to observe both emission bands. To confirm that this concentration range was consistent in the SrS:Te system, RBS measurements were made which indicated that the concentration was $4.1x10^{19}$ cm^{-3}. The thin film samples grown on glass EL device substrates were

fabricated into full ACTFEL devices, however no luminescence was observed under EL excitation.

CHAPTER 7

FUTURE WORK

The Effects of Oxygen Doping $Ca_{0.55}Sr_{0.45}Ga_2S_4$:Ce Thin Films

In chapter three, the effects of oxygen doping $Ca_{0.55}Sr_{0.45}Ga_2S_4$:Ce thin films were investigated, and from the XPS results it was concluded that oxygen ions were replacing three of the eight sulfur ligands bonded to Ce. To confirm this quantitative analysis, the following critical experiment is proposed. Initially a Ce_2S_3 film would be grown in a cluster tool where the sample could then be analyzed by XPS without exposure to air. This would prevent or minimize any physisorbed or chemisorbed oxygen to bond to the surface so a true Ce_2S_3 XPS spectra would be obtained. A high resolution scan of the Ce 3d and Ce MNN Auger region would be taken, as well as the low binding energy valence band region (Ce 4f and S 3p). After the initial Ce_2S_3 spectrum was taken, then the thin film would be exposed briefly to an oxidizing ambient (i.e., hydrogen plasma with a small amount of oxygen), and then analyzed again by XPS. This procedure would be repeated several times until the XPS sensitive region of the film (~ 5 nm) was completely oxidized.

The core level 3d spectra would show conclusively the evolution of the Ce^{+3} charge transfer peaks as oxygen ligands gradually replace sulfur ligands and form more ionic bonds. In addition, one could monitor the difference between the ground state peak and the charge transfer state peak and correlate this to the valence band data. Careful examination of the valence band spectra would reveal changes in the Ce^{+3} 4f binding energy which was determined to control the position of the charge transfer state peak. Finally, from the Ce MNN Auger spectra, the Auger parameter could be plotted as a function of the $Ce_2S_{3-x}O_x$ composition so the bonding properties of the Ce^{+3} could be better understood.

Emission Spectra Changes in Ce Doped Alkaline Earth (Mg, Ca, Sr AND Ba) Sulfide Phosphors

In chapter four, it was suggested that the mechanism responsible for the observed red shift in the $Sr_xBa_{1-x}S$:Ce thin films was a change in the local symmetry of the Ce^{+3} ion. In particular, it was proposed that the Ce^{+3} symmetry changed from O_h to C_{4v} which results from a tetragonal distortion. To confirm this distortion, EPR measurements would be performed on thin film or powder $Sr_xBa_{1-x}S$:Ce samples, because the EPR signal is known to be sensitive to the symmetry of the paramagnetic center.

In addition, the energy level positions of the BaS:Ce could be modeled by the molecular orbital cluster calculations if the semiempirical Ba parameters were calculated. This would allow one to calculate the energy levels of the Ce^{+3} ion in the undistorted O_h BaS lattice and also on different clusters with various tetragonal (C_{4v}) or trigonal (C_{3v}) distortions. The calculated energy levels would then be compared to the experimentally observed energy levels to understand the specific symmetry of the Ce^{+3} ion.

SrS:Te Bound Excitons

Though the objective of synthesizing the SrS:Te powders and films was to produce a bright blue EL phosphor, the thin films did not luminesce under EL excitation. The bound excitons are believed to be field quenched in SrS:Te, however it is not clear whether the Te_S or Te_S-Te_S bound excitons can sensitize the SrS:Ce^{+3} EL phosphor. Sensitization of SrS:Ce may be possible because space charge generated in the SrS:Ce layer induces a high field and a low field region. Therefore, efficient bound exciton recombination is possible in the low field region. Because there is reasonable overlap between the emission band of the Te_S-Te_S bound exciton and the absorption band of the Ce^{+3}, efficient sensitization is possible.

To investigate this process, SrS:Ce,Te thin films would be grown with various Ce ($0 < $ Ce mol% < 1.0) and Te ($0 <$ Te mol% < 1.0) concentrations. For comparison, SrS:Ce thin films with similar Ce concentrations would be grown, and the EL performance of each SrS:Ce and SrS:Ce,Te thin films would be tested. To investigate the details of the field quenching mechanism, PL measurements of the thin films would be measured with under the influence of an external voltage. The photo-excited luminescence would be measured as a function of the external voltage and the quenching behavior would be considered using basic field ionization (tunneling) theory.

REFERENCES

[ALT 84] P. M. Alt, SID Digest, (1984), pp. 79.

[ASA 80] S. Asano, N. Yamashita, T. Ohnishi, Physica Status Solidi (b) 99, 661 (1980).

[ASA 83] S. Asano, N. Yamashita, Y. Ogawa, Physica Status Solidi (b) 118, 89 (1983).

[ASK 94] D. R. Askeland, The Science and Engineering of Materials (PWS Publishing, Boston 1994).

[ATE 68] A. C. Aten, J. H. Haanstra, H. D. Vries, Phillips Research (1968).

[BAI 95] P. Bailey, D. Karkner, X. Wu, SID Digest, (1995), pp. 484.

[BAR 47] J. Bardeen, Physical Review 71, 717 (1947).

[BAR 84] W. A. Barow, R. E. Coovert, C. N. King, SID Digest, (1984), pp. 249.

[BAR 93] W. A. Barrow, R. C. Coovert, E. Dickey, C. N. King, C. Laakso, S.-S. Sun, R. T. Tuenge, SID Digest, (1993), pp. 761.

[BHA 93] K. Bhattacharyya, S. M. Goodnick, J. F. Wager, Journal of Applied Physics 73, 3390 (1993).

[BLA 94] G. Blasse, B. C. Grabmaier, Luminescent Materials (Springer-Verlag, Berlin-Heidelberg, 1994).

[BRE 88] K. Brennan, Journal of Applied Physics 64, 4024 (1988).

[BRI 90] E. Bringuier, Journal of Applied Physics 67, 7040 (1990).

[BRI 91] E. Bringuier, Journal of Applied Physics 70, 4505 (1991).

[BRI 94] E. Bringuier, Journal of Applied Physics 75, 4291 (1994).

[BRI 92] J. D. Britton, J. C. McClure, V. P. Singh, EL 92, (1992), pp. 286.

[CAS 92] J. A. Castellano, Handbook of Display Technology (Hartcourt Brace Jovanovich, New York, 1992).

[CHO 93] K. L. Chopra, S. Major, D. K. Pandya, Thin Solid Films 102, 1 (1983).

[COO 82] R. E. Coovert, C. N. King, R. T. Tuenge, SID Digest, (1982), pp. 128.

[CUL 87] J. C. Culberson, P. Knappe, N. Rosch, M. C. Zerner, Theoretical Chemistry Acta 71, 21 (1987).

[CUT 68] J. D. Cuthbert, D. G. Thomas, Journal of Applied Physics 39, (1968).

[DEA 79] P. J. Dean, D. C. Herbert, in Excitons K. Cho, Eds. (Springer-Verlag, Berlin-Heidelberg ,1979).

[DES 36] G. Destriau, Journal de Chem. Phys. et Physico-Chemie Boil. 33, 620 (1936).

[DUF 90] J. A. Duffy, Bonding, Energy Levels and Bands in Inorganic Solids (John Wiley and Sons Inc., New York, 1990).

[FUK 73] T. Fukushima, S. Shionoya, Japanese Journal of Applied Physics 12, 549 (1973).

[GER 73] Geroch, R. C. Slade, Ligand-Field Parameters (Cambridge University Press, London, 1973).

[GOD 94] M. Godlewski, M. Leskela, Critical Review in Solid State Material Science 19, 199 (1994).

[GUD 29] H. Guden, R. W. Pohl, Z. F. Physik 2, 192 (1929).

[HOL 96] P. H. Holloway, S. Jones, P. Rack, J. Sebastian, T. Trottier, Tenth International Symposium on the Applications of Ferroelectrics, (1996), (submitted 9/96).

[HOW 77] W. E. Howard, IEEE Transactions on Electronic Devices 24, 903 (1977).

[INO 74] T. Inoguchi, M. Takeda, Y. Kakihara, M. Yoshida, SID Digest, (1974), pp. 86.

[INO 94] Y. Inoue, K. Tanaka, S. O. Kumoto, K. Kobayashi, SID Digest, (1994), pp. 169.

[ISL 70] G. W. Isler, A. J. Strauss, Journal of Luminescence 3, 1 (1970).

[KAN 82] K. Kaneko, K. Morimoto, T. Koda, Journal of the Physics Society of Japan 51, 2247 (1982).

[KEL 96] P. A. Keller, Information Display 12, 36 (1996).

[KHO 94] R. Khormaei, S. Thayer, K. Ping, C. King, G. Dolney, A. Ipri, F-L. Hsueh, R. Stewart, T. Keyser, G. Becker, D. Kagey, M. Spitzer, SID Digest, (1994), pp. 137.

[KIN 88] C. N. King, SID Lecture Notes, (1988),

[KIN 96a] C. N. King, EL 96, (1996), pp. 375.

[KIN 96b] C. N. King, Journal of the Society of Information Display 1, 1 (1996).

[KOB 90] H. Kobayashi, T. Tueta, R. Menn, IEEE Transactions on Electronic Devices 29, 1626 (1990).

[KOB 92] S. Kobayashi, J. F. Wager, A. Abu-Dayah, EL 92, (1992), pp. 234.

[KOT 91] M. Kotzian, N. Rosch, M. C. Zerner, International Journal of Quantum Chemistry 25, 545 (1991).

[KUR 69] S. Kurtin, J. C. McGill, C. A. Mead, Physical Review Letters 22, 1433 (1969).

[LEP 93] M. Leppanen, G. Harkonen, A. Pakkala, E. Soininen, R. Tornquist, International Display Research Conference, (1993), pp. 229.

[LEP 91] M. Leppanen, M. Leskela, L. Niinisto, E. Nykanen, P. Soininen, M. Tiita, SID Digest, 282 (1991).

[LIB 71] D. A. Liberman, D. T. Cromer, Computational Physics Communications 2, 107 (1971).

[LID 91] D. R. Lide, Eds., CRC Handbook of Chemistry and Physics (CRC Press Inc., Boston,1991).

[MAC 90] R. Mach, G. O. Muller, Journal of Crystal Growth 101, 967 (1990).

[MAC 91] R. Mach, G. O. Muller, Semiconductor Science and Technology 6, 305 (1991).

[MAN 94] D. Maneval, B. Ray, I. V. F. Viney, J. W. Brightwell, B. W. Arterton, Journal of Crystal Growth 60, 61, 32 (1994).

[MAU 92] R. H. Mauch, K. O. Velthaus, G. Bilger, H. W. Schock, Journal of Crystal Growth 117, 964 (1992).

[MIK 92] A. Mikami, I. Yashima, F. Kajikawa, EL 96, (1996), pp. 369.

[MIT 91] J. Mita, Q. Z. Guo, M. Kobayashi, K. Kawamura, SID Digest, (1991), pp. 290.

[MIY 93] K. Miyashita, M. Shibata, Digest of Japan Display, (1993), pp. 100.

[MOE 63] T. Moeller, The Chemistry of the Lanthanides (Rheinhold Publishing, New York, 1963).

[NAK 93] Y. Nakanishi, T. Ito, H. Tatsuoka, H. Kuwabara, S. Wickramanayaka, Y. Hatanaka, G. Shimaoka, International Display Research Conference, (1993), pp. 475.

[NIR 88] T. Nire, T. Watanabe, N. Tsurumaki, A. Miyakoshi, S. Tanda, SID Digest, (1988), pp. 218.

[NOR 89] F. L. Normand, T. E. Fallah, L. Hilaire, P. Legare, A. Katoni, J. C. Perlebas, Solid State Communications 71, 885 (1989).

[OHM 95] K. Ohmi, K. Fujimoto, S. Tanaka, H. Kobayashi, Journal of Applied Physics 78, 428 (1995).

[OHN 90] H. Ohnishi, T. Okuda, Japanese Journal of Applied Physics, 31 (1990).

[OHW 90] J. Ohwaki, H. Kozawaguchi, B. Tsujiyama, Journal of the Electrochemical Society 137, 340 (1990).

[OKA 89] K. Okamota, T. Yoshini, K. Nakamura, T. Kobayahsi, S. Sato, S. Miara, Japanese Journal of Applied Physics 28, 1378 (1989).

[OKA 93] S. Okamoto, T. Kuki, T. Suzuki, Japanese Journal of Applied Physics 32, 1672 (1993).

[ONO 95] Y. A. Ono, Electroluminescent Displays. H. L. Ong, Eds., Series on Information Display (World Scientific, Singapore,1995), vol. 1.

[PAR 93] K.-H. Park, S.-J. Oh, Physical Review B 48, 14833 (1993).

[PET 72a] T. E. Peters, J. A. Baglio, Journal of the Electrochemical Society 119, 230 (1972).

[PET 72b] T. E. Peters, Journal of Electrochemical Society 119, 1720 (1972).

[POE 93] D. Poelman, R. Vercaemst, R. L. V. Meirhaeghe, W. H. Laflere, F. Cardon, International Display Research Conference, (1993), pp. 483.

[RAC 96] P. D. Rack, A. Naman, P. H. Holloway, S.-S. Sun, R. T. Tuenge, MRS Bulletin 21, 49 (1996).

[ROE 70] D. M. Roessler, Journal of Applied Physics 11, 4589 (1970).

[ROM 93] M. Romeo, K. Bak, J. E. Fallah, F. L. Normand, L. Hilaire, Surface and Interface Analysis 20, 508 (1993).

[RUS 67] M. J. Russ, D. I. Kennedy, Journal of the Electrochemical Society , 1066 (1967).

[SCH 85] W.-D. Schneider, B. Delley, E. Wuilloud, J. M. Imer, Y. Baer, Physical Review B 32, 6819 (1985).

[SHE 84] A. Sher, A. Chen, W. E. Spicer, Thirteenth International Conference on Defects in Semiconductors, L. C. Kimerling, J. M. Parseys, Eds., (1984), pp. 335.

[SMI 95] D. C. Smith, J. A. Samuels, B. F. Espinoza, E. Apen, N. M. Peachey, R. C. Dye, R. T. Tuenge, C. F. Schaus, C. N. King, SID Digest, (1995), pp. 728.

[SOB 79] I. I. Sobelman, Atomic Spectra and Radiative Transitions (Springer-Verlag, Berlin-Heidelberg, 1979).

[SOH 92] S. H. Sohn, D. G. Hyun, M. Noma, S. Hosomi, Y. Hamakawa, Journal of Applied Physics 72, 4877 (1992).

[SOX 72] E. J. Soxman, R. D. Keptchpel, JANAIR, Electroluminescence Thin Film Research Report (1972).

[SUN 94] S.-S. Sun, R. T. Tuenge, J. Kane, M. Ling, Journal of the Electrochemical Society 141, 2877 (1994).

[SZE 81] S. Sze, Physics of Semiconductor Devices (J. Wiley and Sons, New York, 1981).

[TAN 85] S. Tanaka, V. Shanker, M. SIIKI, H. Deguchi, H. Kobayashi, SID Digest, (1985), pp. 218.

[TAN 85] S. Tanaka, H. Deguchi, Y. Mikami, M. Shiki, H. Kobayashi, SID Digest, (1989), pp. 279.

[TAN 92] Y. Tanaka, S. Yamada, M. Minamoto, Y. Fujita, T. Konishi, Japan Display, (1992), pp. 721.

[TAN 85] L. E. Tannas, Flat Panel Displays and CRT's (Von Nostrand Reinhold Company, New York, 1985).

[THO 65] D. G. Thomas, J. J. Hopfield, C. J. Frosch, Physical Review B 15, 857 (1965).

[TRO 95] U. Troppenz, T. K. Plant, B. Huettl, K. O. Velthaus, R. H. Mauch, Extended Abstracts of the First International Conference on the Science and Technology of Display Phosphors, (1995), pp. 65.

[TUE 91] R. T. Tuenge, J. Kane, SID Digest, (1991), pp. 279.

[VEC 68] A. Vecht, Journal of Applied Physics 1, 134 (1968).

[VER 93] R. Vercaumst, D. Poelman, R. L. V. Meirhaeghe, W. L. Flere, F. Cardon, International Display Research Conference, (1993), pp. 479.

[WAG 79] D. C. Wagner, W. M. Riggs, L. E. Davis, J. F. Moulder, Handbook of X-ray Photoelectron Spectroscopy (Perkin Elmer Company, Minnesota, 1979).

[WAR 96] W. L. Warren, K. Vanheusden, M. A. Rodriguez, C. H. Seager, D. R. Tallant, J. A. Tuchman, S. D. Silliman, D. T. Brower, P. D. Rack, P. H. Holloway, Second International Conference on the Science and Technology of Display Phosphors, (1996), pp. 127.

[WU 96] X. Wu, EL 96, (1996), pp. 285.

[YAM 87] N. Yamashita, Y. Michitsuji, S. Asano, Journal of the Electrochemical Society 134, 2932 (1987).

[YAM 95] N. Yamashita, O. Harada, K. Nakamura, Japanese Journal of Applied Physics 34, 5539 (1995).

[YAN 95] H. Yang, Y. K. Park, S. H. Ju, B. H. Chang, Applied Physics Letters 67, 70 (1995).

[YOS 89] T. Yoshioko, Y. Sano, K. Nakamura, C. Tani, SID Digest, (1989), pp. 313.

[ZUM 89] S. S. Zumdahl, Chemistry Second Edition (DC Heath and Company, Lexington, 1989).

BIOGRAPHICAL SKETCH

Philip Derek Rack was born on March 13, 1971, in Decatur Georgia. He was raised in Albuquerque, New Mexico, until 1982, when his family moved to Marietta, Georgia. In Marietta, he attended Sprayberry High School from 1985 to 1989 and after graduating he pursued a college education in the field of engineering. In the Fall of 1989, he began his studies at the Georgia Institute of Technology and in 1991 was admitted into the Materials Science and Engineering Department. During his undergraduate career, Philip worked in three different research groups as an undergraduate research assistant. In the summer of 1991, he worked for his father, Dr. Henry Rack, at Clemson University where he assisted on a project studying the high temperature properties of Ti-Al alloys. In 1992 he worked for Dr. Tom Starr at the Georgia Tech Research Institute where assisted on a computer simulation of a chemical vapor deposition process. Finally in 1993, he worked with Dr. Rosario Gerdhardt exploring impedance spectroscopy as a nondestructive test for dielectric composites. In June of 1993 Philip graduated magna cum laude from the Georgia Institute of Technology with his bachelor's degree in materials science and engineering. After graduating, he was married to Karen Lynn Fountain and in August of 1993 he enrolled as a doctoral student in the Materials Science and Engineering Department at the University of Florida. Under the supervision of Dr. Paul H. Holloway, he studied optical transitions of semiconducting materials for electroluminescent displays. As a result of his graduate studies, Philip received his doctoral degree in materials science and engineering in May 1997.

I certify that I have read this study and that in my opinion it conforms to acceptable standards of scholarly presentation and is fully adequate, in scope and quality, as a dissertation for the degree of Doctor of Philosophy.

Paul H Holloway

Paul H. Holloway, Chairman
Professor of Materials Science
and Engineering

I certify that I have read this study and that in my opinion it conforms to acceptable standards of scholarly presentation and is fully adequate, in scope and quality, as a dissertation for the degree of Doctor of Philosophy.

R. E. Hummel

Rolfe E. Hummel
Professor of Materials Science
and Engineering

I certify that I have read this study and that in my opinion it conforms to acceptable standards of scholarly presentation and is fully adequate, in scope and quality, as a dissertation for the degree of Doctor of Philosophy.

Kevin S. Jones
Associate Professor
of Materials Science
and Engineering

I certify that I have read this study and that in my opinion it conforms to acceptable standards of scholarly presentation and is fully adequate, in scope and quality, as a dissertation for the degree of Doctor of Philosophy.

Stephen J. Pearton
Professor of Materials Science
and Engineering

I certify that I have read this study and that in my opinion it conforms to acceptable standards of scholarly presentation and is fully adequate, in scope and quality, as a dissertation for the degree of Doctor of Philosophy.

David B. Tanner
Professor of Physics

This dissertation was submitted to the Graduate Faculty of the College of Engineering and to the Graduate School and was accepted as partial fulfillment of the requirements for the degree of Doctor of Philosophy.

May 1997

Winfred M. Phillips
Dean, College of Engineering

Karen A. Holbrook
Dean, Graduate School